

Trace Element Composition of Igneous and Hydrothermal Magnetite from Porphyry Deposits: Relationship to Deposit Subtypes and Magmatic Affinity*

Xiao-Wen Huang,^{1,2,3,1} Anne-Aurélié Sappin,^{2,3,4} Émilie Boutroy,^{2,5} Georges Beaudoin,^{2,3} and Sheida Makvandi^{2,3}

¹State Key Laboratory of Ore Deposit Geochemistry, Institute of Geochemistry, Chinese Academy of Sciences, Guiyang 550081, China

²Département de géologie et de génie géologique, Université Laval, Québec, Québec G1V 0A6, Canada

³Research Center on the Geology and Engineering of Mineral Resources (E4m), Université Laval, Québec, Québec G1V 0A6, Canada

⁴Geological Survey of Canada, Natural Resources Canada, 490 rue de la Couronne, Québec, Québec G1K 9A9, Canada

⁵Agnico Eagle Mines Limited, 1655 3e Av, Val d'Or, Québec J9P 1W1, Canada

Abstract

The trace element composition of igneous and hydrothermal magnetite from 19 well-studied porphyry Cu ± Au ± Mo, Mo, and W-Mo deposits was measured by laser ablation-inductively coupled plasma-mass spectrometry (LA-ICP-MS) and then classified by partial least squares-discriminant analysis (PLS-DA) to constrain the factors explaining the relationships between the chemical composition of magnetite and the magmatic affinity and porphyry deposit subtypes. Igneous magnetite can be discriminated by relatively high P, Ti, V, Mn, Zr, Nb, Hf, and Ta contents but low Mg, Si, Co, Ni, Ge, Sb, W, and Pb contents, in contrast to hydrothermal magnetite. Compositional differences between igneous and hydrothermal magnetite are mainly controlled by the temperature, oxygen fugacity, co-crystallized sulfides, and element solubility/mobility that significantly affect the partition coefficients between magnetite and melt/fluids. Binary diagrams based on Ti, V, and Cr contents are not enough to discriminate igneous and hydrothermal magnetite in porphyry deposits.

Relatively high Si and Al contents discriminate porphyry W-Mo hydrothermal magnetite, probably reflecting the control by high-Si, highly differentiated, granitic intrusions for this deposit type. Relatively high Mg, Mn, Zr, Nb, Sn, and Hf but low Ti and V contents discriminate porphyry Au-Cu hydrothermal magnetite, most likely resulting from a combination of mafic to intermediate intrusion composition, high chlorine in fluids, relatively high oxygen fugacity, and low-temperature conditions. Igneous or hydrothermal magnetite from Cu-Mo, Cu-Au, and Cu-Mo-Au deposits cannot be discriminated from each other, probably due to similar intermediate to felsic intrusion composition, melt/fluid composition, and conditions such as temperature and oxygen fugacity for the formation of these deposits.

The magmatic affinity of porphyritic intrusions exerts some control on the chemical composition of igneous and hydrothermal magnetite in porphyry systems. Igneous and hydrothermal magnetite related to alkaline magma is relatively rich in Mg, Mn, Co, Mo, Sn, and high field strength elements (HFSEs), perhaps due to high concentrations of chlorine and fluorine in magma and exsolved fluids, whereas those related to calc-alkaline magma are relatively rich in Ca but depleted in HFSEs, consistent with the high Ca but low HFSE magma composition. Igneous and hydrothermal magnetite related to high-K calc-alkaline magma is relatively rich in Al, Ti, Sc, and Ta, due to a higher temperature of formation or enrichment of these elements in melt/fluids.

Partial least squares-discriminant analysis on hydrothermal magnetite compositions from porphyry Cu, iron oxide copper-gold (IOCG), Kiruna-type iron oxide-apatite (IOA), and skarn deposits around the world identify important discriminant elements for these deposit types. Magnetite from porphyry Cu deposits is characterized by relatively high Ti, V, Zn, and Al contents, whereas that from IOCG deposits can be discriminated from other types of magnetite by its relatively high V, Ni, Ti, and Al contents. IOA magnetite is discriminated by higher V, Ti, and Mg but lower Al contents, whereas skarn magnetite can be separated from magnetite from other deposit types by higher Mn, Mg, Ca, and Zn contents. Decreased Ti and V contents in hydrothermal magnetite from porphyry Cu and IOA, to IOCG, and to skarn deposits may be related to decreasing temperature and increasing oxygen fugacity. The relative depletion of Al in IOA magnetite is due to its low magnetite-silicate melt partition coefficient, immobility of Al in fluids, and earlier, higher-temperature magmatic or magmatic-hydrothermal formation of IOA deposits. The relative enrichment of Ni in IOCG magnetite reflects more mafic magmatic composition and less competition with sulfide, whereas elevated Mn, Mg, Ca, and Zn in skarn magnetite results from enrichment of these elements in fluids via more intensive fluid-carbonate rock interaction.

Introduction

Magnetite is ubiquitous in various types of rocks and mineral deposits. Hydrothermal magnetite in porphyry Cu ± Au ± Mo deposits can be disseminated in early, high-temperature, K-Fe (potassic feldspar + magnetite) alteration and occurs as veins in different stages of sulfide mineralization (Nadoll et

al., 2014, 2015; Canil et al., 2016). In propylitic and supergene alteration stages, magnetite can be partly or completely transformed to hematite. Although magnetite is an accessory mineral in economic copper ores, abundant hydrothermal magnetite is found in gold-rich porphyry deposits, which may be related to more oxidized magma (Sillitoe, 1997; Sinclair, 2007). Formation of hydrothermal magnetite in porphyry deposits involves the reaction between ferrous iron and water or sulfate, resulting in decreased pH and oxygen fugacity

*Corresponding author: e-mail, huangxiaowen2008@live.cn

*This paper is the version of record, replacing any pre-publication versions.

in fluids that cause sulfide precipitation (Sun et al., 2013). Experimental studies also demonstrate that iron in magmatic-hydrothermal systems (e.g., porphyry systems) can be transported as FeCl_2 by magmatic vapor, and magnetite is expected to deposit during volatile exsolution at high temperature and pressure (Simon et al., 2004). In addition to hydrothermal magnetite, igneous magnetite is also common in the host or country rocks of porphyry deposits (Ishihara, 1977; Nadoll et al., 2015; Pisiak et al., 2017).

Chemical composition of igneous and hydrothermal magnetite, in combination with petrographic description and statistical analysis, can be used to discriminate magnetite from various geologic environments (Carew, 2004; Singoyi et al., 2006; Rusk et al., 2009; Dupuis and Beaudoin, 2011; Dare et al., 2012, 2014; Nadoll et al., 2012, 2014; Huang et al., 2013, 2014, 2015a, b, 2016, 2018; Boutroy et al., 2014) and can be employed to fingerprint different types of ore deposits (Dupuis and Beaudoin, 2011; Boutroy et al., 2014; Makvandi et al., 2016a, b, 2017; Pisiak et al., 2017; Huang et al., 2019). A number of in situ iron oxide trace element studies of porphyry deposits (Dupuis and Beaudoin, 2011; Mountjoy, 2011; Nadoll et al., 2014, 2015; Canil et al., 2016; Pisiak et al., 2017) discussed the factors controlling compositional variations in iron oxides and the formation of mineralization. For example, Canil et al. (2016) applied principal component analysis (PCA) to identify correlations among elements and proposed that the compositional differences between hydrothermal magnetite from porphyry $\text{Cu} \pm \text{Au} \pm \text{Mo}$ and skarn deposits in British Columbia (Canada) were caused by variations in temperature, oxygen fugacity, and nature and composition of hydrothermal fluids. Dupuis and Beaudoin (2011) proposed the $\text{Ca} + \text{Al} + \text{Mn}$ versus $\text{Ti} + \text{V}$ and $\text{Ni}/(\text{Cr} + \text{Mn})$ versus $\text{Ti} + \text{V}$ diagrams to discriminate iron oxide copper-gold (IOCG), Kiruna-type iron oxide-apatite (IOA), banded iron formation, porphyry Cu , skarn, Fe-Ti-V , Ni-Cu-platinum group element (PGE), and volcanogenic massive sulfide deposits. These discrimination diagrams are useful in identifying the iron oxides with unknown origin. However, individual analyses of samples from a specific deposit type (e.g., porphyry Cu , skarn, IOA) can show a large compositional variability. Nadoll et al. (2014, 2015) investigated the trace element composition of magnetite from porphyry Cu and skarn deposits from the southwestern United States and argued that the boundary in the $\text{Al} + \text{Mn}$ versus $\text{Ti} + \text{V}$ diagram to separate these two deposit types is transitional. Pisiak et al. (2017) calculated discriminant functions using linear discriminant analysis (LDA) of trace element data of barren igneous, ore-related igneous, and porphyry hydrothermal magnetite and applied the results to exploration for porphyry deposits near the Mount Polley Cu-Au deposit (Canada). Their study demonstrated that LDA of magnetite composition is useful for exploration of porphyry deposits covered by glacial sediments (Pisiak et al., 2017).

Porphyry deposits can be classified into subtypes—such as porphyry Cu , Cu-Mo , Cu-Au , Cu-Mo-Au , Au , Mo , W-Mo , Sn , Sn-Ag , and Ag deposits—according to their metal endowment (Kirkham and Sinclair, 1995; Singer, 1995; Cooke et al., 2005; Sinclair, 2007; Sillitoe, 2010). Different types of porphyry deposits reflect various magma and fluid compositions and physical conditions such as temperature, pressure, and oxygen fugacity. For example, high-sulfidation Au -rich

deposits commonly occur at shallower levels above porphyry Cu systems (Sillitoe, 2010). Sillitoe (2010) showed that the host rock composition may play an important role in the size of a deposit, ore grade, and mineralization styles in porphyry deposits. Granitic rocks related to porphyry Cu and Mo deposits commonly belong to the magnetite series, whereas those related to porphyry W and Sn deposits mainly belong to ilmenite series granitoids (Ishihara, 1981; Sinclair, 2007). The porphyritic intrusions in porphyry Cu systems show an affinity with metaluminous and medium-K calc-alkaline or alkaline magmas (Seedorff et al., 2005; Sillitoe, 2010). There is an affinity between high-K calc-alkaline rocks and gold-rich porphyry systems (Müller and Groves, 1993; Sillitoe, 1997, 2000). Felsic intrusive rocks genetically related to porphyry W deposits are commonly characterized by F-rich fluorite and/or topaz (Sinclair, 1995). However, the relationship between the chemical composition of igneous and hydrothermal magnetite with the porphyry deposit subtypes and the magmatic affinity of the porphyritic intrusions remains poorly studied.

In this study, we investigate the chemical composition of igneous and hydrothermal magnetite from a wide range of porphyry deposit subtypes (Table 1). These deposits formed in a range of geologic environments, with different ages and country rock types, and are related to porphyry intrusions with various compositions and magmatic affinities (Table 1). Trace element compositions of magnetite were determined using electron probe microanalysis (EPMA) and laser ablation-inductively coupled plasma-mass spectrometry (LA-ICP-MS). The geochemical data were investigated by partial least squares-discriminant analysis (PLS-DA) to identify factors controlling the formation of igneous and hydrothermal magnetite in porphyry systems and to establish the link of igneous and hydrothermal magnetite chemistry with porphyry deposit subtypes and the magmatic affinity of porphyry intrusions. The trace element composition of hydrothermal magnetite from porphyry Cu deposits is also compared with that of IOCG, IOA, and skarn magnetite to identify possible relationships between them and to provide a better understanding of trace element fingerprints in magnetite from porphyry deposits.

Sampling and Analytical Methods

Sampling

Seventy-nine samples representing different types of host rocks, veins, and hydrothermal alteration were collected from porphyry $\text{Cu} \pm \text{Au} \pm \text{Mo}$ (17), porphyry Mo (1), and porphyry W-Mo (1) deposits (Table 1). These deposits are distributed in western and eastern North America, western South America, Eastern Europe, Central Asia, and the southwestern Pacific regions (Table 1). According to the main metals, these deposits can be divided into porphyry Au-Cu , Cu-Au , Cu-Mo , Cu-Mo-Au , Mo , and W-Mo deposits of Late Ordovician to Miocene age (Table 1). They are mainly hosted by intrusions, dikes, and stocks of intermediate to felsic composition, e.g., diorite, monzonite, monzodiorite, syenite, granite, and granodiorite. Some deposits are also hosted by subvolcanic porphyries such as andesite to rhyolite, trachyandesite, trachyte, and alkaline basalt (Table 1). The porphyry intrusions were emplaced into a range of country rocks, including andesitic to basaltic volcanic rocks, volcanoclastic rocks, clastic sedimentary rocks,

Table 1. Main Characteristics of Studied Porphyry Deposits

Deposit	Location	Mineralization	Production, resource, or reserve	Age	Magmatic affinity	Host porphyry composition	Host porphyry classification	Country rock	Reference
<u>Western North America</u>									
Bingham Canyon	United States	Cu-Mo-Au	Production: 2,666 Mt at 0.74% Cu, 0.04% Mo, 0.49 g/t Au, and 3.29 g/t Ag	Eocene (~39–37 Ma)	High-K calc-alkaline	Quartz monzonite	Intermediate	Siliciclastic and carbonate rocks of the Oquirrh Group	Cooke et al. (2005), Redmond and Einandi (2010)
Granisle	Canada	Cu-Au	Production: 53 Mt at 0.47% Cu	Eocene (~51 Ma)	Calc-alkaline	Quartz diorite porphyry and biotite feldspar porphyry	Intermediate	Andesite and sedimentary rocks (shale, siltstone, conglomerate) of the Hazelton Group	Wilson et al. (1980), Dirom et al. (1995)
Butte	United States	Cu-Mo	Production and reserves: 2,083 Mt at 0.85% Cu	Paleocene (~66–64 Ma)	Calc-alkaline	Quartz porphyry and granite porphyry	Felsic	Butte granite and co-genetic aplites and pegmatites	Lund et al. (2002), Dilles et al. (2003), Cooke et al. (2005), Rusk et al. (2008), Reed et al. (2013)
Mount Milligan	Canada	Cu-Au	Total proven and probable reserves: 542 Mt at 0.20% Cu and 0.36 g/t Au	Early Jurassic (~183 Ma)	Alkaline	Quartz monzonite to monzodiorite	Intermediate	Trachyandesites and volcaniclastic rocks of the Witch Lake Group	LeFort et al. (2011), Jago et al. (2014), Logan and Mihalyuk (2014), Thompson Creek Metals Company (internal report, 2016)
Copper Mountain	Canada	Cu-Au	Total proven and probable reserves: 205 Mt at 0.29% Cu, 0.10 g/t Au, and 1.21 g/t Ag	Late Triassic–Early Jurassic (~204–200 Ma)	Alkaline	Diorite, monzonite, and syenite	Intermediate	Andesite to basalt of the Nicola Group	Holbek and Noyes (2013), Logan and Mihalyuk (2014)
Mount Polley	Canada	Cu-Au	Total measured and indicated resources: 411 Mt at 0.28% Cu, 0.29 g/t Au, and 0.81 g/t Ag (cutoff grade of 0.25% Cu equiv)	Late Triassic (~205–202 Ma)	Alkaline	Diorite, monzonite, plagioclase porphyry, and syenite	Intermediate	Basalt and carbonaceous sedimentary rocks of the Nicola Group	Fraser (1994), Logan and Mihalyuk (2014), Pass et al. (2014), Imperial Metals Corporation (internal report, 2016)
Endako	Canada	Mo	Production and reserves: 341 Mt at 0.07% Mo	Late Jurassic (~148–145 Ma)	Calc-alkaline	Granitic rocks	Felsic	Granite to granodiorite of the François Lake plutonic suite	Selby et al. (2000), Selby and Creaser (2001), Sinclair (2007)
<u>Western South America</u>									
Bajo de la Alumbrera	Argentina	Cu-Au	Production and remaining resources: 605 Mt at 0.54% Cu and 0.64 g/t Au	Miocene (~7 Ma)	High-K calc-alkaline	Dacite porphyry	Intermediate	Andesite of the Farallón Negro Volcanic Complex	Ulrich and Heinrich (2001), Proffett (2003), Harris et al. (2008)

Table 1. (Cont.)

Deposit	Location	Mineralization	Production, resource, or reserve	Age	Magmatic affinity	Host porphyry composition	Host porphyry classification	Country rock	Reference
Morococha (district)	Peru	Cu-Mo-Au	Total measured and indicated resources of the Toromochu porphyry Cu-Mo deposit: 520 Mt at 0.37% Cu, 0.01% Mo, and 6.10 g/t Ag	Miocene (~9–7 Ma)	Calc-alkaline	Dioritic, granodioritic, and quartz monzonitic porphyry	Intermediate	Carbonate rocks of the Pucará Group and Anticona diorite	Catchpole et al. (2015), Chinalco Mining Corporation (internal report, 2016)
Escondida Norte	Chile	Cu-Mo	Production and reserves: sulfide (supergene): 1,280 Mt at 1.24% Cu; oxide: 330 Mt at 0.77% Cu	Eocene (~38–36 Ma)	Calc-alkaline	Granodiorite to tonalite	Felsic	Andesite to rhyolite of La Tabla Formation and coeval intrusive phase	Cooke et al. (2005), Romero et al. (2011)
<u>Eastern North America</u>									
Mount Pleasant	Canada	W-Mo	Production and reserves: 22.5 Mt at 0.21% W, 0.10% Mo, and 0.08% Bi	Carboniferous (~340–330 Ma)	Calc-alkaline	Granitic rocks	Felsic	Rhyolite to dacite, minor andesite, trachyandesite and basalt, and argillite breccia of the Piskahegan Group	Kooiman et al. (1986), Samson (1990), Yang et al. (2003)
<u>Eastern Europe</u>									
Rosia Poteni	Romania	Cu-Au	Total measured, indicated, and inferred resources: 350 Mt at 0.36% Cu and 0.29 g/t Au	Miocene (~9 Ma)	Calc-alkaline	Diorite porphyry	Intermediate	Rotunda andesite, volcaniclastic rocks, and sedimentary rocks	Borcos et al. (1998), Mihu et al. (2004), Kouzmanov et al. (2005)
Skouries	Greece	Cu-Au	Total proven and probable reserves: 138 Mt at 0.53% Cu and 0.81 g/t Au	Miocene (~19 Ma)	Alkaline	Monzonite porphyry	Intermediate	Biotite gneiss and schist of the Vertiskos Formation	Frei (1995), Kroll et al. (2002), Eliopoulos et al. (2014)
<u>Central Asia</u>									
Sari Gunay	Iran	Au-Cu	Resources: 52 Mt at 1.77 g/t Au (cutoff grade of 1.00 g/t Au)	Miocene (~12–10 Ma)	Alkaline	Latitic to trachytic volcanic complex	Intermediate	Schist, limestone, and intermediate to felsic volcanic rocks	Richards et al. (2006)
Reko Diq (H9, H13, H14-H15, H79, Spegar centers)	Pakistan	Cu-Au	Total measured, indicated, and inferred resources: 5,900 Mt at 0.41% Cu and 0.22 g/t Au	Miocene (~14–10 Ma)	Calc-alkaline	Quartz diorite to granodiorite	Intermediate	Andesite of the Reko Diq Formation and clastic sedimentary rocks of the Dalbandin Formation	Perelló et al. (2008), Raziq et al. (2014), Tethyan Copper Company (internal report, 2016)
Kharmagtai (district)	Mongolia	Cu-Au	Total measured, indicated, and inferred resources: 133 Mt at 0.36% Cu and 0.37 g/t Au (cut-off grade of 0.30% Cu equivalent)	Late Carboniferous (~297 Ma)	Calc-alkaline	Monzodiorite and diorite porphyry	Intermediate	Volcano-sedimentary sequence	Kirvin et al. (2005), Müller et al. (2010), A. Víggar (unpub. report, 2014)

Table 1. (Cont.)

Deposit	Location	Mineralization	Production, resource, or reserve	Age	Magmatic affinity	Host porphyry composition	Host porphyry classification	Country rock	Reference
Oyu Tolgoi (district)	Mongolia	Cu-Mo-Au	Total proven and probable reserves: 1,494 Mt at 0.85% Cu, 0.31 g/t Au, and 1.23 g/t Ag	Late Devonian (~372–370 Ma)	High-K calc-alkaline	Quartz monzodiorite	Intermediate	Basalt and minor volcanoclastic and sedimentary rocks of the Oyu Tolgoi and Herga sequences	Perelló et al. (2001), Crane et al. (2012), Porter (2016)
Southwestern Pacific									
Poregera (deep veins)	Papua New Guinea	Au-Cu	Total proven and probable reserves: 14 Mt at 4.24 g/t Au	Miocene (~6 Ma)	Alkaline	Hypabyssal intrusions of alkali basaltic, hawaiitic, and mugearitic compositions	Mafic	Carbonaceous mudstones and calcareous siltstones of the Chlm Formation	Richards et al. (1997), Romacher et al. (2004), Barrick Gold Corporation (internal report, 2015)
Ridgeway	Australia	Au-Cu	Total measured, indicated, and inferred resources: 150 Mt at 0.51 g/t Au, 0.33% Cu, and 0.65 g/t Ag	Late Ordovician (~457–456 Ma)	Alkaline	Monzodiorite to quartz monzonite	Intermediate	Andesitic- and basaltic-clast volcanic conglomerate and siltstone of the Weemalla Formation	Wilson et al. (2007), Newcrest Mining (internal report, 2016)

carbonate rocks, granite to diorite, schist, and gneiss (Table 1). The volcanic and intrusive rocks have alkaline, calc-alkaline, and high-K calc-alkaline affinities (Table 1). A total of 630 magnetite grains from the 79 samples were analyzed by EPMA, and 68 magnetite grains from 19 samples were analyzed by LA-ICP-MS (Table 2). The EPMA data set includes 242 analyses from Dupuis and Beaudoin (2011) (Table 2).

Petrography

Optical petrography was used to characterize the mineral assemblage and magnetite texture and to assist in discrimination of hydrothermal from igneous magnetite. Magnetite textures were examined using a JEOL JSM-840A scanning electron microscope at Université Laval (Québec, Canada) under backscattered electron (BSE) and secondary electron modes. Semiquantitative energy dispersive X-ray spectrometry (EDS) was used to identify exsolution products, mineral inclusions, and associated minerals. Operating conditions used an accelerating voltage of 15 kV and a beam current of 60 μA at a working distance of 20 mm.

EPMA analyses

Magnetite was analyzed by a CAMECA SX-100 EPMA at Université Laval using conditions similar to those described in Boutroy et al. (2014) and Huang et al. (2019). The analyses here were performed using 10-μm diameter beam, 15-kV voltage, and 100-nA current. Analyzed crystals are lithium fluoride (LIF) for V and Cr; large lithium fluoride (LLIF) for Zn, Cu, Ni, and Mn; large pentaerythritol (LPET) for K, Sn, Ca, and Ti; and thallium acid phthalate (TAP) for Al, Si, and Mg. Kα signal was acquired for all elements. Standards such as simple oxides (GEO standard block of P and H Developments) and natural minerals (mineral standard mount MINM 25–53, Astimex Scientific) were used to calibrate the analyses (Jurek and Hulínský, 1980). The background was measured for 15 to 20 s, and the concentration was counted over the peak for 20 to 40 s, depending on the element. The average detection limits are 17 ppm for K, 23 ppm for Ca, 29 ppm for Sn, 34 ppm for Cr, 67 ppm for Ni, 83 ppm for Mg, 93 ppm for Cu, 105 ppm for Mn, 110 ppm for V, 149 ppm for Zn, 151 ppm for Si, 154 ppm for Ti, and 301 ppm for Al.

LA-ICP-MS analyses

Trace elements in magnetite were analyzed by an LA-ICP-MS at Université du Québec à Chicoutimi (UQAC), using a RESOLUTION M-50 193-nm Excimer laser ablation system and an Agilent 7700x ICP-MS. The detailed analytical conditions and data reduction procedures are similar to those described in Boutroy et al. (2014) and Huang et al. (2019) and are only summarized here. The ablation was carried out across the surface of magnetite grains to obtain relatively homogeneous composition and avoid visible mineral inclusions. Each analysis includes 20- to 30-s gas blank and 20- to 60-s ablation under the conditions of 25- to 80-μm beam, 3- to 15-μm/s stage speed, 10-Hz frequency, and 5-mJ/pulse power for the laser system. The synthetic basalt glass (U.S. Geological Survey), GSD-1G, and natural magmatic magnetite (Bushveld in South Africa; Dare et al., 2012), BC-28, are used to monitor the analyses. Intensity data are transformed to concentration data by Iolite software, using Fe (72.36 wt %, stoichiometric

value) as internal standard and synthetic Fe-rich basalt glass (U.S. Geological Survey), GSE-1G, as external calibration standard (Dare et al., 2012; Savard et al., 2012).

Statistical Methods

Estimation of average composition

Some elements measured by EPMA and LA-ICP-MS have concentrations below the detection limit. These censored data (Helsel, 2005) are commonly deleted from the data sets. Use of simple arithmetic mean will result in higher average values. Instead, we calculate the average composition of magnetite using NADA package in R, which was based on the nonparametric Kaplan-Meier method (Lee and Helsel, 2007).

Data preprocessing and PLS-DA

Following Makvandi et al. (2016b), censored concentration data were imputed using robCompositions package in R, which involves k-nearest neighbors' function with the Aitchison distance (Hron et al., 2010). In order to overcome the closure problem resulting from concentration data based on a total of 100% (Aitchison, 1986; Whitten, 1995), data was transformed to centered-log ratio prior to PLS-DA (Aitchison, 1986; Egozcue et al., 2003; Makvandi et al., 2016b).

Multivariate statistical analysis of EPMA and LA-ICP-MS data was performed in order to (1) recognize factors responsible for compositional variations of magnetite, (2) identify the relationship between igneous and hydrothermal magnetite, and (3) unravel the relationships between magnetite chemistry and deposit subtype, magmatic affinity, and host porphyry composition. The PLS-DA method has been described in Makvandi et al. (2016b) and Huang et al. (2019). PLS-DA is a supervised classification in which predefined groups of observations (samples) are labeled, in contrast to an unsupervised statistical analysis technique such as PCA. This method maximizes differences among the labeled groups by rotating principal components and identifying the most important variables (elements) in the classification (De Iorio et al., 2007; Wold et al., 2001; Eriksson et al., 2013; Brereton and Lloyd, 2014).

A number of PLS-DA components can be extracted with decreasing importance in explaining the data set variance. Usually, the first two or three components account for most of the variance in the data set (Makvandi et al., 2016b). Four types of plots generated by PLS-DA are used here for interpreting the results. The first and second loading plots (q_w^*1 - q_w^*2) show the element correlations and the relationship between elements and labeled groups, such as magnetite types, deposit subtypes, magmatic affinity, and porphyry composition. Elements plotting in the same quadrant are positively correlated and are inversely correlated to elements in the opposing quadrant. Elements with larger absolute loading values are more important in the regression. First and second score scatter plots (t_1 - t_2) show the distribution of individual analyses (samples) and the relationship among labeled groups. The score contribution plot is used to highlight the compositional differences between a sample group and the average of the data set. One element in a sample group with a positive or negative score contribution value can be interpreted as higher or lower concentration of this element in the sample

group compared to the average composition of the data set (Makvandi et al., 2016b). Variable importance on projection (VIP) plots emphasize the importance of each element for discriminating each labeled sample group. The elements with VIP values ≥ 1 have major controls in the discriminant analysis (Eriksson et al., 2013).

Petrography

One important aspect of petrographic observations is to discriminate igneous magnetite from hydrothermal magnetite. McQueen and Cross (1998) showed that textural features such as crystal morphology and mineral association can be used to distinguish the origin of magnetite. Nadoll et al. (2015) suggested that magnetite of igneous and hydrothermal origin can be determined based on occurrence (vein vs. disseminated in host rock), crystal habit (euhedral vs. massive), associated minerals (mafic vs. hydrothermal minerals), and the occurrence and type of exsolution and mineral inclusions.

Igneous magnetite in porphyry systems

In the studied porphyry deposits, igneous magnetite is disseminated in barren to slightly mineralized, weakly altered, volcanic and intrusive host rocks, such as andesite (Fig. 1A), dacite (Fig. 1B), diorite, and monzonite porphyries. Igneous magnetite is an accessory phase (<10 modal %) associated with felsic and mafic magmatic minerals including plagioclase, K-feldspar, hornblende, and biotite (Fig. 1A, B). Igneous magnetite occurs as subhedral to anhedral grains (Fig. 1A, B) and rarely as bands in ilmenite grains in the Rosia Poeni porphyry Cu-Au deposit (Fig. 1C). It commonly contains ilmenite and spinel exsolution lamellae (Fig. 1D). Titanite may occur as inclusions in magnetite (Fig. 1E) or as replacement of ilmenite lamellae in magnetite (Fig. 1F). Locally, hematite partially replaced magnetite (martitization) along spinel planes, rims, and fissures (Fig. 1D). In the Mount Milligan deposit, igneous magnetite is also replaced by chalcopyrite along fractures (Fig. 1F).

Hydrothermal magnetite in porphyry systems

Nadoll et al. (2014) commented on the difficulty of recognizing hydrothermal and magmatic magnetite. In a porphyry system, assigning a hydrothermal origin to magnetite can be complicated by multiple vein generations, overprints of multiple alteration stages, fluid-rock interaction, and secondary weathering processes (Nadoll et al., 2014). For example, early magnetite veins can be crosscut by K-feldspar + quartz + magnetite + pyrite veins, and both veins can be cut by late quartz + sericite + pyrite \pm magnetite veins (Einaudi, 1982; Titley, 1990; Nadoll et al., 2014). Here, vein crosscutting relationships and magnetite generations are not emphasized, because the compositional variations of hydrothermal magnetite are discussed at deposit or deposit-type scale rather than at the vein scale. All generations of magnetite with possible hydrothermal origin are grouped together. Hydrothermal magnetite is abundant (~ 15 - 30 modal %) within weakly to strongly altered host rocks and within fissures, associated with sericite, chlorite, and epidote (Fig. 2A). Anhedral to subhedral hydrothermal magnetite is disseminated in sericitized, feldspath-rich rock and was crosscut by chlorite + magnetite + chalcopyrite veins (Fig. 2A). In addition, hydrothermal magnetite mainly occurs within and along quartz-dominated (Fig. 2B, C) and

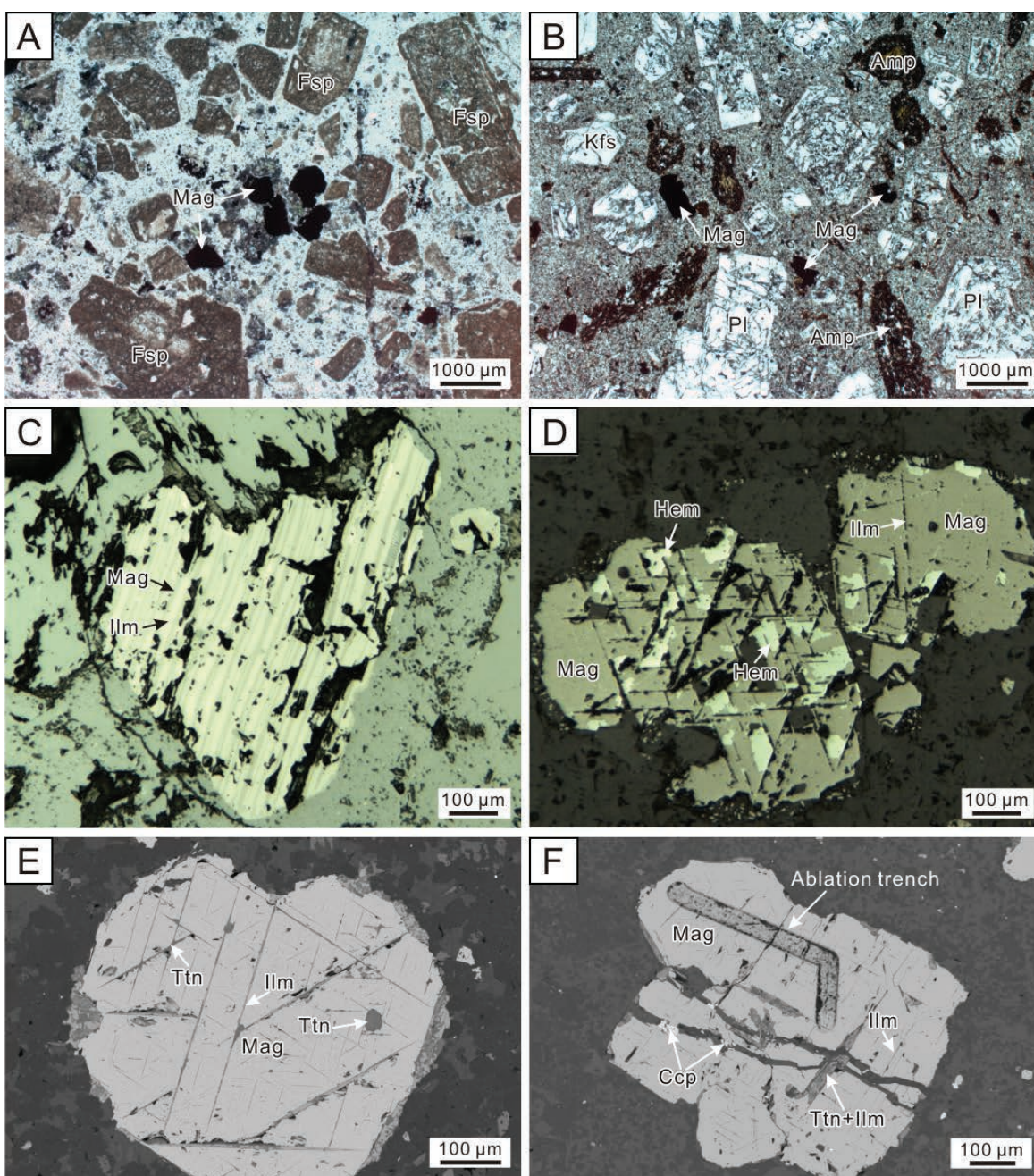


Fig. 1. Photomicrographs showing the occurrences of igneous magnetite from the porphyry deposits. A and B are images under transmitted light, whereas C and D are images under reflected light. E and F are BSE images. A. Subhedral to anhedral igneous magnetite disseminated in andesite porphyry from the Mount Milligan Cu-Au deposit (sample 90-616-191). The andesite is composed of phenocrysts of sericitized feldspar in a quartzo-feldspathic matrix. B. Anhedral igneous magnetite disseminated in dacite porphyry from the Reko Diq Cu-Au deposit (sample Spegar1). The dacite is composed of phenocrysts of plagioclase, K-feldspar, and amphibole in a quartzo-feldspathic matrix. C. Magnetite occurring as exsolution bands in ilmenite in andesite porphyry from the Rosia Poieni Cu-Au deposit (sample RP-4-CH-34). D. Magnetite with ilmenite exsolution lamellae replaced by hematite from the Reko Diq Cu-Au deposit (sample RK 8). E. Igneous magnetite from the Reko Diq Cu-Au deposit showing exsolution lamellae of ilmenite (sample RK 22). Some lamellae have transformed to titanite. F. Magnetite from the Mount Milligan Cu-Au deposit replaced by chalcopyrite and titanite (sample 90-616-191). Abbreviations: Amp = amphibole, Ccp = chalcopyrite, Fsp = feldspar, Hem = hematite, Ilm = ilmenite, Kfs = K-feldspar, Mag = magnetite, Pl = plagioclase, Ttn = titanite.

magnetite-dominated (Fig. 2D-F) veins. It forms disseminated grains (Fig. 2B) or massive aggregates (Fig. 2C, D) and is locally surrounded by chalcopyrite (Fig. 2C) and pyrite (Fig. 2E). Hydrothermal magnetite is partially or totally martitized

(Fig. 2F). In the Kharmagtai and Skouries deposits, replacement of magnetite by chalcopyrite is common (Fig. 2G, H).

Weak oscillatory zoning is locally found in hydrothermal magnetite using BSE imaging. Zonation is characterized by

light-gray zones, which alternate with fine dark-gray zones rich in small inclusions (<1–10 μm ; Fig. 3A–E). Quartz is the main inclusion in magnetite. Some magnetite grains from the Mount Pleasant W-Mo deposit show dissolution-reprecipitation texture composed of Si-rich, dark-gray and Si-poor, light-gray domains (Fig. 3F). This texture in porphyry deposits is not as common as in IOCG, IOA, and skarn deposits (Hu et al., 2015; Heidarian et al., 2016; Huang et al., 2018; Huang and Beaudoin, 2019). Because of elemental heterogeneity in magnetite with oscillatory zoning and compositional modification during dissolution-reprecipitation processes (Hu et al., 2015; Huang et al., 2018), magnetite grains with oscillatory zoning and dissolution-precipitation textures were not analyzed by EPMA and LA-ICP-MS.

Chemical Composition of Magnetite

Igneous and hydrothermal magnetite from the porphyry deposits contains variable trace element contents. Titanium, Si, Al, Mn, Cu, Mg, V, Zn, Ca, K, Cr, Sn, P, Ni, Pb, W, Zr, Co, and Ga (in decreasing order of maximum abundance) are in concentrations higher than 100 ppm. Magnetite also contains low concentrations (<100 ppm) of Nb, As, Sc, Y, Mo, La, Bi, Sm, Sb, Hf, Ta, Ge, Yb, In, and Ag. Cadmium, PGEs (Ir, Pt, and Os), and Au are typically below or close to the lower detection limit of LA-ICP-MS. The full EPMA and LA-ICP-MS data set for all magnetite grains is given in Appendix Table A1. Elements such as Mg, Al, Ti, V, and Mn occur in significant concentrations in magnetite and are often detectable by both EPMA and LA-ICP-MS. Other elements such as K, Sn, Cu, Zn, Si, Ca, Cr, and Ni often have lower concentration near or below detection for the EPMA. There is a good correlation between EPMA and LA-ICP-MS analyses for elements V, Al, and Mn ($R^2 = 0.98, 0.83, 0.75$; App. Fig. A1). However, significant differences are observed between EPMA and LA-ICP-MS analyses for elements Ti, Mg, Cr, Ca, and Si ($R^2 = 0.36, 0.32, 0.28, 0.04, 0.006$; App. Fig. A1). Significant scatter observed for certain elements may be due to the difference in beam size between the EPMA and LA-ICP-MS. For example, extensive exsolution is observed in the igneous magnetite grains (Fig. 1D–F). The smaller beam size of EPMA (10 μm) is less able to homogenize entire bulk composition of magnetite with significant exsolution lamellae, whereas the area rasterized by the larger laser spot size (80 μm) is more efficient for homogenizing material during analysis (Dare et al., 2012). Therefore, this difference in sampling would contribute significantly to differences in concentrations for any element that is heterogeneously distributed in magnetite, such as Ti, which occurs as ilmenite exsolution lamellae (Fig. 1D–F). The significant differences in Si, Ca, Mg, and Cr concentrations between EPMA and LA-ICP-MS analyses may be due to different detection limits of these elements for two different analytical techniques and unresolved mineral inclusions during LA-ICP-MS analyses. For example, the higher Si and Ca contents analyzed by LA-ICP-MS than by EPMA (App. Fig. A1) are partly due to unavoidable mineral inclusions that occur in submicron or nanometer scale.

Average trace element composition of magnetite

The chemical composition of individual analyses and the average composition of each sample, normalized to bulk

continental crust (Rudnick and Gao, 2003), are shown in Appendix Figures A2 to A5. EPMA data show that igneous and hydrothermal magnetite from the same deposit have similar normalized trace element patterns, respectively, and that normalized ratios of a specific element vary within one order of magnitude (App. Figs. A2–A4). Igneous and hydrothermal magnetite from the same deposit have different trace element patterns. For example, igneous magnetite (sample 3133) from the Bajo de la Alumbrera Cu-Au deposit has higher Al, Mn, Mg, Ti, and Zn contents than hydrothermal magnetite (App. Fig. A2). Similarly, igneous magnetite from the Reko Diq Cu-Au deposit (sample Spegar1) and from the Butte Cu-Mo deposit (sample 10880-B) have higher Al, Mn, Mg, and Ti contents than hydrothermal magnetite in the same deposit (App. Figs. A3, A4). However, some igneous magnetite grains (e.g., Loc18b in Reko Diq or Bur-98-5 and Bur-98-8 in Butte) also show trace element patterns similar to hydrothermal magnetite in the same deposit (App. Figs. A3, A4). LA-ICP-MS data show igneous magnetite from the same deposit has more variable trace element compositions with normalized Zr, Ta, Nb, W, and Cu content variation exceeding one order of magnitude (App. Fig. A5). This is the same for hydrothermal magnetite (App. Fig. A5).

Figure 4 provides the average composition of individual deposits, normalized to bulk continental crust (Rudnick and Gao, 2003). EPMA data show that most igneous magnetite from different porphyry deposits has similar normalized trace element patterns (Fig. 4A), with the exception of the Mount Milligan deposit, which has Mn contents one order of magnitude lower than other samples. Hydrothermal magnetite from most porphyry deposits shows similar normalized EPMA trace element patterns (Fig. 4B). However, hydrothermal magnetite from the Mount Pleasant W-Mo deposit has higher Si, Al, and Sn but lower Mg, Ti, and V contents than that from other deposits (Fig. 4B). LA-ICP-MS data show that igneous magnetite from the Bajo de la Alumbrera and Butte deposits has slightly different trace element patterns with normalized ratios of P, Pb, Ta, and Nb varying by close to one order of magnitude (Fig. 4C). In addition, hydrothermal magnetite from the Reko Diq Cu-Au deposit has the highest Y, P, Pb, Ge, W, and Mo contents, whereas that from the Porgera Au-Cu deposit has the lowest W, Cu, Ga, Ti, and V contents (Fig. 4D).

Box and whisker plots of trace element contents in igneous and hydrothermal magnetite show that EPMA mean values for hydrothermal magnetite are higher for Si, K, Sn, Cu, and Ni but lower for Ca, Al, Mn, Mg, Ti, Zn, and V contents (Fig. 5A). LA-ICP-MS analyses show that hydrothermal magnetite has higher Pb, Ge, W, Sc, Cu, Mo, Ga, Co, and Ni but lower Ca, Y, P, Zr, Hf, Al, Ta, Nb, Sn, Mn, Mg, Ti, Zn, V, and Cr contents compared to igneous magnetite (Fig. 5B).

Compositional comparison for magnetite from different deposit subtypes

There is some overlapping of igneous/hydrothermal magnetite composition between different deposit subtypes in terms of the large compositional variations. However, significant differences can be identified in terms of the average composition for different deposit subtypes. EPMA analyses show that igneous magnetite from porphyry Cu-Au deposits has higher

Mn, Mg, Ti, and Zn average contents than that from porphyry Cu-Mo and Cu-Mo-Au deposits (Fig. 6A). Igneous magnetite from porphyry Cu-Mo deposits shows higher V and Cr average contents than that from the other two deposit types, whereas that from porphyry Cu-Mo-Au deposits is characterized by relatively high K contents (Fig. 6A). Limited LA-ICP-MS data (four and seven analyses for porphyry Cu-Au and Cu-Mo, respectively) suggest that igneous magnetite from porphyry Cu-Au deposits has higher Si, Ca, Y, Pb, Al, W, Ta, Nb, Mo, Sn, Mn, Mg, Ti, Zn, and Co average contents than that from porphyry Cu-Mo deposits (Fig. 6B).

Electron probe microanalysis shows that hydrothermal magnetite from porphyry Au-Cu deposits has higher Mg and Ti average contents than that from other deposit types, whereas that from porphyry Cu-Mo deposits has relatively high Cu and Cr contents (Fig. 6C). Hydrothermal magnetite from porphyry Cu-Mo-Au deposits has slightly higher K, Zn, and Ni average contents than that from other deposit types, whereas that from the porphyry W-Mo deposit has relatively high Si, Ca, Al, and Sn concentrations (Fig. 6C). Hydrothermal magnetite from the porphyry Cu-Au and Mo deposits has intermediate trace element contents compared to other deposit types (Fig. 6C). The LA-ICP-MS data of hydrothermal magnetite is from four deposit subtypes: porphyry Au-Cu, Cu-Au, Cu-Mo, and Cu-Mo-Au. Hydrothermal magnetite from porphyry Au-Cu deposits shows relatively high Zr, Nb, and Mn contents, whereas that from the porphyry Cu-Au deposits has higher Y, P, Pb, Hf, W, Sc, Ta, Mo, Ti, and Cr contents (Fig. 6D). Hydrothermal magnetite from porphyry Cu-Mo deposits has higher Ca and Cu contents, whereas that from Cu-Mo-Au deposits shows relatively high Ni and Cr contents (Fig. 6D).

Multivariate Statistical Analysis of Magnetite Composition

Igneous and hydrothermal magnetite

Figure 7 shows the PLS-DA results of EPMA and LA-ICP-MS data classified by magmatic and hydrothermal magnetite. PLS-DA of EPMA data shows that in contrast to hydrothermal magnetite that is dispersed in the t_1 - t_2 space, igneous magnetite is mainly isolated in the high t_1 region because of a positive correlation between V and Ti, which are negatively

correlated to Si and Ca (Fig. 7A, B, E-H). However, there is significant compositional overlap between igneous and hydrothermal magnetite (Fig. 7B) in terms of score contributions of Mg, Mn, Al, and Zn (Fig. 7E, F). Figure 7C and D shows PLS-DA results of LA-ICP-MS data that uses a higher number of elemental variables to differentiate between igneous and hydrothermal magnetite. Igneous magnetite mainly plots in the high t_1 , t_2 region due to positive correlation among V, Zr, P, Ti, Nb, and Mn, which are negatively correlated to Mg, Si, Co, Ni, Ge, Sb, W, and Pb (Fig. 7C, D, G, H). It is worth noting that V is more efficient than Ti in discriminating between igneous and hydrothermal magnetite, as shown by the higher score contribution for V (Fig. 7G, H). Score contribution plots show that contrasting element contributions discriminate igneous from hydrothermal magnetite (Fig. 7E-H).

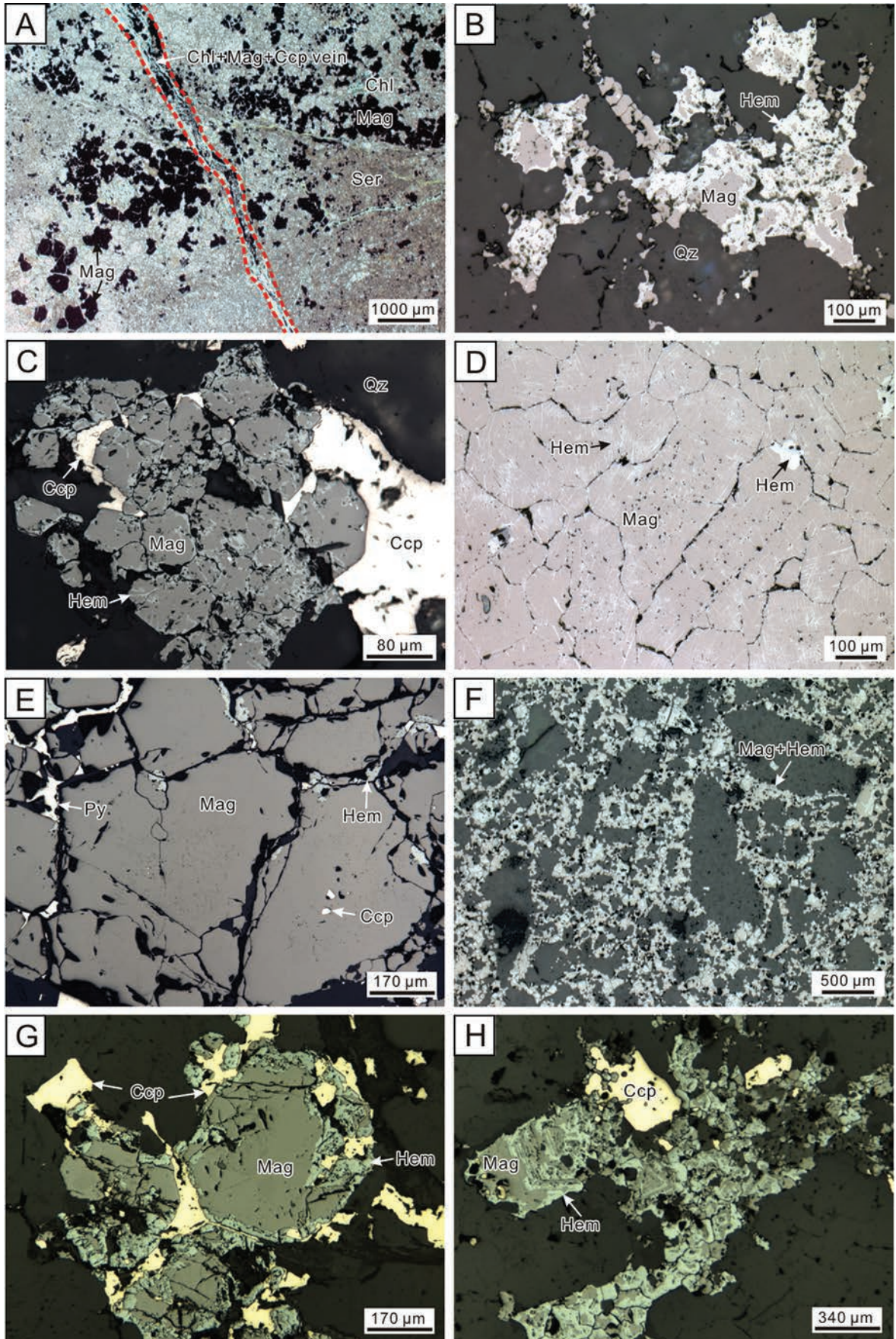
Deposit subtypes—igneous magnetite

Figure 8 shows the PLS-DA results of EPMA data of igneous magnetite classified by three deposit types: Cu-Au, Cu-Mo, and Cu-Mo-Au. Igneous magnetite from Cu-Au deposits mainly plots at positive t_1 due to correlated Mg and Al (Fig. 8A-C), whereas that from Cu-Mo deposits plots in the negative t_2 side due to correlated Mn, V, and Ca (Fig. 8B, D). Igneous magnetite from the Cu-Mo-Au deposits plots in the negative t_1 , positive t_2 region due to correlated V and Ca (Fig. 8B, E). In general, igneous magnetites from the three subtypes of deposits cannot be well discriminated from each other because of overlap in the t_1 - t_2 space. The VIP plot indicates that V and Al are the most important discriminant elements for these three deposit subtypes (Fig. 8F). Titanium is important to discriminate Cu-Mo-Au deposits, whereas Si is useful to discriminate Cu-Mo deposits (Fig. 8F). Magnesium is the important variable for Cu-Au deposits (Fig. 8F). Due to the limited number ($n = 11$) of LA-ICP-MS analyses for igneous magnetite and the larger number ($n = 25$) of element variables than analyses, PLS-DA of LA-ICP-MS data was not attempted.

Deposit subtypes—hydrothermal magnetite

Figure 9 shows PLS-DA results of EPMA data for hydrothermal magnetite classified by deposit subtypes. Hydrothermal magnetite from porphyry W-Mo deposit plots in the negative t_2 side and can be discriminated from other deposit subtypes

Fig. 2. Photomicrographs showing the occurrences of hydrothermal magnetite from the porphyry deposits. All images are under reflected light except image A, which is under transmitted light. A. Hydrothermal magnetite within chlorite-magnetite-chalcocopyrite veinlets from the Oyu Tolgoi Cu-Au-Mo deposit (sample Oyu Tolgoi). Magnetite is anhedral to subhedral and forms disseminated grains and aggregates in a strongly sericitized feldspath-rich rock. B. Hydrothermal magnetite in quartz vein from the Bajo de la Alumbrera Cu-Au deposit (sample 51-61). Magnetite is anhedral and partly replaced by hematite. C. Hydrothermal magnetite in quartz vein from Butte deposit (sample 7233D). Magnetite occurs as aggregates of anhedral grains associated with chalcocopyrite and shows evidence of martitization. Small inclusions of chalcocopyrite are common. D. Hydrothermal magnetite in thick magnetite veins from the Reko Diq Cu-Au deposit (sample RK 5). Subhedral magnetite forms massive aggregates and displays martitization along spinel planes. E. Hydrothermal magnetite in magnetite-chalcocopyrite-quartz-pyrite vein from Butte deposit (sample 11166-3199). Magnetite is anhedral, forms massive aggregates, is enclosed by chalcocopyrite and pyrite, hosts small inclusions of chalcocopyrite, and is slightly replaced by hematite along rims. F. Hydrothermal magnetite in magnetite-cemented breccia from Escondida Norte deposit (sample EN3). Magnetite occurs as small anhedral grains, partially or totally replaced by hematite (martitization). G. Anhedral to subhedral hydrothermal magnetite from the Kharmagtai Cu-Au deposit replaced by hematite and chalcocopyrite along the rims and fractures (sample Kharmagtai). H. Anhedral hydrothermal magnetite from the Skouries Cu-Au deposit showing oscillatory zoning, nearly totally replaced by hematite (sample 1836). Some magnetite grains were completely replaced by chalcocopyrite resulting in the formation of small magnetite inclusions in chalcocopyrite. Abbreviations: Ccp = chalcocopyrite, Chl = chlorite, Hem = hematite, Mag = magnetite, Py = pyrite, Qz = quartz, Ser = sericite.



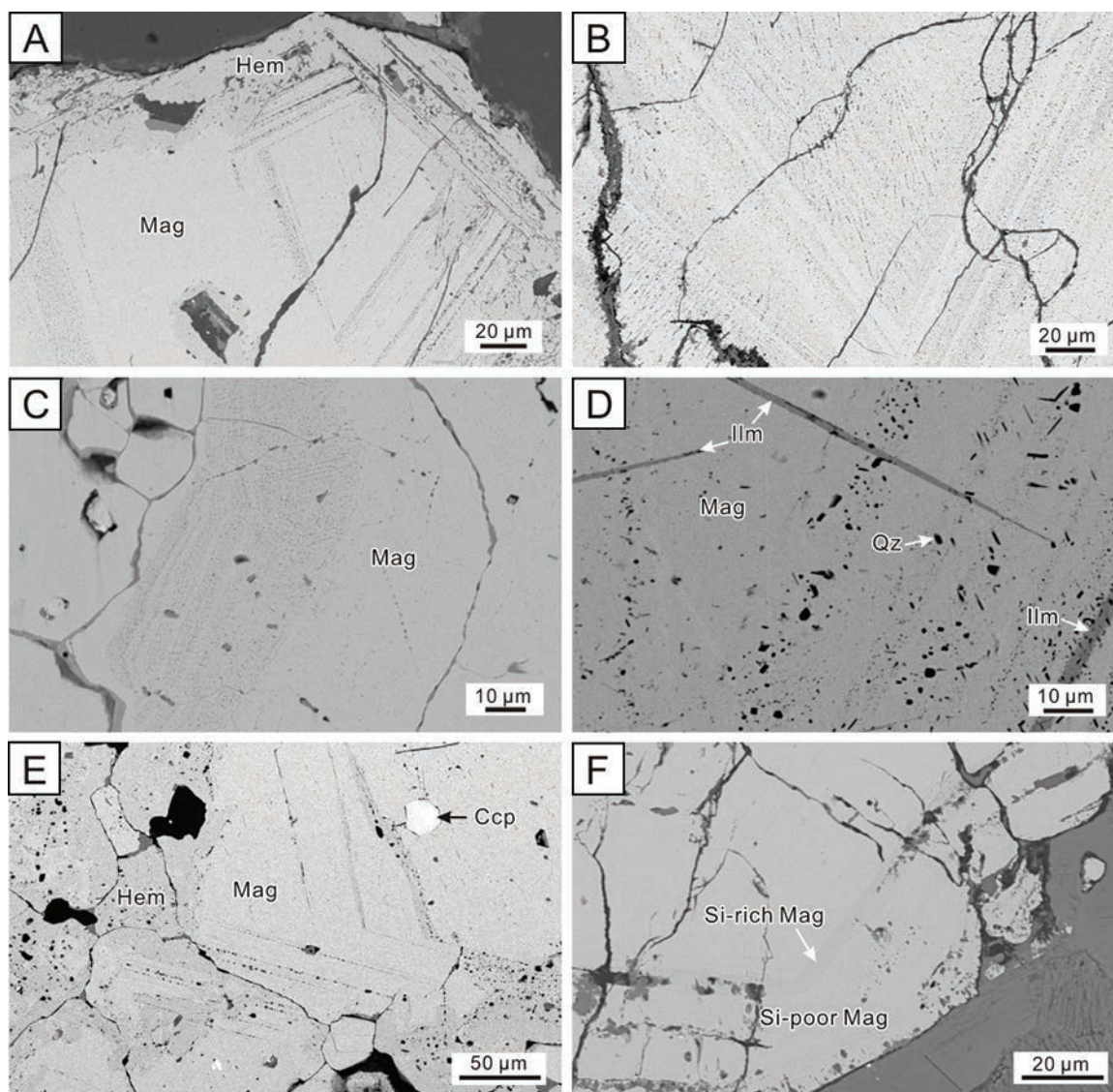


Fig. 3. Backscattered electron images of zoned magnetite from porphyry deposits. A, B. Hydrothermal magnetite from the Kharmagtai Cu-Au deposit showing zoned textures composed of dark-gray and light-gray domains (sample Kharmagtai). The dark-gray domains are composed of small silicate inclusions. C, D. Hydrothermal magnetite in magnetite-quartz vein from the Bajo de la Alumbrera Cu-Au deposit. Quartz inclusions and minor ilmenite exsolution lamellae are observed in magnetite. E. Hydrothermal magnetite from the Endako porphyry Mo deposit showing oscillatory zoning that was replaced by hematite (sample 2071). There are also minor chalcopyrite inclusions in magnetite. F. Hydrothermal magnetite from the Mount Pleasant porphyry W-Mo deposit composed of Si-rich (dark gray) and Si-poor (light gray) domains (sample SC1). Abbreviations: Ccp = chalcopyrite, Hem = hematite, Ilm = ilmenite, Mag = magnetite, Qz = quartz.

due to correlated Si and Al (Fig. 9A, B). Hydrothermal magnetite from the porphyry Mo deposit mainly plots at positive t_1 due to correlated Ti and Mg in spite of overlap with that from porphyry Cu-Au deposits (Fig. 9A, B). Hydrothermal magnetites from porphyry Au-Cu, Cu-Au, Cu-Mo, and Cu-Mo-Au deposits is scattered in the t_1 - t_2 plot and cannot be discriminated from each other (Fig. 9A, B). However, hydrothermal magnetite from porphyry Au-Cu deposits can be roughly discriminated from other deposit subtypes in the t_1 - t_3 plot by a high Mg score (Fig. 9C, D). Score contribution plots indicate that hydrothermal magnetite from different deposit subtypes has specific trace element characteristics relative to the whole data set. For example, hydrothermal magnetite from

porphyry Au-Cu deposits is discriminated by a positive contribution of Mg (Fig. 9E), whereas that from the Cu-Au and Mo deposits is mainly discriminated by positive contributions of Ti, Al, and Mg (Fig. 9F, I). Positive contributions of V, Ca, and Si characterize hydrothermal magnetite from porphyry Cu-Mo deposits (Fig. 9G), whereas positive contributions of Zn, Al, Si, and Mg are typical of hydrothermal magnetite from porphyry Cu-Mo-Au deposits (Fig. 9H). Hydrothermal magnetite from porphyry W-Mo deposits is distinguished by positive contributions of Al and Si (Fig. 9J). The VIP plot indicates that Si is an important discriminant element for all deposit subtypes with the exception of Au-Cu deposits, whereas Mg is important for discriminating all deposit subtypes with the

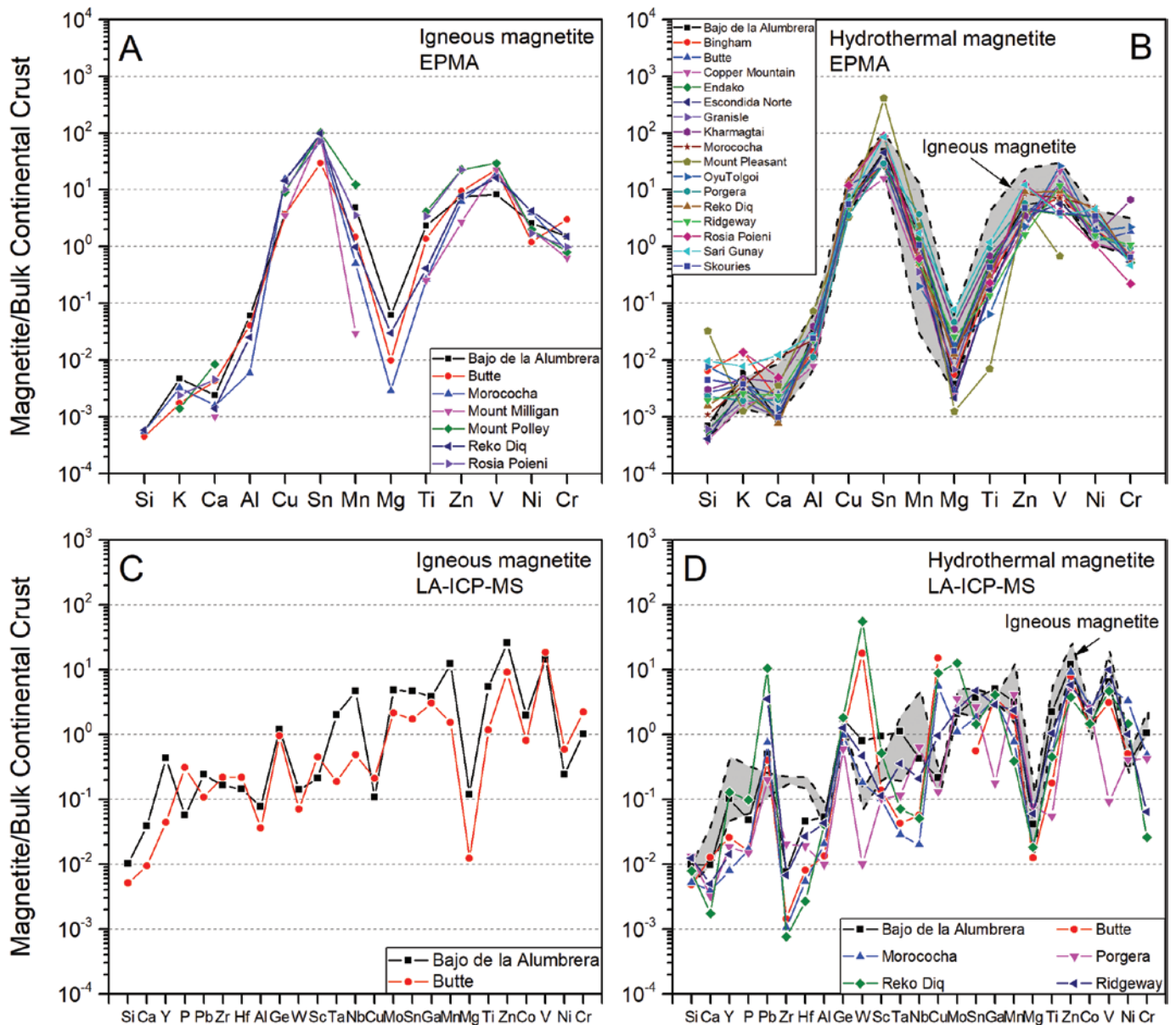


Fig. 4. Multi-element diagrams of average trace element composition of magnetite from individual deposits, normalized to bulk continental crust (Rudnick and Gao, 2003). Gray areas in B and D represent compositional ranges for igneous magnetite in A and C, respectively. A, B. EPMA data of igneous and hydrothermal magnetite. C, D. LA-ICP-MS data of igneous and hydrothermal magnetite.

exception of W-Mo deposits (Fig. 9K). Zinc and Al are important in discriminating hydrothermal magnetite from the Cu-Mo-Au and W-Mo deposits, although Al is also important for Au-Cu deposits (Fig. 9K). Vanadium is an important discriminant element for Cu-Au and Mo deposits (Fig. 9K).

Figure 10 shows the PLS-DA results of LA-ICP-MS data of hydrothermal magnetite classified by four deposit subtypes: Au-Cu, Cu-Au, Cu-Mo, and Cu-Mo-Au. Hydrothermal magnetite from the Au-Cu deposits plots in the negative t_1 side due to correlated Mg, Mn, Co, Zr, Nb, Sn, and Hf, whereas that from Cu-Au deposits mainly plots in the positive t_1 , negative t_2 region due to correlated Al, Sc, Ti, W, Pb, and Y (Fig. 10A, B). Hydrothermal magnetite from Cu-Mo and

Cu-Mo-Au deposits plots in the positive t_1 , positive t_2 region because of correlated Ga, V, Cu, Sb, and Ge (Fig. 10A, B). Hydrothermal magnetites from Au-Cu, Cu-Au, and Cu-Mo-Au deposits can be discriminated from each other, whereas hydrothermal magnetite from Cu-Mo deposits partly overlaps that from Cu-Au and Cu-Mo-Au deposits. Score contribution plots show that positive contributions of Mg, Mn, Co, Zr, Nb, Sn, and Hf discriminate hydrothermal magnetite from the Au-Cu deposits, whereas positive contributions of Sc, Al, Ti, V, Ga, Ta, W, and Pb characterize hydrothermal magnetite from Cu-Au deposits (Fig. 10C, D). Hydrothermal magnetite from Cu-Mo deposits is discriminated by positive contributions of Ca, V, Mn, Cu, Zn, Ga, and W, whereas that from

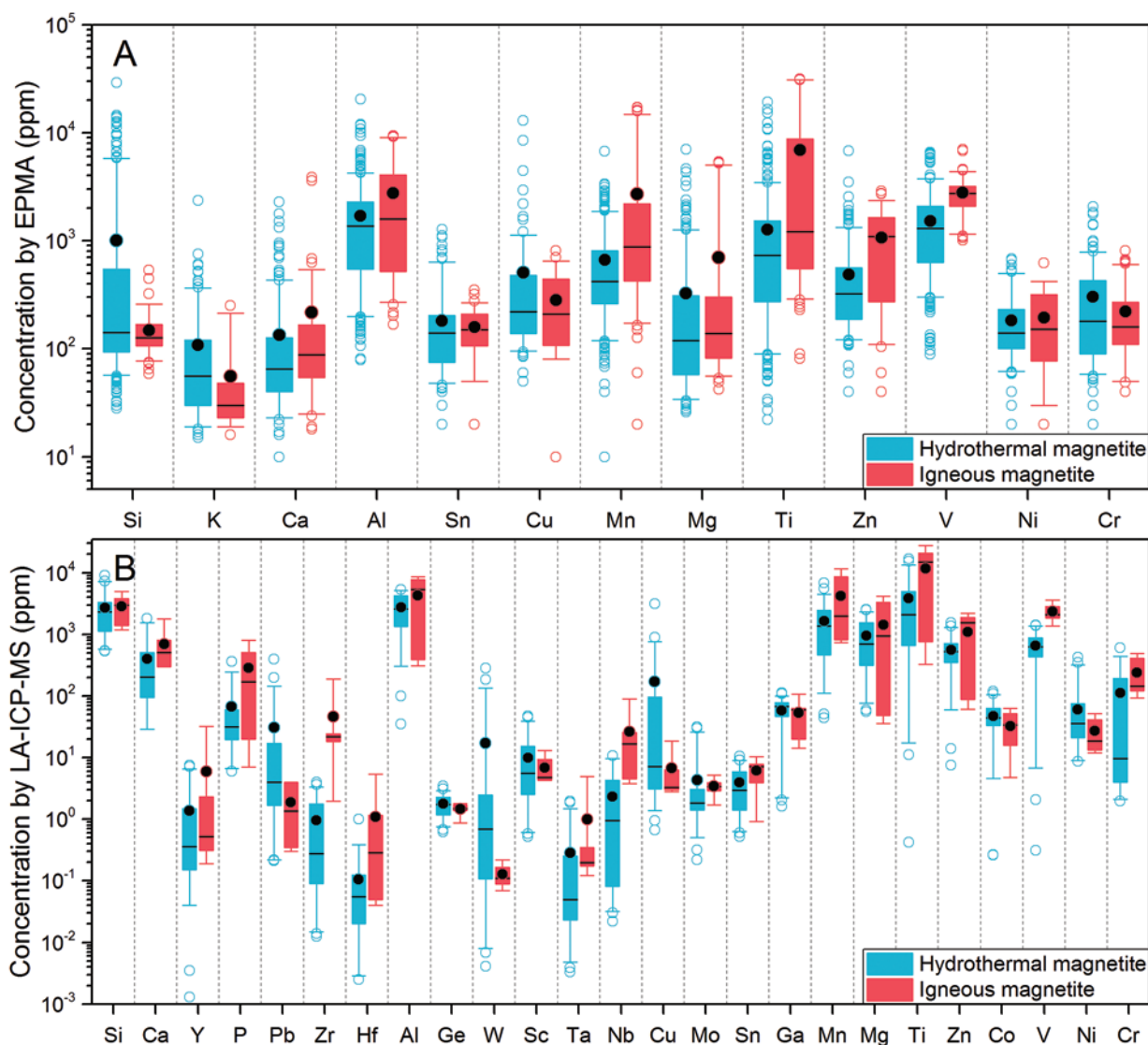


Fig. 5. Box and whisker plots of trace elements in igneous and hydrothermal magnetite analyzed by EPMA (A) and by LA-ICP-MS (B). The upper and lower margins of the box represent the upper 75% and lower 25% of the data. The whiskers represent the upper and lower threshold values (95% data). Median values are shown as solid black lines and mean values as solid black circles. Outliers are shown as open circles along the whisker. Data below detection limit are removed from this plot.

Cu-Mo-Au deposits is separated by positive contributions of V, Co, Ni, Zn, and Ga (Fig. 10E, F). The VIP plot indicates that Sc, Mn, and Co are important discriminant elements for all deposit subtypes (Fig. 10G). Aluminum and Sn are important in discriminating Au-Cu, Cu-Mo, and Cu-Mo-Au deposits, whereas V, Ga, Zr, and Nb are important discriminant elements for Au-Cu and Cu-Au deposits (Fig. 10G).

Magmatic affinity—igneous magnetite

Figure 11 shows the PLS-DA results of EPMA data of igneous magnetite classified by magmatic affinity. In spite of overlapping in t_1 - t_2 space, igneous magnetite associated with alkaline intrusions plots in the positive t_2 side due to correlated Si and Al (Fig. 11A-C), whereas that associated with high-K calc-alkaline intrusions plots in the positive t_1 , negative t_2 region due to correlated Ti, Mg, and Al (Fig. 11A, B, E). Igneous magnetite associated with calc-alkaline intrusions is scattered

in the t_1 - t_2 plot, characterized by positive contributions of Zn, V, and Ca (Fig. 11A, B, D). The VIP plot shows that Al is important to discriminate all types of igneous magnetite (Fig. 11F). Zinc and Ca are useful discriminant elements for igneous magnetite associated with calc-alkaline and high-K calc-alkaline intrusions (Fig. 11F). Vanadium is only useful in discriminating igneous magnetite associated with calc-alkaline intrusions, whereas Si is useful in discriminating igneous magnetite associated with alkaline and high-K calc-alkaline intrusions (Fig. 11F). PLS-DA of LA-ICP-MS was not performed due to limited data for igneous magnetite grouped by magmatic affinity.

Magmatic affinity—hydrothermal magnetite

Partial least squares-discriminant analysis of EPMA data shows that hydrothermal magnetite associated with high-K calc-alkaline intrusions mainly plots at negative t_2 due to

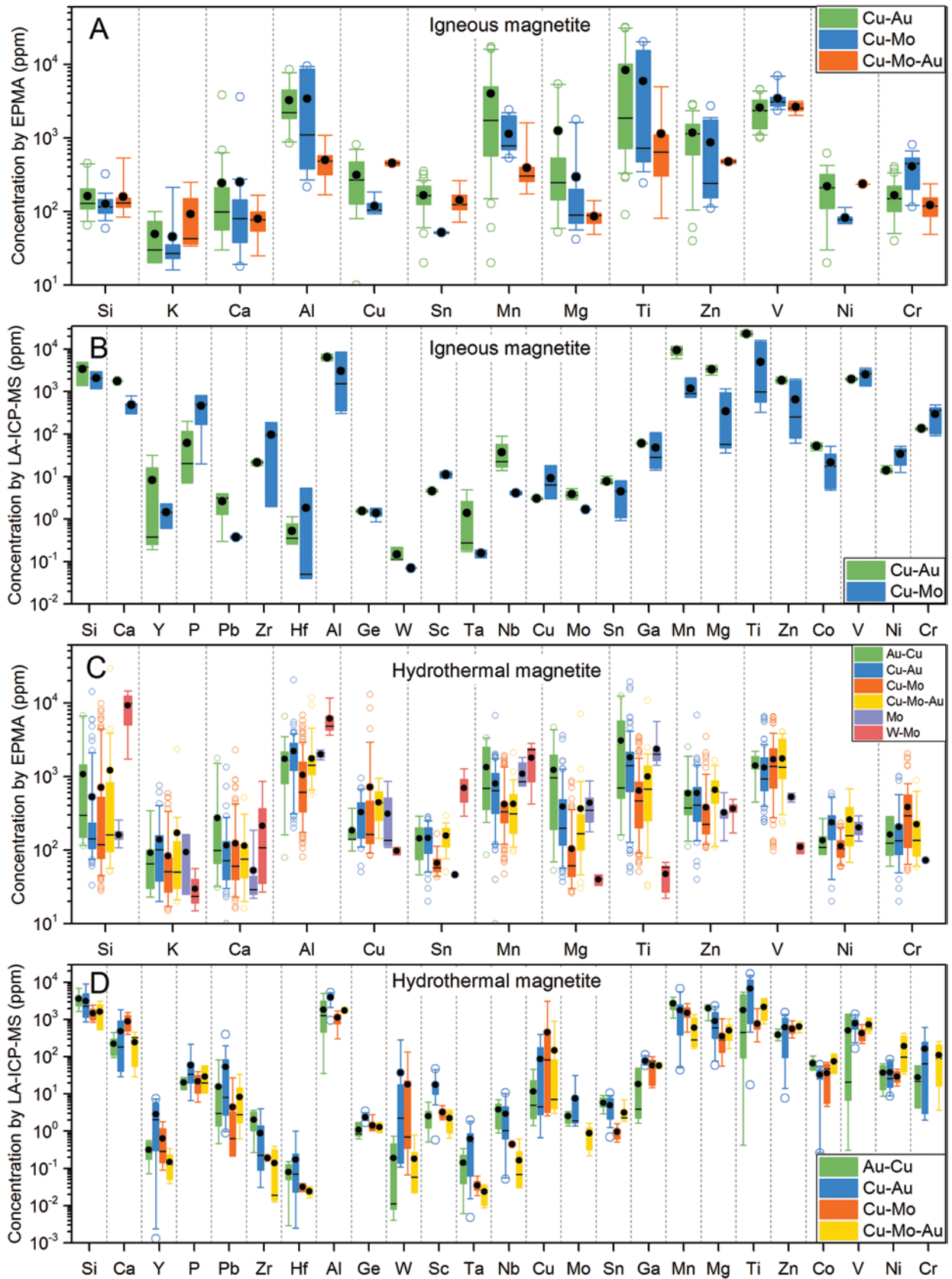


Fig. 6. Box and whisker plots of trace elements in igneous and hydrothermal magnetite from different types of porphyry deposits. A and C are EPMA data, whereas B and D are LA-ICP-MS data. The meaning of symbols in box and whisker plot is the same as in Figure 5. Data below detection limit are removed from this plot.

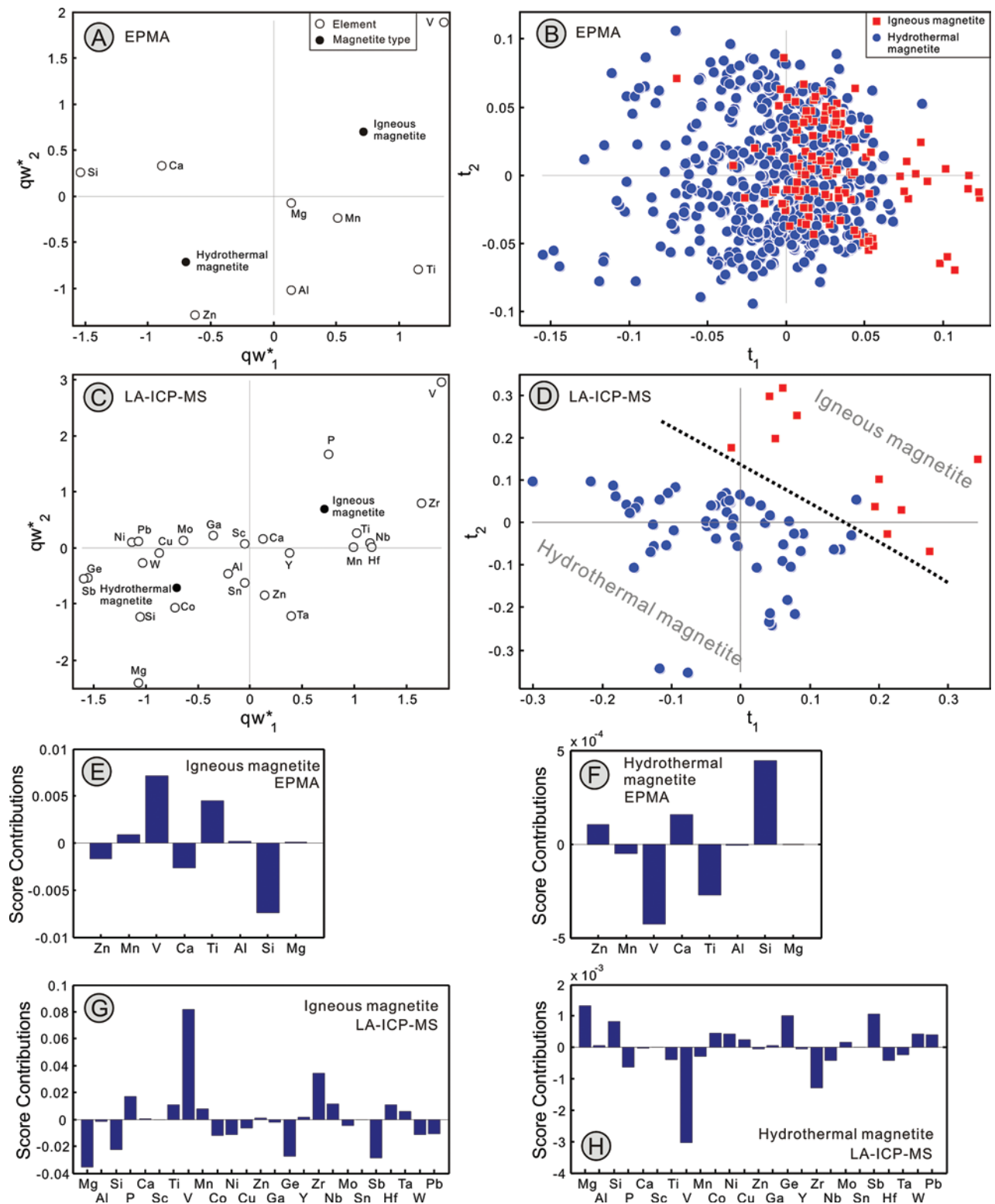


Fig. 7. PLS-DA of EPMA (A, B) and LA-ICP-MS (C, D) data of igneous and hydrothermal magnetite from the studied deposits. A. The qw_1^* - qw_2^* (first and second loadings) plot based on EPMA data showing correlations among element variables and magnetite type. B. The t_1 - t_2 (first and second scores) plot showing the distribution of individual analyses of samples in the latent variable space defined by qw_1^* - qw_2^* in A. C. The qw_1^* - qw_2^* (first and second loadings) plot based on LA-ICP-MS data showing correlations among element variables and magnetite type. D. The t_1 - t_2 (first and second scores) plot showing the distribution of individual analyses of samples in the latent variable space defined by qw_1^* - qw_2^* in C. Dotted line in D roughly separates igneous from hydrothermal magnetite. E-H. Score contribution plots of elements for igneous and hydrothermal magnetite.

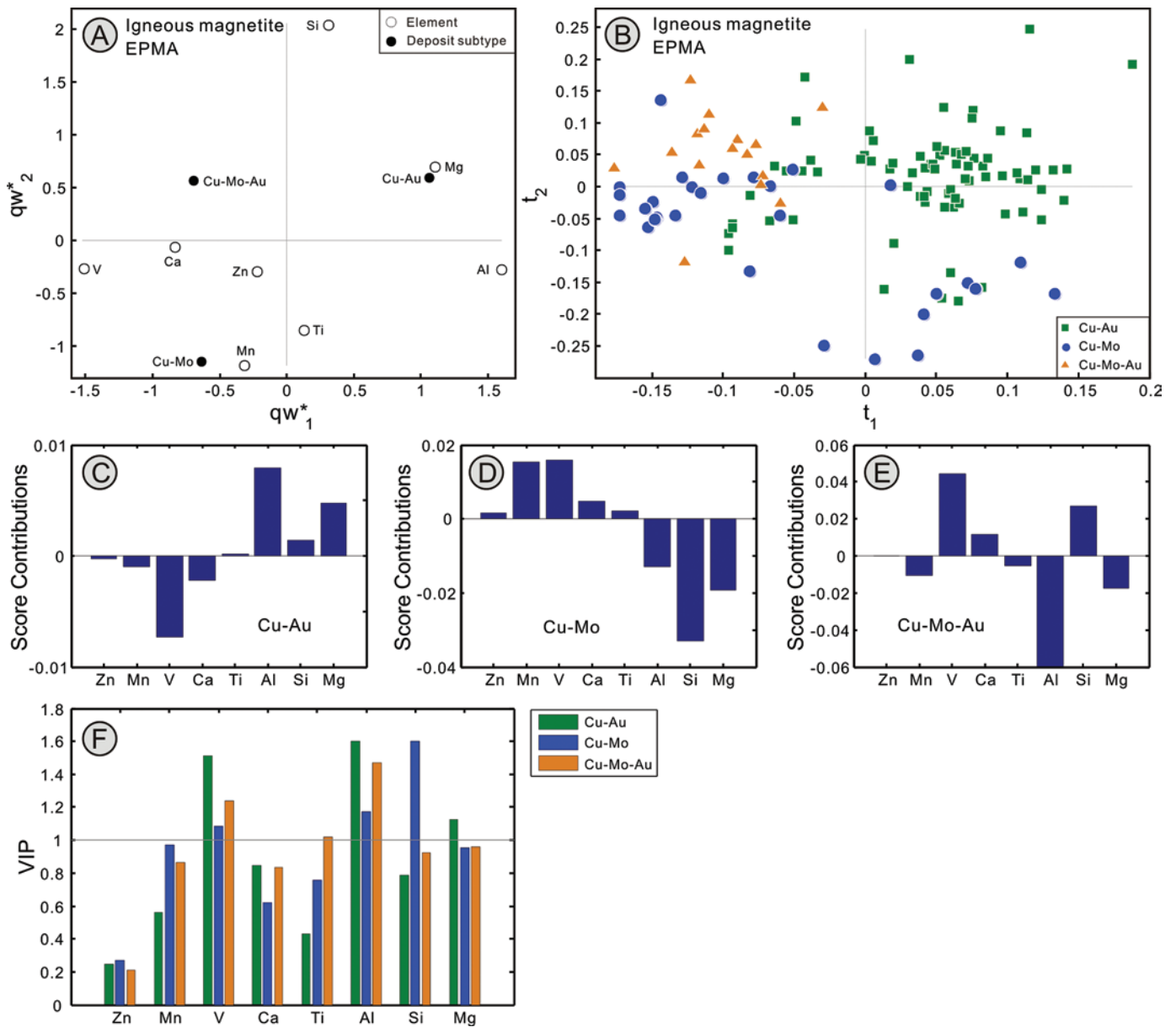


Fig. 8. PLS-DA of EPMA data of igneous magnetite from porphyry Cu-Au, Cu-Mo, and Cu-Mo-Au deposits. A. The qw^*_1 - qw^*_2 (first and second loadings) plot showing correlations among element variables and deposit subtypes. B. The t_1 - t_2 (first and second scores) plot showing the distribution of individual analyses of samples in the latent variable space defined by qw^*_1 - qw^*_2 in A. C-E. Score contribution plots of elements for hydrothermal magnetite from different types of mineralization. F. The VIP plot showing the importance of compositional variables in classification of samples in B. Gray line in F represents the VIP value of 1. Elements with VIP value higher than 1 are the most important in the classification.

correlated Al and Mn (Fig. 12A, B). Hydrothermal magnetite associated with alkaline and calc-alkaline intrusions is scattered in t_1 - t_2 space. In general, hydrothermal magnetites associated with intrusions of different magmatic affinities cannot be discriminated from each other from EPMA data (Fig. 12B). Score contribution plots show that positive contribution of Mg discriminates hydrothermal magnetite associated with alkaline intrusions, whereas positive contributions of Zn, V, Ca, and Si discriminate that associated with calc-alkaline intrusions (Fig. 12C, D). Hydrothermal magnetite associated with high-K calc-alkaline intrusions

is discriminated by positive contributions of Mn, Ti, and Al (Fig. 12E). The VIP plot shows that Al and Mg are important discriminating elements for hydrothermal magnetite associated with intrusions of all magmatic affinities (Fig. 12F). Zinc and Ti discriminate hydrothermal magnetite associated with calc-alkaline and high-K calc-alkaline intrusions (Fig. 12F).

Laser ablation-inductively coupled plasma-mass spectrometry data yield a better classification for hydrothermal magnetite associated with intrusions of different magmatic affinities (Fig. 13A, B). Hydrothermal magnetite associated

with alkaline intrusions is discriminated by positive contributions of Mg, Mn, Co, Zr, Nb, Mo, Sn, Hf, and Ta (Fig. 13A-C), whereas that associated with calc-alkaline intrusions is discriminated by positive contributions of V, Ni, Cu, Ga, Ge, Sb, and W (Fig. 13A, B, D). Hydrothermal magnetite associated with high-K calc-alkaline intrusions plots at positive t_2 due to correlated Sc, Ti, Al, Ta, and Hf (Fig. 13A, B, E). The VIP plot shows that V, Ni, Ga, and Ta are important discriminant elements for all types of hydrothermal magnetite (Fig. 13F). Magnesium, Mn, Cu, Zr, Nb, Sn, Hf, and W are useful in discriminating hydrothermal magnetite associated with alkaline and calc-alkaline intrusions (Fig. 13F). Aluminum, Co, and Mo are only useful in discriminating hydrothermal magnetite associated with high-K calc-alkaline intrusions (Fig. 13F). Scandium and Ti are useful in discriminating hydrothermal magnetite associated with alkaline and high-K calc-alkaline intrusions (Fig. 13F).

Porphyry composition—igneous magnetite

Partial least squares-discriminant analysis of EPMA data of igneous magnetite shows that intermediate porphyry cannot be separated from felsic porphyry in the t_1 - t_2 space (Fig. 14A, B). Igneous magnetite from intermediate porphyry is scattered in the t_1 - t_2 space with positive contributions of Al, Si, and Mg (Fig. 14C), whereas that from felsic porphyry plots in the negative t_1 region (Fig. 14A, B) due to positive contributions of Mn and V (Fig. 14D). Because there are only four and seven LA-ICP-MS analyses for igneous magnetite from intermediate and felsic porphyry, respectively, PLS-DA was not performed on igneous magnetite grouped by porphyry composition.

Porphyry composition—hydrothermal magnetite

Figure 15 shows PLS-DA results of EPMA data of hydrothermal magnetite related to different porphyry compositions.

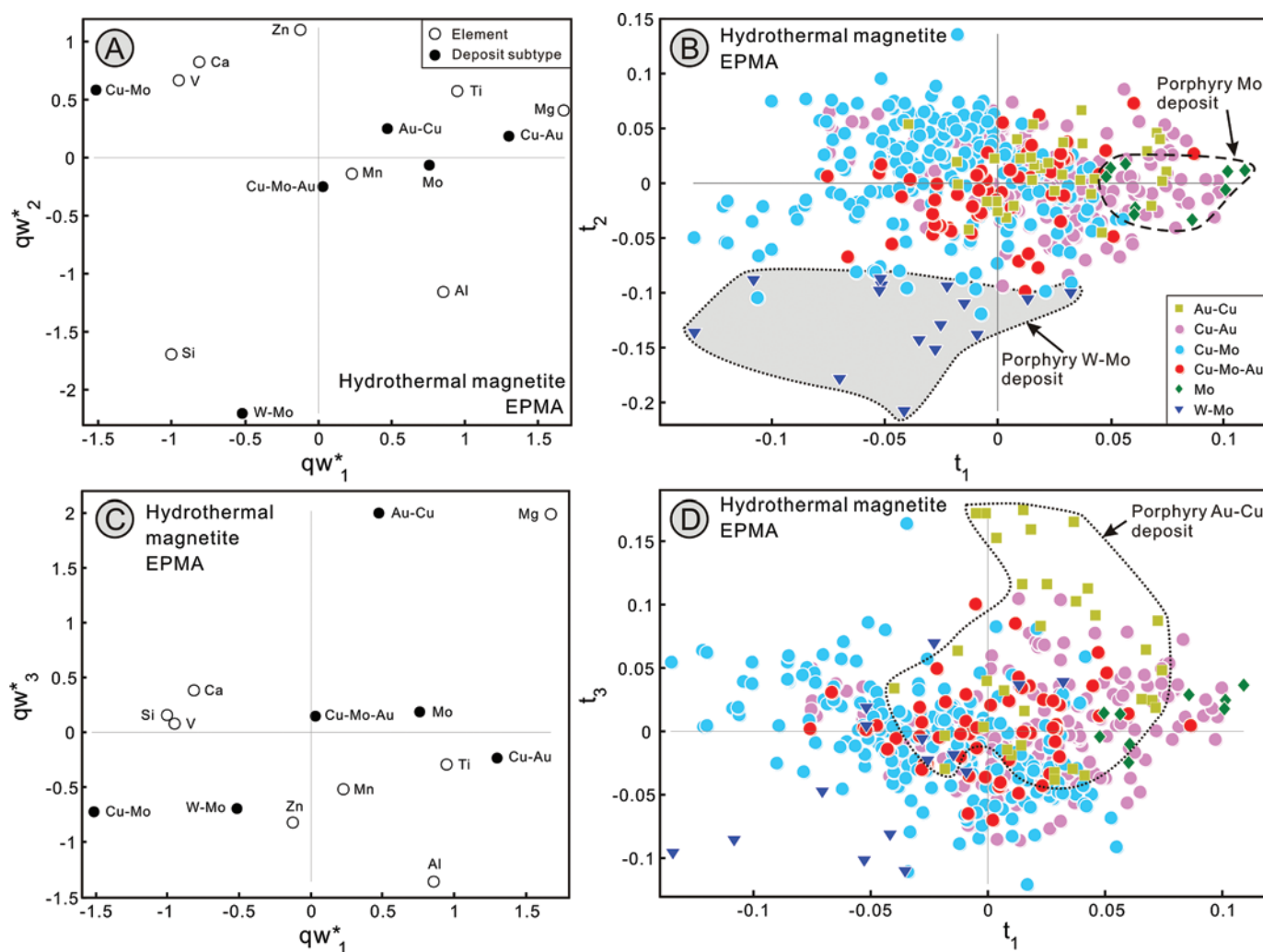


Fig. 9. PLS-DA of EPMA data of hydrothermal magnetite from different types of porphyry deposits. A. The qw^*_1 - qw^*_2 (first and second loadings) plot showing correlations among element variables and deposit subtypes. B. The t_1 - t_2 (first and second scores) plot showing the distribution of individual analyses of samples in the latent variable space defined by qw^*_1 - qw^*_2 in A. C. The qw^*_1 - qw^*_3 (first and third loadings) plot showing correlations among element variables and deposit subtypes. D. The t_1 - t_3 (first and third scores) plot showing the distribution of individual analyses of samples in the latent variable space defined by qw^*_1 - qw^*_3 in C.

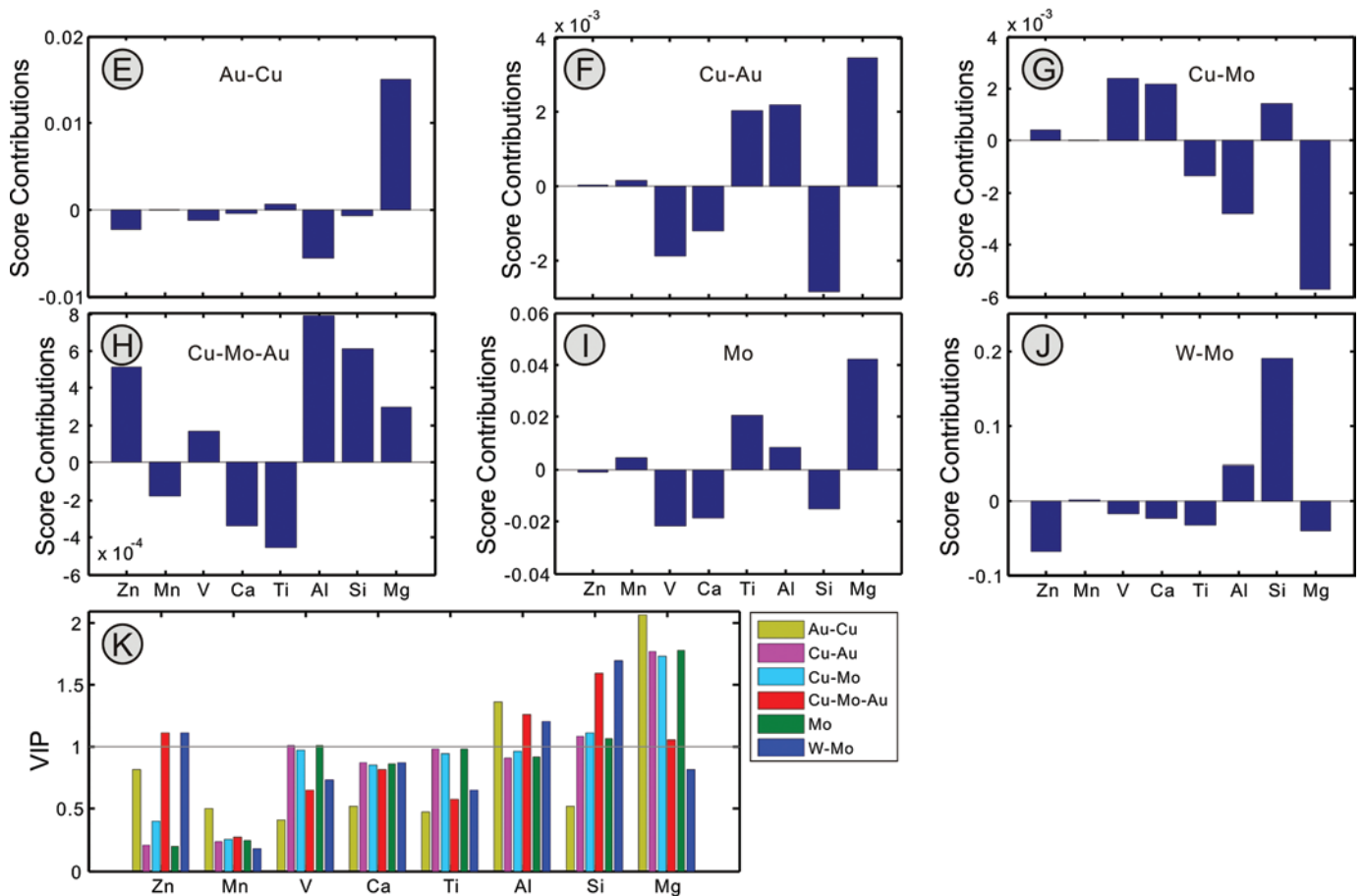


Fig. 9. (Cont.) E-J. Score contribution plots of elements for hydrothermal magnetite from different types of mineralization. K. The VIP plot showing the importance of compositional variables in classification of samples in B and D. Gray line in K represents the VIP value of 1. Elements with VIP value higher than 1 are the most important in the classification.

Hydrothermal magnetite related to mafic porphyry can be discriminated from that related to intermediate and felsic porphyry due to positive contributions of Mg and Mn (Fig. 15A-C). However, hydrothermal magnetites related to intermediate and felsic porphyry cannot be separated from each other in the t_1 - t_2 space (Fig. 15A, B). Score contribution plots show that hydrothermal magnetite related to intermediate porphyry is characterized by positive contributions of Mg and Al (Fig. 15D), whereas that related to felsic porphyry is characterized by weakly positive contributions of Si, Ca, and V (Fig. 15E). Magnesium and Al are the most important discriminant elements for three types of porphyry, whereas Mn is only useful in discriminating mafic porphyry (Fig. 15F).

Partial least squares-discriminant analysis of LA-ICP-MS data of hydrothermal magnetite shows that mafic, intermediate, and felsic porphyries are discriminated from each other. Hydrothermal magnetite related to mafic porphyry plots in the negative t_1 region (Fig. 16A, B) because of positive contributions of Mg, Mn, Co, Zr, Nb, Mo, Sn, and Hf (Fig. 16C). Hydrothermal magnetite related to intermediate porphyry mainly plots in the positive t_1 , positive t_2 region due to positive contributions of Al, Sc, Ti, V, Ga, Sn, and Pb (Fig. 16D), whereas that related to felsic porphyry plots in the positive t_1 , negative t_2 region due to positive contributions of Ca, Mn,

Cu, Zn, and W (Fig. 16E). VIP plots show that Mg, Al, Ti, and Mn are the most important discriminant elements for three different porphyries (Fig. 16F). Vanadium, Ga, Zr, and Nb are useful in discrimination between mafic and intermediate porphyries, whereas Cu, Zn, Sn, W, and Pb are important to discriminate between intermediate and felsic porphyries (Fig. 16F). Calcium and Ta are only useful in discriminating hydrothermal magnetite related to felsic porphyry (Fig. 16F).

Discussion

Igneous versus hydrothermal processes

The compositional variations of igneous magnetite are mainly attributed to the conditions of temperature, f_{O_2} and f_{S_2} , melt composition, cooling rate, subsolidus reequilibration processes, and element partitioning with coprecipitated minerals (Buddington and Lindsley, 1964; Ghiorso and Sack, 1991; Frost and Lindsley, 1992; Dare et al., 2012, 2014; Nadoll et al., 2014). Experimental studies have demonstrated that magnetite-melt or magnetite-mineral partition coefficients of elements in igneous magnetite depend mostly on temperature, host rock/melt composition, and oxygen/sulfur fugacity (Toplis and Corgne, 2002; Sievwright et al., 2017; Sossi et al., 2018) and can vary across three to five orders of magnitude

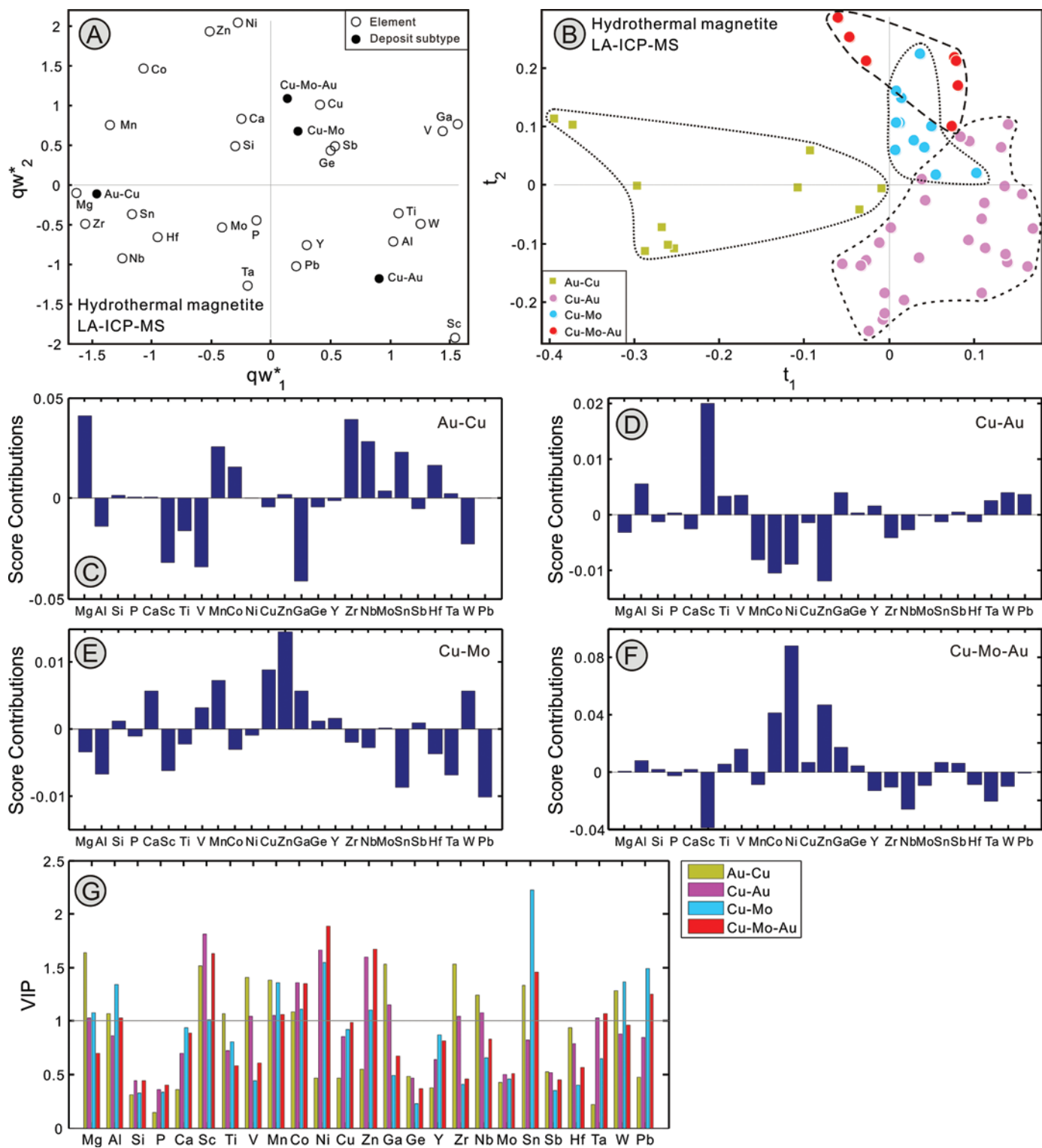


Fig. 10. PLS-DA of LA-ICP-MS data of hydrothermal magnetite from different types of porphyry deposits. A. The qw^*_1 - qw^*_2 (first and second loadings) plot showing correlations among element variables and deposit subtypes. B. The t_1 - t_2 (first and second scores) plot showing the distribution of individual analyses of samples in the latent variable space defined by qw^*_1 - qw^*_2 in A. C-F. Score contribution plots for hydrothermal magnetite from different types of mineralization. G. The VIP plot showing the importance of compositional variables in classification of samples in B. Gray line in G represents the VIP value of 1. Elements with VIP value higher than 1 are the most important in the classification.

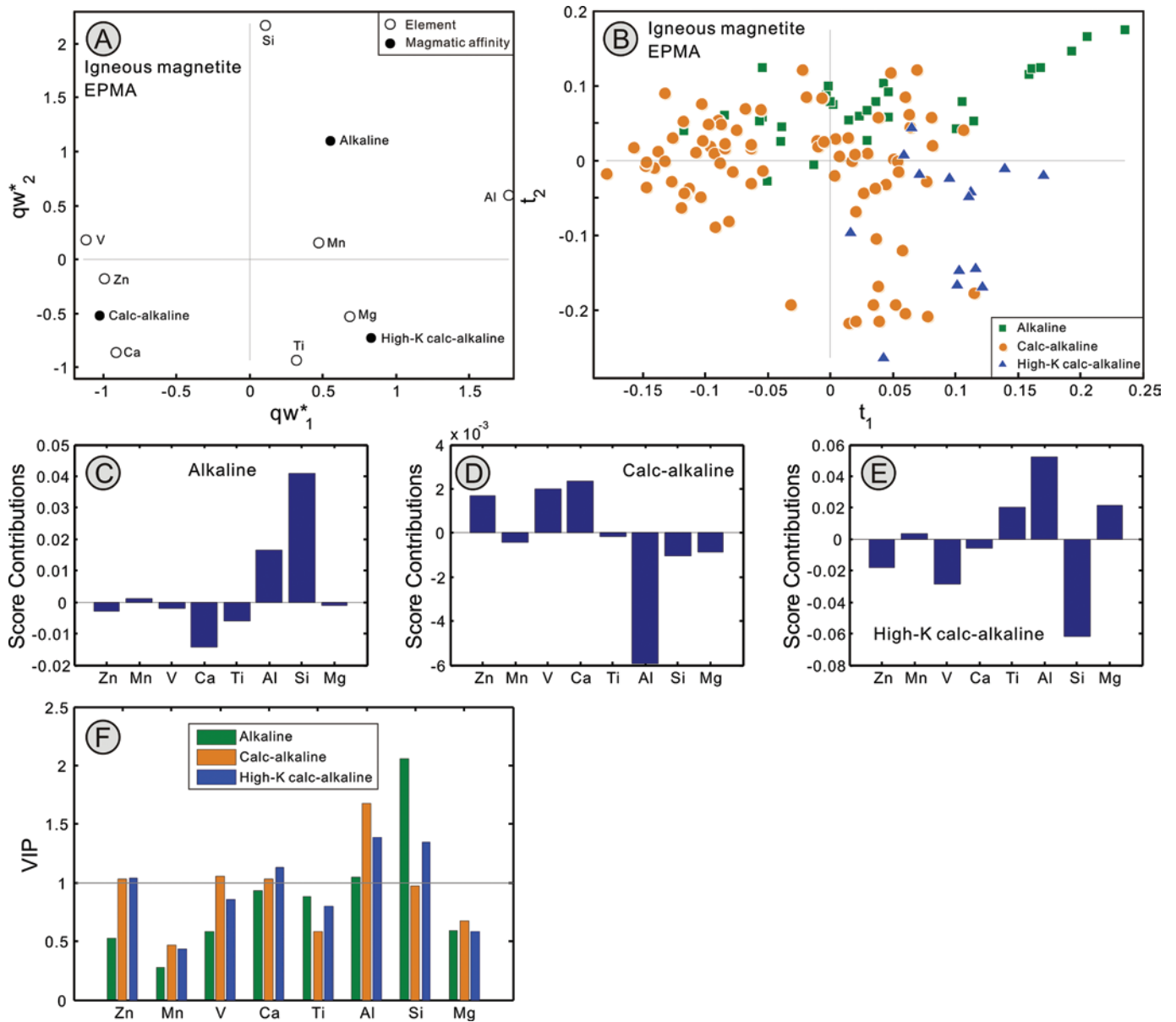


Fig. 11. PLS-DA of EPMA data of igneous magnetite grouped by magmatic affinity of porphyry intrusions. A. The qw^*_1 - qw^*_2 (first and second loadings) plot showing correlations among element variables and magmatic affinity. B. The t_1 - t_2 (first and second scores) plot showing the distribution of individual analyses of samples in the latent variable space defined by qw^*_1 - qw^*_2 in A. C-E. Score contribution plots of elements for igneous magnetite associated with different magmatic affinities. F. The VIP plot showing the importance of compositional variables in classification of samples in B. Gray line in F represents the VIP value of 1. Elements with VIP value higher than 1 are the most important in the classification.

for a specific element (Dare et al., 2012; Nadoll et al., 2014). Despite the limited experimental work available on partitioning of trace elements between magnetite and hydrothermal fluids (Chou and Eugster, 1977; Ilton and Eugster, 1989; Simon et al., 2004), the composition of hydrothermal magnetite appears to be controlled by the fluid composition (element availability), temperature, f_{O_2} and f_{S_2} , and host-rock buffering (Nadoll et al., 2014). Hydrothermal magnetite has higher Si, K, Pb, Ge, W, Sc, Cu, Mo, Ga, Co, and Ni but lower Ca, Y, P, Zr, Hf, Al, Ta, Nb, Mn, Mg, Ti, Zn, and V contents than igneous magnetite in terms of average values (Fig. 5A, B). PLS-DA results show that relatively high Mg, Si, Ca, Co,

Ni, Ge, Sb, W, and Pb discriminates hydrothermal magnetite, whereas relatively high P, Ti, V, Mn, Zr, Nb, Hf, and Ta discriminates igneous magnetite (Fig. 7). In this section, we discuss the main factors controlling the compositional differences between igneous and hydrothermal magnetite.

The observation that Ti and V contents are higher in igneous magnetite compared to hydrothermal magnetite in porphyry systems is consistent with the study of Nadoll et al. (2015) that focuses on both porphyry and skarn systems. The Ti versus V diagram was proposed to discriminate igneous from hydrothermal magnetite based on this observation (Nadoll et al., 2015). This observation is also consistent with findings that

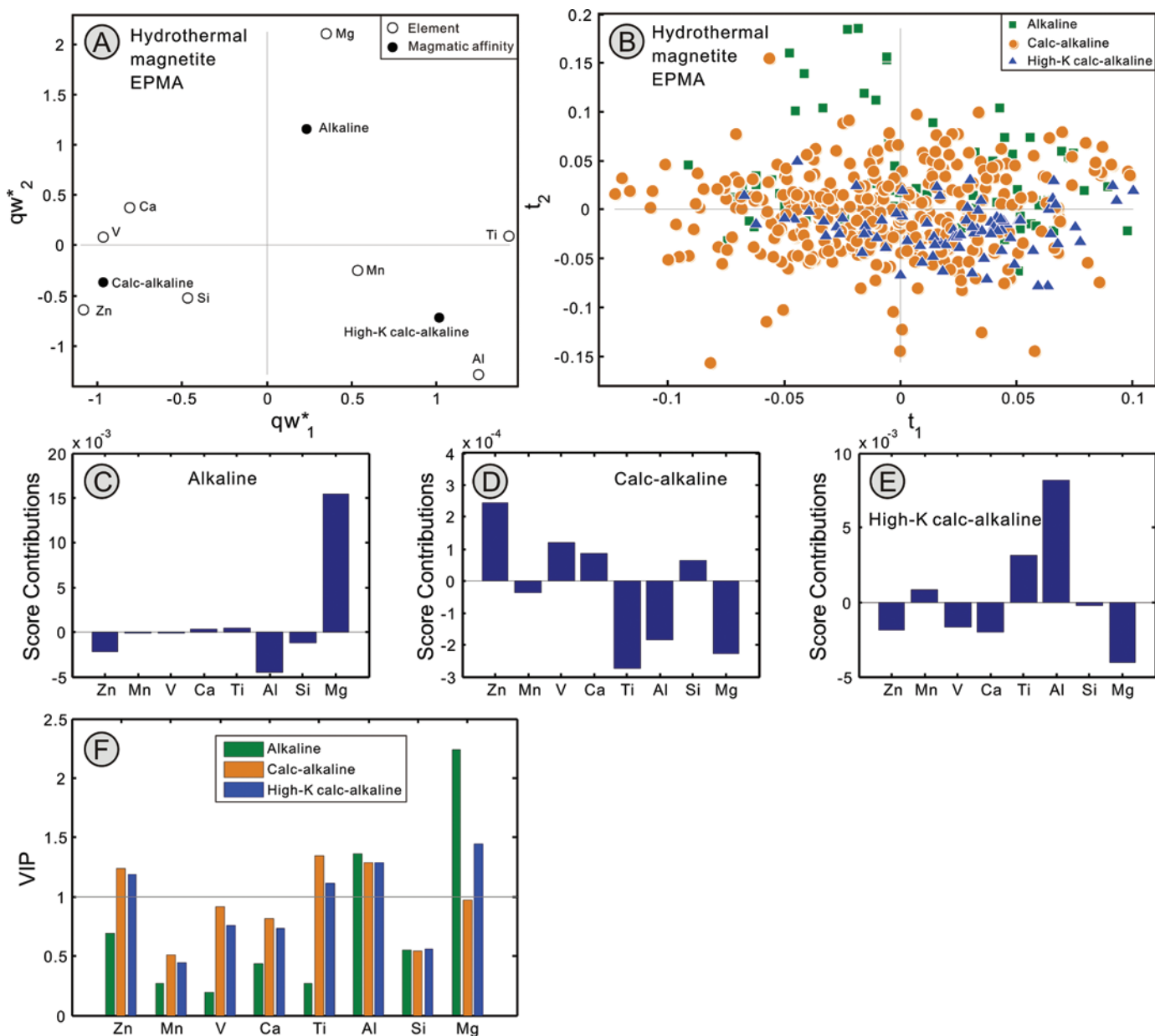


Fig. 12. PLS-DA of EPMA data of hydrothermal magnetite grouped by magmatic affinity of porphyry intrusions. A. The qw^*_1 - qw^*_2 (first and second loadings) plot showing correlations among element variables and magmatic affinity. B. The t_1 - t_2 (first and second scores) plot showing the distribution of individual analyses of samples in the latent variable space defined by qw^*_1 - qw^*_2 in A. C-E. Score contribution plots of elements for hydrothermal magnetite associated with different magmatic affinities. F. The VIP plot showing the importance of compositional variables in classification of samples in B. Gray line in F represents the VIP value of 1. Elements with VIP value higher than 1 are the most important in the classification.

magmatic magnetite from Fe-Ti-(V) deposits commonly has Ti + V contents higher than hydrothermal magnetite from magmatic-hydrothermal deposits such as IOCG and porphyry Cu (Dupuis and Beaudoin, 2011). Higher Ti and V contents in igneous magnetite are likely due to strong compatibility of Ti and V in magnetite crystallized from silicate melt ($D_{Ti} = 7.0$, $D_V = 26$; Dare et al., 2012) and relatively lower solubility of these elements in aqueous fluids (Mysen, 2012). Because the partition of Ti and V into magnetite is preferred with increasing temperature and decreasing oxygen fugacity, respectively

(Nielsen et al., 1994; Toplis and Carroll, 1995; Toplis and Corgne, 2002; Sievwright et al., 2017), decreased Ti and V contents from igneous to hydrothermal magnetite reflect decreasing temperature and increasing oxygen fugacity from magmatic to hydrothermal process.

Phosphorus is incompatible in igneous magnetite ($D_P = 0.0028$; Dare et al., 2012) and therefore tends to concentrate in late magma after progressive fractional crystallization, for example, to form Fe-Ti-P mineralization. Phosphorus contents in both igneous and hydrothermal magnetite are commonly

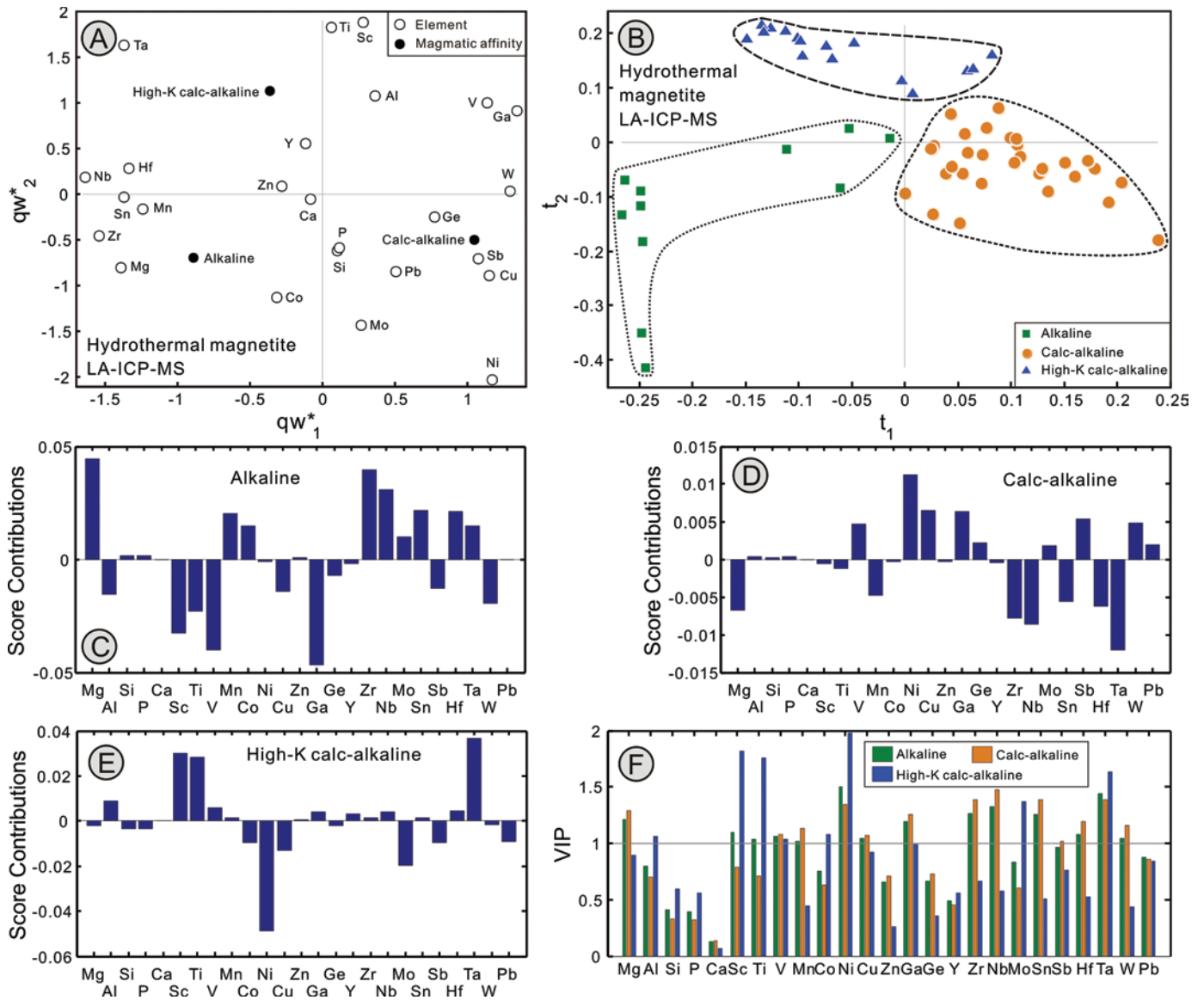


Fig. 13. PLS-DA of LA-ICP-MS data of hydrothermal magnetite grouped by magmatic affinity of porphyry intrusions. A. The qw^*_1 - qw^*_2 (first and second loadings) plot showing correlations among element variables and magmatic affinity. B. The t_1 - t_2 (first and second scores) plot showing the distribution of individual analyses of samples in the latent variable space defined by qw^*_1 - qw^*_2 in A. C-E. Score contribution plots of elements for hydrothermal magnetite associated with different magmatic affinities. F. The VIP plot showing the importance of compositional variables in classification of samples in B. Gray line in F represents the VIP value of 1. Elements with VIP value higher than 1 are the most important in the classification.

below detection limit and rarely reported (Dare et al., 2014). The slightly higher P in igneous magnetite compared to hydrothermal magnetite may be related to highly differentiated granitic magma rich in P. Igneous magnetite is generally rich in high field strength elements (HFSEs)—Zr, Hf, Nb, and Ta—relative to hydrothermal magnetite. This observation is consistent with the result of Dare et al. (2014). Because HFSEs are relatively incompatible in magnetite ($D_{Zr} = 0.2$, $D_{Hf} = 0.25$, $D_{Nb} = 0.1$, $D_{Ta} = 0.2$; Dare et al., 2012), these metals are preferentially incorporated into late igneous magnetite crystallized from the most evolved magmas. Moreover, the HFSEs are considered relatively immobile during alteration at low metamorphic grades and low water/rock ratios (Pearce

and Cann, 1973; Floyd and Winchester, 1978; Middelburg et al., 1988) and thus have low solubility in hydrothermal fluids under the pressure-temperature conditions that prevail during the formation of porphyry deposits. Thus, the low mobility of HFSEs under hydrothermal conditions perhaps explains their low concentrations in most magmatic-hydrothermal fluids.

Silicon and Ca are extremely incompatible in igneous magnetite crystallized from silicate melts ($D_{Si} = 0.0017$, $D_{Ca} = 0.035$; Dare et al., 2012). Although no partition coefficients of Si and Ca between magnetite and hydrothermal fluids are available, Si- and/or Ca-rich (e.g., ~1–6 wt %) hydrothermal magnetite is commonly found in skarn deposits (Westendorp

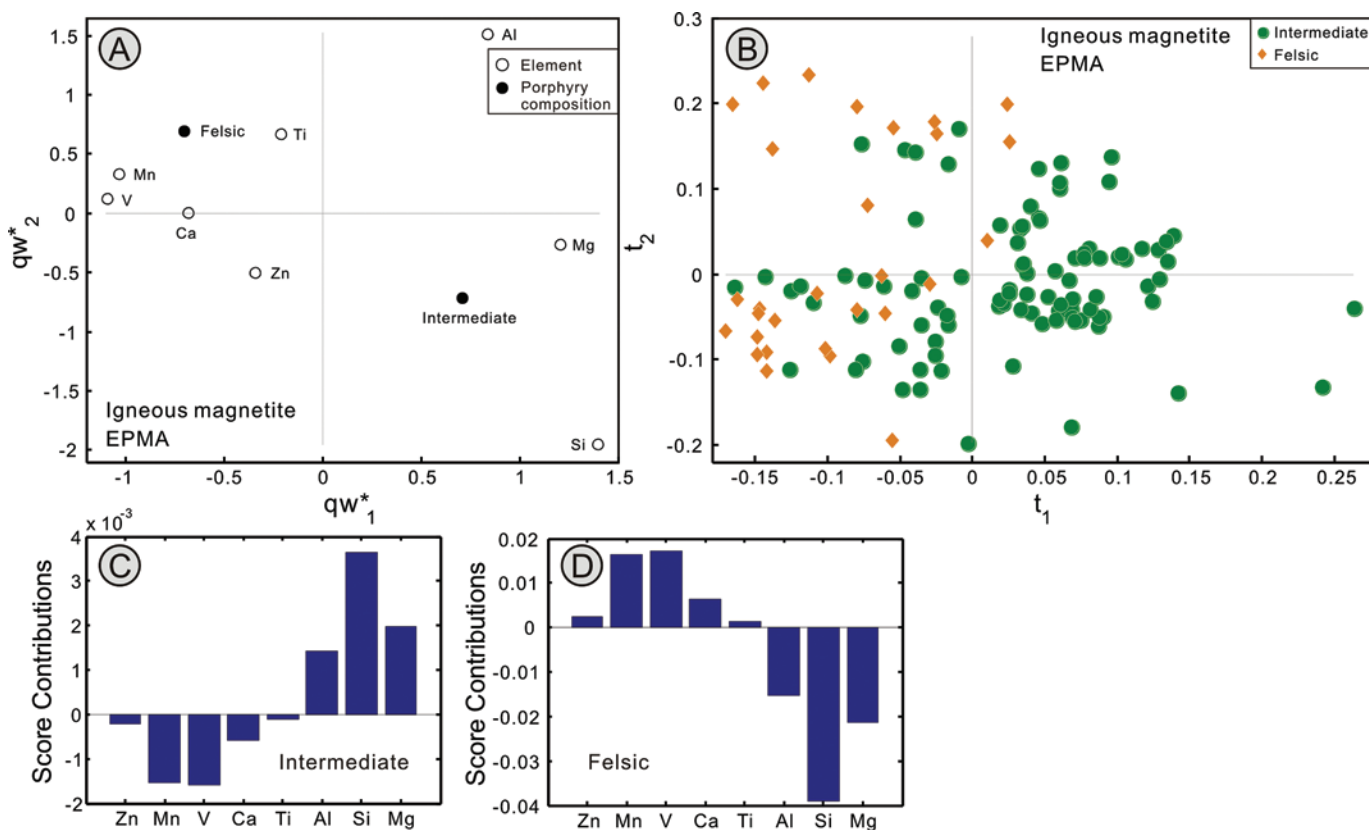


Fig. 14. PLS-DA of EPMA data of igneous magnetite hosted by intermediate and felsic porphyry. A. The qw^*_1 - qw^*_2 (first and second loadings) plot showing correlations among element variables and porphyry composition. B. The t_1 - t_2 (first and second scores) plot showing the distribution of individual analyses of samples in the latent variable space defined by qw^*_1 - qw^*_2 in A. C, D. Score contribution plots of elements for igneous magnetite hosted by intermediate and felsic porphyry.

et al., 1991; Shimazaki, 1998; Ciobanu and Cook, 2004; Dupuis and Beaudoin, 2011; Hu et al., 2015; Huang et al., 2018). This suggests that Si and Ca are highly mobile during hydrothermal alteration and tend to concentrate in magnetite precipitated from hydrothermal fluids. However, some magnetite grains with high Si and Ca contents in fact contain nanometer-scale mineral inclusions (Deditius et al., 2018).

Hydrothermal magnetite from porphyry deposits is rich in Ge, Sb, Pb, and W relative to igneous magnetite. These elements are incompatible to weakly compatible in magmatic magnetite ($D_{Ge} = 0.11$, $D_{Sb} = 0.35$, $D_{Pb} = 1.4$, $D_W = 2.3$). Meng et al. (2017) interpreted the enrichment of Ge in hydrothermal magnetite from skarn, IOCG, and volcanic-hosted hydrothermal deposits, relative to igneous magnetite from magmatic Fe-Ti oxide and Ni-Cu sulfide deposits, as caused by higher oxygen fugacity. The elevated W, Pb, As, Mo, and Sn concentrations in altered magnetite from banded iron formation-hosted high-grade iron deposits were attributed to hydrothermal metasomatism related to the granitic rocks (Nadoll et al., 2014). Germanium, Sb, and Pb are also chalcophile and more likely to partition into coexisting sulfides such as chalcopyrite and pyrite (Bernstein, 1985; Dare et al., 2012; Meng and Hu, 2018). Minor amounts of these elements in hydrothermal magnetite coprecipitating with Fe-Cu sulfides may reflect relative enrichment of these elements in fluids. Considering that these elements have high solubility

in hydrothermal fluids—in particular at intermediate to high temperatures ($>300^\circ\text{C}$) (Hemley and Hunt, 1992)—it is likely that hydrothermal fluids that exsolved from porphyry-associated intrusions may have a major control on the contents of Ge, Sb, Pb, and W in hydrothermal magnetite from porphyry deposits.

Transition metals Co and Ni are strongly compatible in magnetite crystallized from silicate melt ($D_{Co} = 7.5$, $D_{Ni} = 30$; Dare et al., 2012) and are expected to be in high concentration in igneous magnetite. In contrast to sulfide-deficient mineral assemblage of igneous magnetite, hydrothermal magnetite in porphyry deposits is commonly crystallized with chalcopyrite and pyrite that scavenge or preferentially incorporate chalcophile elements such as Co and Ni from fluids (Dare et al., 2012). It is thus expected that hydrothermal magnetite in sulfide-bearing veins should be depleted in Co and Ni relative to igneous magnetite. However, Co and Ni contents are relatively higher in hydrothermal magnetite compared to igneous magnetite (Figs. 5B, 7). Nadoll et al. (2015) showed that there are no obvious differences in Co contents (~ 40 ppm) between igneous and hydrothermal magnetite from porphyry deposits. Considering that porphyry systems are hosted by a variety of igneous, sedimentary, and metamorphic rocks (Table 1), the relative enrichment of Co and Ni in hydrothermal magnetite is most likely due to interaction of hydrothermal fluids with mafic volcanic rocks or magmatic sulfides. This is consistent

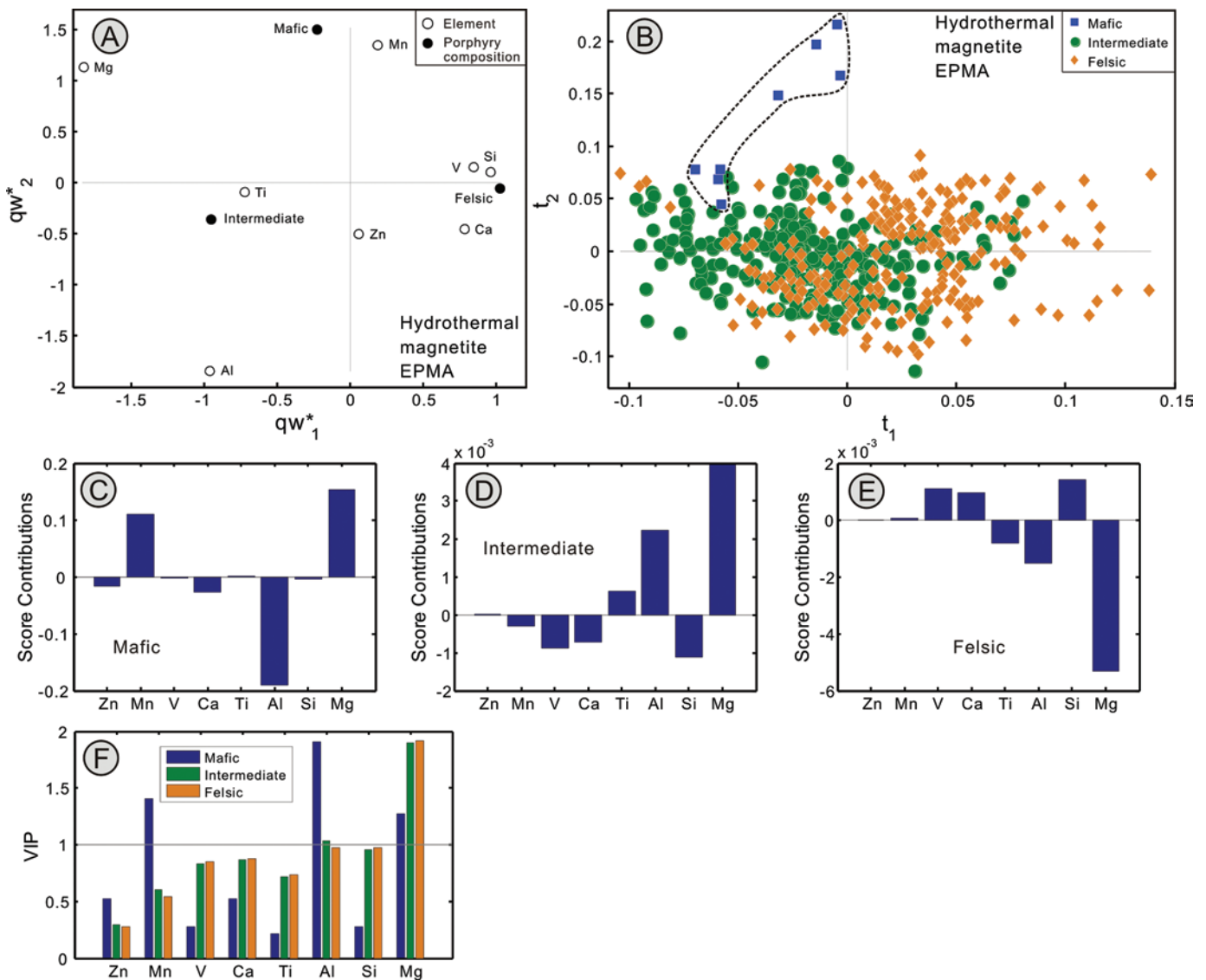


Fig. 15. PLS-DA of EPMA data of hydrothermal magnetite grouped by host porphyry composition. A. The qw^*_1 - qw^*_2 (first and second loadings) plot showing correlations among element variables and porphyry composition. B. The t_1 - t_2 (first and second scores) plot showing the distribution of individual analyses of samples in the latent variable space defined by qw^*_1 - qw^*_2 in A. C-E. Score contribution plots of elements for hydrothermal magnetite associated with different types of porphyries. F. The VIP plot showing the importance of compositional variables in classification of samples in B. Gray line in F represents the VIP value of 1.

with hydrothermal magnetite from mafic porphyry that has higher Co content than that from intermediate and felsic porphyries (Fig. 16C).

Hydrothermal magnetite is relatively rich in Mg but depleted in Mn compared to igneous magnetite. The low score contributions for Mn (Fig. 7E-H) indicate subtle differences in Mn contents between igneous and hydrothermal magnetite and indicate that Mn is not as important as Mg in discriminating magmatic from hydrothermal magnetite. Hydrothermal fluids can be enriched in elements such as Mg and Mn by extensive fluid-rock interactions (Einaudi et al., 1981; Meinert et al., 2005), as suggested by relatively high Mg and Mn contents in skarn magnetite (Nadoll et al., 2015; Zhao and Zhou, 2015; Huang et al., 2016, 2018). Considering that

mafic porphyry is involved in the formation of hydrothermal magnetite, the higher Mg in hydrothermal magnetite is thus explained by host-rock buffering, because hydrothermal magnetite related to mafic porphyry is rich in Mg and Mn relative to that related to intermediate and felsic porphyries (Figs. 15, 16).

Discrimination diagrams for igneous and hydrothermal magnetite

Partial least squares-discriminant analysis of EPMA data shows that igneous magnetite cannot be discriminated from hydrothermal magnetite in the t_1 - t_2 space (Fig. 7B). In spite of overlapping, positive contributions of Si and Ca discriminate hydrothermal magnetite, whereas positive contributions of Ti

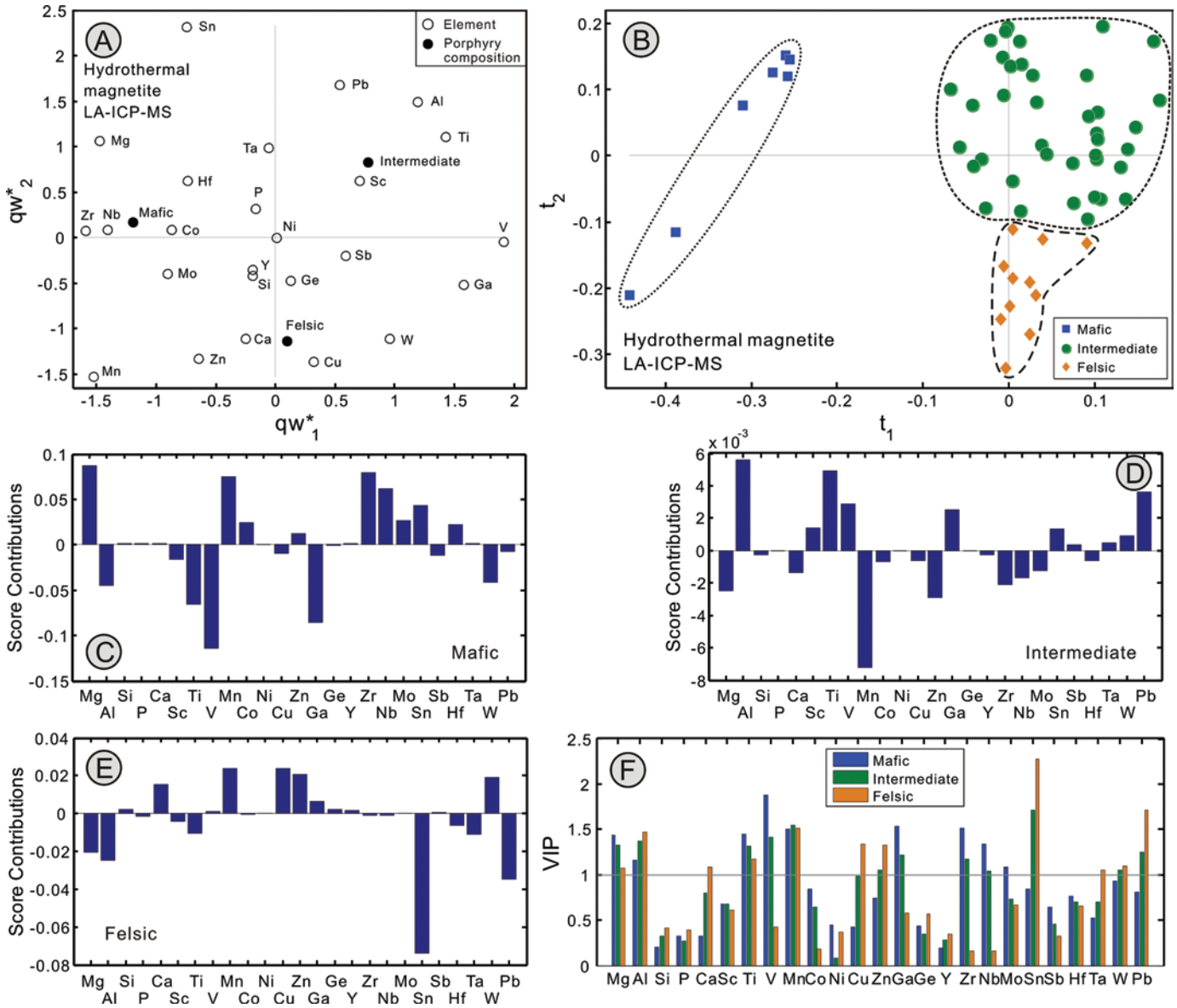


Fig. 16. PLS-DA of LA-ICP-MS data of hydrothermal magnetite grouped by host porphyry composition. A. The qw^*_1 - qw^*_2 (first and second loadings) plot showing correlations among element variables and porphyry composition. B. The t_1 - t_2 (first and second scores) plot showing the distribution of individual analyses of samples in the latent variable space defined by qw^*_1 - qw^*_2 in A. C-E. Score contribution plots of elements for hydrothermal magnetite associated with different types of porphyries. F. The VIP plot showing the importance of compositional variables in classification of samples in B. Gray line in F represents the VIP value of 1.

and V characterize igneous magnetite (Fig. 7E-F). PLS-DA of LA-ICP-MS data, covering a larger number of elements, show a clear separation between igneous and hydrothermal magnetite (Fig. 7D). The most important discrimination elements for igneous magnetite are V and Zr, whereas those for hydrothermal magnetite are Mg, Si, Ge, and Sb (Fig. 7G, H). The different discrimination ability of magnetite between EPMA and LA-ICP-MS data is related to the larger number of variables (i.e., elements) but perhaps also to the smaller number of samples analyzed by LA-ICP-MS. Therefore, the boundary between igneous and hydrothermal magnetite is preliminary (Fig. 7D) and should be confirmed by more data.

Dare et al. (2014) proposed a Ti versus Ni/Cr discriminant diagram to distinguish magnetite from igneous to hydrothermal origin. This diagram is constructed based on the different behavior of Ni and Cr in magmatic and hydrothermal systems. Nickel and Cr are coupled in silicate magmas with Ni/Cr ratios lower than 1, because they behave compatibly during fractionation of intermediate and felsic melts, whereas they are decoupled in many hydrothermal systems with higher Ni/Cr ratios, likely due to a higher solubility of Ni compared to Cr in fluids (Dare et al., 2014). EPMA data show that most of hydrothermal magnetite grains plot in the hydrothermal field (Fig. 17A). However, some hydrothermal magnetite has lower Ni/Cr ratios than expected (Fig. 17A). Moreover, more than

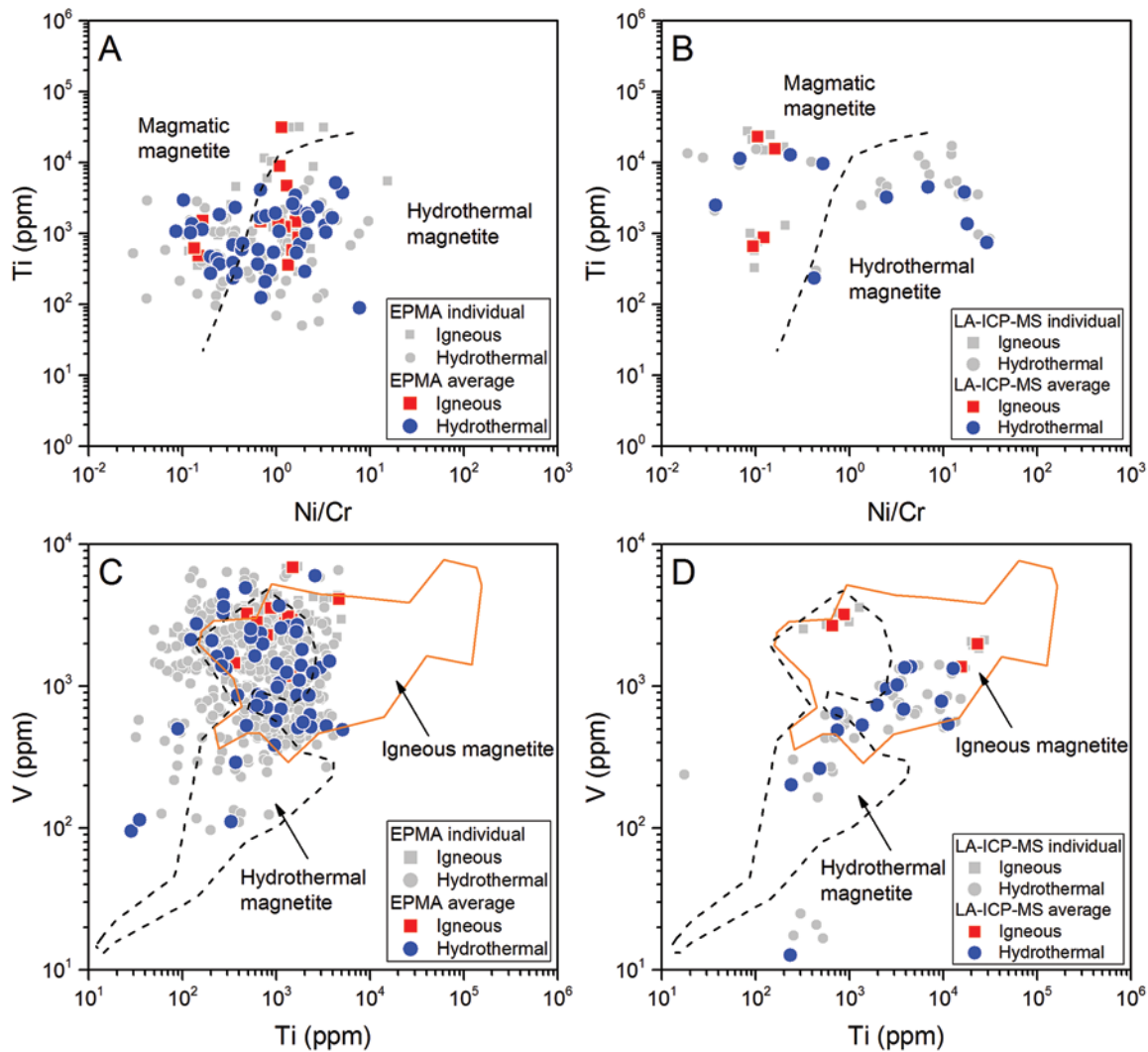


Fig. 17. Plots of Ni/Cr versus Ti (A, B) and V versus Ti (C, D) showing the composition differences between igneous and hydrothermal magnetite from porphyry deposits. The boundary line (dotted line) between igneous and hydrothermal magnetite in A is defined by Dare et al. (2014), whereas the fields in B for igneous and hydrothermal magnetite are defined by the data of Nadoll et al. (2015).

half of igneous magnetite plots in the hydrothermal field characterized by high Ni/Cr ratios. LA-ICP-MS data show that all igneous magnetite plots in the magmatic field but that some hydrothermal magnetite plots in both magmatic and hydrothermal fields (Fig. 17B). Our results are consistent with the observation of Knipping et al. (2015) that the Ti versus Ni/Cr diagram is not very useful for discrimination between igneous and hydrothermal magnetite. Experimental studies showed that both Cr^{6+} and Cr^{3+} are more soluble than Ni in aqueous fluid at high temperature (magmatic conditions) (James, 2003; Watenphul et al., 2012, 2013), which would result in low Ni/Cr ratios for magmatic-hydrothermal magnetite. Low Cr contents and high Ni/Cr ratios, however, cannot be used as diagnostic features for hydrothermal magnetite, because Ni is compatible in magmatic magnetite in absence of coprecipitating Fe sulfides (Dare et al., 2012; Knipping et al., 2015).

Nadoll et al. (2015) proposed a simple binary Ti-V diagram to discriminate between igneous and hydrothermal magnetite

from porphyry and skarn deposits. They considered that igneous magnetite commonly has Ti contents above $\sim 5,000$ ppm, whereas hydrothermal magnetite is characterized by lower Ti-V concentrations, in spite of an overlap between igneous and hydrothermal magnetite. In the Ti-V plot, most EPMA data of igneous and hydrothermal magnetite from porphyry deposits plot in the overlapping field (Fig. 17C), whereas most hydrothermal magnetite LA-ICP-MS data plot in the igneous field (Fig. 17D). This suggests that in porphyry systems, the limit between igneous and hydrothermal processes is transitional and that some of the magnetite grains have a hydrothermal-igneous origin. This overlapping composition between igneous and hydrothermal magnetite is also observed in PLS-DA results (Fig. 7B). Moreover, microtextures show that some igneous magnetite grains have been replaced along grain margins and that some ilmenite lamellae have been altered to titanite (Fig. 1E, F). Wen et al. (2017) showed that igneous magnetite grains in altered granitic rocks have modified

texture and chemical composition. This secondary magnetite, formed by replacement of igneous magnetite, has different trace element compositions from the primary igneous magnetite. This partly explains why the binary plots of Ti versus Ni/Cr and Ti versus V cannot efficiently discriminate igneous and hydrothermal magnetite in porphyry deposits.

Relationship between deposit subtypes and magnetite chemistry

As shown in Figures 8 and 9, both igneous and hydrothermal magnetite from Cu-Au, Cu-Mo, and Cu-Mo-Au deposits cannot be discriminated by EPMA data. However, hydrothermal magnetite from these deposits can be discriminated by LA-ICP-MS data in spite of minor overlap (Fig. 10B). In addition, PLS-DA of EPMA and LA-ICP-MS data of hydrothermal magnetite shows that porphyry W-Mo and Au-Cu deposits can be discriminated from other deposit subtypes (Figs. 9, 10). The discrimination between different subtypes of porphyry deposits suggests that the composition of hydrothermal magnetite can reflect physical or chemical conditions responsible for the formation of these deposit types.

The porphyry intrusions have compositions spanning from mafic to felsic (Table 1). Sinclair (2007) and Sillitoe (2010) suggested that the composition of porphyry intrusions has important effects on mineralization types and ore grades of porphyry deposits. For example, felsic intrusions are commonly associated with Mo-rich porphyry Cu deposits (e.g., Butte and Escondida Norte; Table 1), whereas intrusions with more mafic compositions are associated with Au-rich porphyry deposits (Sillitoe, 2010). Some Au-rich porphyry deposits, however, such as Ridgeway, are hosted by monzodiorite to quartz monzonite intrusions of intermediate composition (Table 1; Sillitoe, 2010). Porphyry Mo (Climax-type), W-Mo, W, and Sn deposits are commonly in association with highly evolved granitic intrusions with SiO₂ contents ranging from 72 to 77 wt % (Sinclair, 2007). The relatively high Si and Al contents in hydrothermal magnetite from the Mount Pleasant porphyry W-Mo deposit (Fig. 9J) are thus likely due to the granitic composition of the host intrusions (Table 1). This is consistent with the fact that hydrothermal magnetite related to felsic porphyry has higher Si contents than that related to mafic and intermediate porphyries (Figs. 15E, 16E). Intrusions associated with Endako-type porphyry Mo deposits range more widely in composition, from granodiorite to granite (Table 1; Sinclair, 2007), whereas porphyry Cu-Au, Cu-Mo, and Cu-Mo-Au deposits are hosted by intermediate intrusions (Table 1). Therefore, the overlapping composition of hydrothermal magnetite from porphyry Mo (Endako), Cu-Au, Cu-Mo, and Cu-Mo-Au deposits (Figs. 9B, D, 10B) could be explained by similar and overlapping composition of their host intrusions. This is consistent with the significant compositional overlapping of hydrothermal magnetite associated with intermediate and felsic porphyry intrusions (Fig. 15B).

The Porgera porphyry Au-Cu deposit is hosted by mafic intrusions, whereas the Sari Gunay and Ridgeway porphyry Au-Cu deposits are hosted by intermediate intrusions (Table 1). The more mafic composition of the host rocks may explain the high Mg and Mn in hydrothermal magnetite from Au-Cu deposits, because these elements are more enriched in fluids

related to mafic magma than those related to felsic magma (Figs. 15C, 16C). However, the relative enrichment of HFSEs such as Zr, Nb, and Hf in Au-Cu deposit hydrothermal magnetite cannot be explained by a more mafic host-rock composition, because these elements are incompatible in magnetite (Dare et al., 2012) and tend to concentrate in more evolved magma and related fluids. Alternatively, other factors such as fluid chemistry also play an important role. In the fluoride-rich alkaline magmatic systems, Zr, Nb, and rare earth elements in igneous rocks can be remobilized and transported during later hydrothermal alteration to form related metal deposits (Salvi and Williams-Jones, 2006; Yang et al., 2014). Experimental studies also demonstrated that NaCl- and NaF-bearing aqueous fluids at high-pressure (>0.5 GPa) and moderate- to high-temperature (>300°C) conditions could improve HFSE solubility (Tanis et al., 2015, 2016). Webster and Holloway (1990) and Shchekina and Gramenitskii (2008) have shown that Mo, Sn, Nb, and Sc strongly partition into F-rich fluids, consistent with the fact that porphyry Mo and Sn deposits are closely related to fluids exsolved from highly differentiated, F-rich granitic magmas. Therefore, the relative enrichment of HFSEs and Sn in hydrothermal magnetite from Au-Cu deposits and Sc in hydrothermal magnetite from porphyry Cu-Au deposits appears to be dominated by fluid chemistry (Cl/F). Because Au is commonly assumed to be in the form of chloride complexes in the hypersaline liquid phase (Henley, 1973; Chou and Eugster, 1977), the high concentration of chloride in fluids is more likely the factor inducing the relative enrichment of HFSEs in Au-rich porphyry hydrothermal magnetite. This is consistent with the generally high contents of halogens, such as Cl and F, of ore-bearing rocks in these deposits (Müller and Groves, 1993).

The oxidation state of granitic rocks, divided into magnetite series and ilmenite series (Ishihara, 1981), also exerts a control on the mineralization types of porphyry deposits (Sinclair, 2007). For example, the relatively oxidized, magnetite-series, granitic rocks commonly host porphyry Cu, Cu-Mo, Cu-Au, Au, Mo (Climax-type), and W deposits, whereas relatively reduced, ilmenite-series intrusions are associated with most porphyry Sn deposits (Sinclair, 2007). Granitic rocks hosting Endako-type Mo deposits have oxidation states spanning both magnetite and ilmenite series (Sinclair, 2007). Because nearly all our studied deposits are associated with magnetite-series plutons, the effect of oxidation state of host rocks on trace element variations in magnetite from different porphyry deposits cannot be discussed. However, the relative oxygen fugacity conditions for different porphyry deposits can be reflected by magnetite chemistry. It is worth noting that hydrothermal magnetite from porphyry Au-Cu deposits is depleted in V relative to that from porphyry Cu-Au, Cu-Mo, and Cu-Mo-Au deposits (Fig. 10C). The fact that gold-rich deposits are usually rich in magnetite suggests that high f_{O_2}/f_{S_2} ratios, conducive to deposition of larger amounts of magnetite under feldspar-stable conditions, also favor the precipitation of larger amounts of gold (Sillitoe, 1979; Sun et al., 2004). The relative depletion of V in porphyry Au-Cu hydrothermal magnetite is consistent with formation under higher f_{O_2} than hydrothermal magnetite from other subtypes of porphyry deposits, because V partitions into magnetite at relatively low f_{O_2} (Toplis and Corgne, 2002; Sievwright et al., 2017; Sossi et al., 2018).

In addition to host-rock composition, fluid chemistry, and f_{O_2} conditions, temperature may exert control on the chemical composition of magnetite from different types of porphyry deposits. Titanium and Al concentrations in magnetite are positively correlated to temperature in igneous systems (Nielsen et al., 1994; Toplis and Carroll, 1995). Both igneous and hydrothermal magnetite from porphyry Cu-Au and Cu-Mo deposits have higher Ti and Al contents than magnetite from other types of deposits, particularly Au-Cu deposits (Figs. 8C, 9F, 10D). This indicates that Cu-dominated porphyry deposits formed at a higher temperature than Au-dominated porphyry deposits. This conclusion is consistent with the evolution of porphyry systems. Sillitoe (2010) suggested that fluid cooling, from $\sim 550^\circ$ to 350°C , along with reaction with country rocks, is a dominant process forming low-sulfidation Cu-Fe sulfides in porphyry Cu deposits. Williams-Jones and Heinrich (2005) and Sillitoe (2010) showed that pressure decrease and vapor expansion during upward flow can cause precipitation of Cu-Fe sulfides and Au. The precipitation of gold by decreasing temperature and pressure thereby potentially accounts for the typically shallow formation (Cox and Singer, 1992; Sillitoe, 2000) of Au-rich porphyry Cu deposits (Williams-Jones and Heinrich, 2005).

Relationship between magmatic affinity and magnetite chemistry

Porphyry deposits can be classified based on the geochemical composition of their associated porphyritic intrusions (Barr et al., 1976). Most of the studied porphyry deposits are associated with calc-alkaline and alkaline intrusions, whereas Bingham Canyon and Oyu Tolgoi Cu-Mo-Au deposits and Bajo de la Alumbrera Cu-Au deposits are hosted by intrusions with high-K calc-alkaline compositions (Table 1). It has been suggested that Au-rich porphyry deposits have an affinity with high-K calc-alkaline rocks (Müller and Groves, 1993, 2000; Sillitoe, 1997, 2000). In this section, we discuss the magmatic affinity with the chemical composition of igneous and hydrothermal magnetite.

Partial least squares-discriminant analysis of EPMA data for both igneous and hydrothermal magnetite shows no distinction based on magmatic affinities of host porphyry (Figs. 11, 12). In spite of overlapping in the t_1 - t_2 plots (Figs. 11B, 12B), positive contributions of Zn, V, and Ca discriminate igneous and hydrothermal magnetite associated with calc-alkaline intrusions, whereas positive contributions of Ti and Al discriminate that associated with high-K calc-alkaline intrusions (Figs. 11D, E, 12D, E). PLS-DA of LA-ICP-MS data of hydrothermal magnetite define fields for porphyries with different magmatic affinity (Fig. 13A, B). Hydrothermal magnetite associated with alkaline intrusions is discriminated by positive contributions of Mg, Mn, Co, Zr, Nb, Mo, Sn, Hf, and Ta, whereas that associated with calc-alkaline intrusions is discriminated by positive contributions of V, Ni, Cu, Ga, Ge, Sb, and W (Fig. 13C, D). Hydrothermal magnetite associated with high-K calc-alkaline intrusions can be separated from that associated with alkaline and calc-alkaline intrusions by positive contributions of Al, Sc, Ti, and Ta (Fig. 13E). This indicates that hydrothermal magnetite chemistry is partly controlled by the magmatic affinity of intrusions.

An alkaline magma is rich in Na and K relative to subalkaline magmas (Le Bas et al., 1986), depleted in Si and/or Al with respect to alkalis, and rich in volatile components (Fitton, 1987). Fitton (1987) and Harris and Sheppard (1987) argued that the enrichment of volatiles in alkaline magma was evidenced by widespread metasomatized rocks such as fenite around alkaline plutons, high contents of Cl and F in some alkaline igneous rocks, and the explosive eruption of alkaline magma. It is worth noting that hydrothermal magnetite associated with alkaline intrusions has the same signature elements as that from the Au-Cu deposits that are mainly hosted by alkaline intrusions. Therefore, the same factors controlling the chemical composition of hydrothermal magnetite from the Au-Cu deposits, such as the high concentrations of Cl and F in magma/fluids, can be applied to hydrothermal magnetite associated with alkaline intrusions. The typically higher Ca content in igneous and hydrothermal magnetite associated with calc-alkaline intrusions may be related to the high concentration of Ca in this magma series (Wilson, 1996). The relative depletion of HFSEs in hydrothermal magnetite associated with calc-alkaline intrusions is also consistent with the depletion of these elements in calc-alkaline magma (Hooper, 1994).

High-K, I-type granitoid magmas are derived from partial melting of hydrous, calc-alkaline to high-K calc-alkaline, mafic to intermediate metamorphic rocks in the crust (Roberts and Clemens, 1993). The relative enrichment of incompatible elements Sc and Ta in igneous and hydrothermal magnetite associated with high-K calc-alkaline intrusions may reflect the composition of this magma type. The coupled behavior of Al and Ti in igneous and hydrothermal magnetite (Figs. 11A, 12A, 13A) is similar to behavior observed in other porphyry deposits (Canil et al., 2016). The partition of both Ti and Al in the magnetite shows a positive temperature dependence (Nielsen et al., 1994; Toplis and Carroll, 1995). The relatively high Al and Ti in igneous and hydrothermal magnetite associated with high-K calc-alkaline intrusions likely reflects higher temperatures for magnetite formation or the relative enrichment of these elements in high-K calc-alkaline melts and their exsolved fluids.

Comparison of porphyry Cu magnetite composition and that of IOCG, IOA, and skarn deposits

Porphyry Cu, IOCG, IOA, and skarn deposits belong to the family of magmatic-hydrothermal deposits (Sillitoe, 2003, 2010; Meinert et al., 2005; Williams et al., 2005; Pollard, 2006; Richards and Mumin, 2013; Simon et al., 2018), although some IOCG deposits are also considered to be related to basinal brines (Barton and Johnson, 2000). These deposits have similar ore mineral assemblages of magnetite, hematite, chalcopyrite, and pyrite but with different proportions. Sillitoe (2003) and Tornos et al. (2010) have proposed that IOCG deposits related to diorite intrusions form a vertical continuum from high-temperature, magnetite-dominant Cu-Au mineralization to shallower, low-temperature, hematite-dominant mineralization. Others consider that contrasting tectonic settings and sulfur contents of magmas control the formation of porphyry Cu \pm Mo \pm Au and intrusion-related IOCG deposits (Richards and Mumin, 2013; Richards et al., 2017). The close relationship between porphyry Cu and skarn

systems is well recognized (Einaudi et al., 1981; Einaudi, 1982), and the carbonate wall rocks around the intrusion-centered porphyry system can host proximal Cu-Au skarns and less common distal Zn-Pb and/or Au skarns (Sillitoe, 2010). In carbonates and carbonate alteration close to intrusions in IOCG systems, skarns may develop with Fe-Cu-Au sulfide mineralization (Corriveau et al., 2010, 2016). Dupuis and Beaudoin (2011) proposed plots of Ca + Al + Mn versus Ti + V and Ni/(Cr + Mn) versus Ti + V, based on EPMA data, to distinguish magnetite in porphyry deposits from other magmatic-hydrothermal deposits. Nadoll et al. (2014, 2015), however, considered that the boundary between porphyry Cu and skarn deposits in Al + Mn versus Ti + V plots is transitional. Canil et al. (2016) showed that the PCA method is efficient to distinguish highest-temperature igneous magnetite,

intermediate-temperature hydrothermal porphyry magnetite, and low-temperature skarn magnetite due to different Ti, Al, and V contents. Here, we compare the trace element composition of hydrothermal magnetite from porphyry Cu, IOCG, IOA, and skarn deposits, using PLS-DA of a large EPMA ($n = 1,675$) and LA-ICP-MS ($n = 1,335$) data set, to identify the most discriminant elements for each deposit type. This will be useful to identify magnetite with unknown origins.

Partial least squares-discriminant analysis of EPMA data (Si, Ca, Al, Mn, Mg, Ti, and V) shows that magnetites from porphyry Cu, IOCG, IOA, and skarn deposits cannot be discriminated from each other (Fig. 18A, B). However, magnetite from different types of deposits shows characteristic elemental compositions. Magnetite from porphyry Cu deposits is characterized by positive contributions of Ti, Al, and V

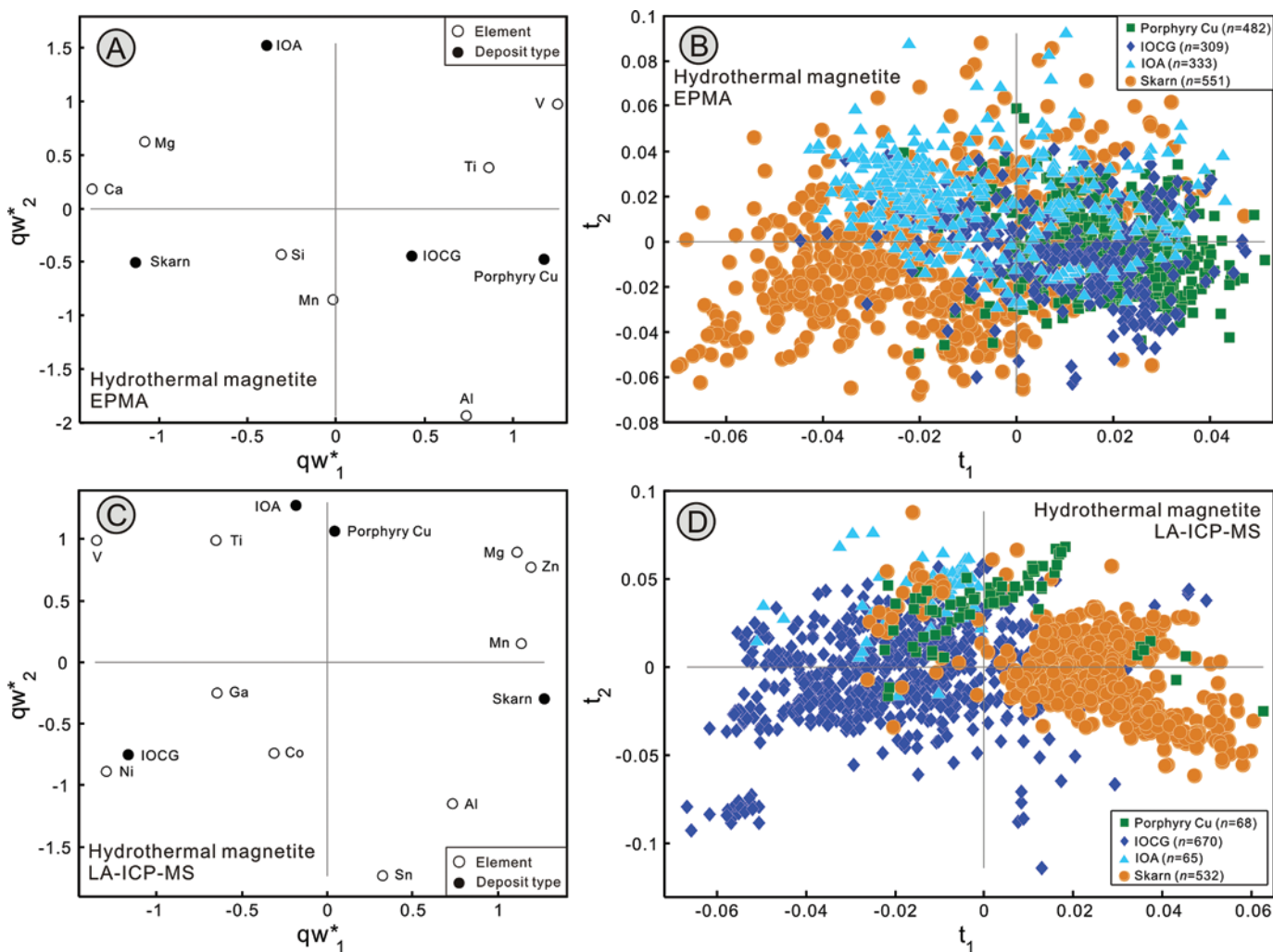


Fig. 18. PLS-DA of EPMA (A, B, E-H, M) and LA-ICP-MS (C, D, I-L, N) data of hydrothermal magnetite from porphyry Cu, IOCG, IOA, and skarn deposits. EPMA data sources: porphyry Cu (this study; Dupuis and Beaudoin, 2011), IOCG (Dupuis and Beaudoin, 2011; Huang et al., 2019), IOA (Knipping et al., 2015; Huang et al., 2019), and skarn deposits (Schwartz and Melcher, 2004; Dupuis and Beaudoin, 2011; Nadoll, 2011; Li, 2012; Dare et al., 2014; Duan et al., 2014; Hu et al., 2014, 2017; Xie et al., 2017). LA-ICP-MS data sources: porphyry Cu (this study), IOCG (Carew, 2004; Gosselin et al., 2006; Dupuis and Beaudoin, 2007; Chen et al., 2015a, b; Zhao et al., 2018; Huang et al., 2019), IOA (Knipping et al., 2015; Huang et al., 2019), and skarn (Huang et al., 2013, 2016, 2018; Yi et al., 2015; Zhao and Zhou, 2015; Canil et al., 2016; Hu et al., 2017; Xie et al., 2017) deposits. A, C. The qw_1 - qw_2 (first and second loadings) plot showing correlations among element variables and deposit types. B, D. The t_1 - t_2 (first and second scores) plots showing the distribution of individual analyses of samples in the latent variable space defined by qw_1 - qw_2 in A and C, respectively.

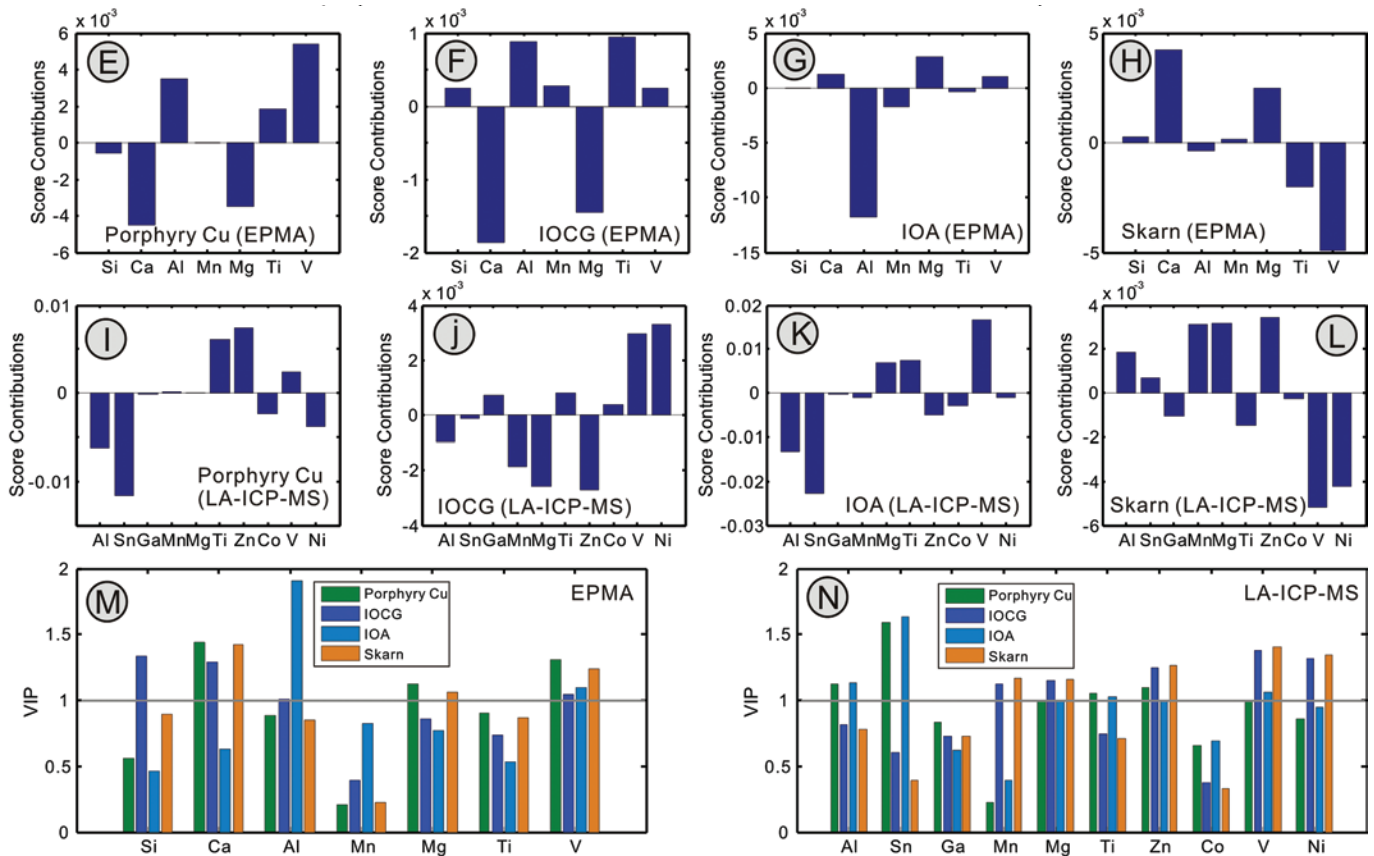


Fig. 18. (Cont.) E-H. Score contribution plots of elements based on EPMA data for hydrothermal magnetite from different types of deposits. I-L. Score contribution plots of elements based on LA-ICP-MS data for hydrothermal magnetite from different types of deposits. M, N. The VIP plots showing the importance of compositional variables in classification of samples in B and D, respectively.

(Fig. 18E), whereas that from IOCG deposits is discriminated by positive contributions of Al and Ti (Fig. 18F). Weakly positive contributions of Mg, Ca, and V and negative contribution of Al characterize magnetite from IOA deposits (Fig. 18G), whereas positive contributions of Ca and Mg discriminate magnetite from skarn deposits (Fig. 18H). EPMA data VIP plot shows that Ti is the most important discriminant element for these four types of deposits (Fig. 18M). Calcium is useful for discriminating all deposit types except IOA deposits, whereas Mg is useful for discriminating between porphyry Cu and skarn deposits (Fig. 18M). Silicon is an important discriminant element for IOCG deposits, whereas Al is useful in discrimination between IOCG and IOA magnetite (Fig. 18M). PLS-DA of LA-ICP-MS data, using Al, Mn, Mg, Ti, V, Ga, Co, Zn, Ni, and Sn, yields a better discrimination than that of EPMA data. Magnetite from IOCG deposits can be separated from skarn deposits by t_1 , but magnetite from IOA and porphyry deposits overlaps that from IOCG deposits (Fig. 18C, D). Score contributions indicate that magnetite from porphyry deposits has relatively high Ti and Zn (Fig. 18I), whereas that from IOCG deposits has relatively high V and Ni (Fig. 18J). Magnetite from IOA deposits is characterized by higher V, Ti, and Mg (Fig. 18K), whereas magnetite from skarn deposits is characterized by higher Mn, Mg, and Zn (Fig. 18L). LA-ICP-MS data VIP plot shows that Mg, Zn,

and V are most important discriminant elements for the four types of deposits, whereas Mn and Ni are important in discriminating magnetite from IOCG deposits and skarn deposits (Fig. 18N). Tin, Al, and Ti are useful for discriminating magnetite from IOA and porphyry Cu deposits (Fig. 18N). In summary, Ti, V, Zn, and Al, in the order of decreasing importance, are higher in magnetite from porphyry Cu deposits, V, Ni, Ti, and Al are higher for IOCG deposits, V, Ti, and Mg are higher for IOA deposits, and Mg, Mn, Ca, and Zn are higher for skarn deposits. This conclusion is consistent with the study of Nadoll et al. (2015), in which the key elements accounting for compositional variations are Mg and Mn for hydrothermal magnetite from skarn and Mg, Ti, V, Mn, Co, and Zn for hydrothermal porphyry magnetite.

The decreased Ti + V contents in magnetite from porphyry Cu, IOA, IOCG, to skarn deposits is consistent with the studies of Dupuis and Beaudoin (2011) and Canil et al. (2016) and likely reflect decreasing temperature and increasing oxygen fugacity (Nadoll et al., 2014). The porphyry Cu system cools from $>700^\circ$ to $<250^\circ\text{C}$ with the main Cu precipitation at 550° to 350°C (Sillitoe, 2010). IOA deposits commonly formed by high-temperature ($\sim 800^\circ\text{--}600^\circ\text{C}$) magmatic or magmatic-hydrothermal processes, as indicated by Fe-O stable isotope pairs of magnetite and actinolite (Bilenker et al., 2016; Corriveau et al., 2016), whereas IOCG deposits have

temperatures from $>600^{\circ}$ to $\sim 200^{\circ}\text{C}$ with Cu-Au precipitation between 500° and 200°C (Williams et al., 2005; Corriveau et al., 2016). Skarn deposits can evolve from high-temperature ($\geq 500^{\circ}\text{C}$) high-salinity fluids of magmatic origin in the prograde alteration stage to lower-temperature ($\leq 400^{\circ}\text{C}$) fluids during retrograde magnetite-sulfide stage with influx of cooler, lower-salinity fluids of magmatic origin (Meinert et al., 2005). Most porphyry Cu deposits formed at the f_{O_2} of 3 log units above the fayalite-magnetite-quartz buffer ($\Delta\text{FMQ} +3$) (Richards, 2014), whereas IOCG and skarn deposits probably formed at $\Delta\text{FMQ} +5$, considering the amounts of hematite in the mineral assemblage (Meinert et al., 2005; Williams et al., 2005). Experimental studies have shown that IOA deposits can form from immiscible hydrous Fe-Ca-P melt under more reduced conditions at ΔFMQ between $+0.5$ and $+3.3$ (Hou et al., 2018). The relative depletion of Al in IOA magnetite is due to its low magnetite-silicate melt partition coefficient ($D_{\text{Al}} = 0.2$; Dare et al., 2012) and relative immobility of Al in fluids (Middelburg et al., 1988). With the evolution of melt or fluids, later magnetite will be enriched in Al. Considering that the formation of IOA deposits is earlier and at higher temperature than formation of IOCG and skarn deposits in a magmatic-hydrothermal system (Corriveau et al., 2016), magnetite from IOA deposits is thus relatively depleted in Al. The higher Ni in IOCG magnetite, compared to porphyry and skarn magnetite, is probably due to the more mafic magma for IOCG deposits compared to granodioritic magmas associated with porphyry and skarn deposits (Richards et al., 2017). The more abundant sulfides in porphyry deposit mineral assemblages, compared to IOCG deposits, will likely result in low-Ni porphyry systems because of Ni partitioning into sulfides (Dare et al., 2012; Huang et al., 2014). The higher Ca, Mn, Mg, and Zn in skarn magnetite is consistent with previous studies of magnetite from skarn deposits (Hu et al., 2014; Nadoll et al., 2015; Huang et al., 2016, 2018). Experimental studies suggest that even minor to trace concentrations of base metals, such as Mn and Zn, in magnetite indicate strong enrichment of Mn and Zn relative to Fe in chloride-rich hydrothermal fluids, particularly in skarn system (Ilton and Eugster, 1989). Therefore, the elevated Ca, Mn, Mg, and Zn in skarn magnetite likely reflect high concentrations of these elements in hydrothermal fluids, possibly via fluid-rock (carbonate) interaction (Einaudi et al., 1981; Meinert et al., 2005).

Conclusions

Trace element compositions of igneous and hydrothermal magnetite from porphyry deposits are used to discuss the main factors controlling the magnetite chemistry. PLS-DA of magnetite composition is used to discriminate between igneous and hydrothermal magnetite, between porphyry deposit subtypes, and between magmatic intrusion affinities. Igneous magnetite can be discriminated from hydrothermal magnetite by higher P, Ti, V, Mn, Zr, Nb, Hf, and Ta but lower Mg, Si, Co, Ni, Ge, Sb, W, and Pb. Compositional variations between igneous and hydrothermal magnetite in porphyry system are controlled by temperature, oxygen fugacity, coprecipitated sulfides, and element solubility/mobility that affects the partition coefficients. Hydrothermal magnetite from porphyry W-Mo and Au-Cu deposits can be discriminated from that from Cu-Mo, Cu-Au, and Cu-Mo-Au deposits due to different

compositional characteristics. Compositional variation in magnetite from different deposit subtypes results from variations in host-rock composition, chlorine in fluids, temperature, and oxygen fugacity. Magmatic affinity of porphyritic intrusions may have some control on the chemical composition of igneous and hydrothermal magnetite mainly by influencing the magma composition and formation temperatures. However, the reason for the relationship between magmatic affinity and magnetite composition needs further study. PLS-DA of compiled porphyry Cu, IOCG, IOA, and skarn magnetite compositions identifies discriminant elements Ti, V, Zn, and Al for porphyry Cu magnetite, V, Ni, Ti, and Al for IOCG magnetite, V, Ti, and Mg for IOA magnetite, and Mn, Mg, Ca, and Zn for skarn magnetite. These compositional differences are mainly due to higher temperature and lower oxygen fugacity for IOA and porphyry deposits, more mafic magma composition and less sulfide competition for IOCG deposits, and more intensive fluid-rock (carbonate) interaction in skarn deposits.

Acknowledgments

This project was funded by China Scholarship Council (CSC, 201604910462) and by the Natural Science and Engineering Research Council (NSERC) of Canada, through a Collaborative Research and Development Grant with Vale, Teck, Areva (now Orano) and the Geological Survey of Canada and the NSERC-Agnico Eagle Industrial Research Chair in Mineral Exploration. We thank Marc Choquette (Université Laval) for his assistance with EPMA, André Ferland, Émilie Bédard, and Marjorie Lapointe (Université Laval) for their assistance with SEM analyses, and Dany Savard (UQAC) for his assistance with LA-ICP-MS analyses. Special thanks are also extended to Brian Rusk (Western Washington University), Christoph A. Heinrich (ETH-Zurich), Jeremy P. Richards (University of Alberta), Meghan Jackson, Paul Jago, and Janina Micko (University of British Columbia), Aldo Bendezu and Kalin Kouzmanov (Université de Genève), Doug Kirwin (formerly Ivanhoe Mines), and Tim Fletcher (Barrick Gold UK Limited), who provided representative samples. We thank Jaayke L. Knipping for sharing the original table for IOA magnetite data of Los Colorados. We also acknowledge constructive comments from Patrick Nadoll and an anonymous reviewer and editorial handling by Adam Simon and Larry Meinert.

REFERENCES

- Aitchison, J., 1986, *The statistical analysis of compositional data*: London, United Kingdom, Chapman and Hall Ltd., 416 p.
- Barr, D.A., Fox, P.E., Northcote, K.E., and Preto, V.A., 1976, The alkaline suite porphyry deposits: A summary: Canadian Institute of Mining and Metallurgy, Special Volume 15, p. 359–367.
- Barton, M.D., and Johnson, D.A., 2000, Alternative brine sources for Fe-oxide (-Cu-Au) systems: Implications for hydrothermal alteration and metals, in Porter, T.M., ed., *Hydrothermal iron oxide copper-gold and related deposits: A global perspective*, v. 1: Adelaide, Australian Mineral Foundation, p. 43–60.
- Bernstein, L.R., 1985, Germanium geochemistry and mineralogy: *Geochimica et Cosmochimica Acta*, v. 49, p. 2409–2422.
- Bilenker, L.D., Simon, A.C., Reich, M., Lundstrom, C.C., Gajos, N., Bindeman, I., Barra, F., and Munizaga, R., 2016, Fe-O stable isotope pairs elucidate a high-temperature origin of Chilean iron oxide-apatite deposits: *Geochimica et Cosmochimica Acta*, v. 177, p. 94–104.
- Borcos, M., Vlad, S., Udubasa, G., and Gabudeanu, B., 1998, Qualitative and quantitative metallogenetic analysis of the ore genetic units in Romania: *Romanian Journal of Mineral Deposits*, v. 78, p. 1–83.

- Boutroy, E., Dare, S.A.S., Beaudoin, G., Barnes, S.-J., and Lightfoot, P.C., 2014, Magnetite composition in Ni-Cu-PGE deposits worldwide and its application to mineral exploration: *Journal of Geochemical Exploration*, v. 145, p. 64–81.
- Brereton, R.G., and Lloyd, G.R., 2014, Partial least squares discriminant analysis: Taking the magic away: *Journal of Chemometrics*, v. 28, p. 213–225.
- Buddington, A., and Lindsley, D., 1964, Iron-titanium oxide minerals and synthetic equivalents: *Journal of Petrology*, v. 5, p. 310–357.
- Canil, D., Grondahl, C., Lacourse, T., and Pisiak, L.K., 2016, Trace elements in magnetite from porphyry Cu-Mo-Au deposits in British Columbia, Canada: *Ore Geology Reviews*, v. 72, p. 1116–1128.
- Carew, M.J., 2004, Controls on Cu-Au mineralisation and Fe oxide metasomatism in the Eastern fold belt, NW Queensland, Australia: Unpublished Ph.D. thesis, Townsville, Australia, James Cook University, p. 213–277.
- Catchpole, H., Kouzmanov, K., Putlitz, B., Seo, J.H., and Fontboté, L., 2015, Zoned base metal mineralization in a porphyry system: Origin and evolution of mineralizing fluids in the Morococha district, Peru: *Economic Geology*, v. 110, p. 39–71.
- Chen, W.T., Zhou, M.-F., Gao, J.-F., and Hu, R.Z., 2015a, Geochemistry of magnetite from Proterozoic Fe-Cu deposits in the Kangdian metallogenic province, SW China: *Mineralium Deposita*, v. 50, p. 795–809.
- Chen, W.T., Zhou, M.-F., Li, X., Gao, J.-F., and Hou, K., 2015b, In-situ LA-ICP-MS trace elemental analyses of magnetite: Cu-(Au, Fe) deposits in the Khetri copper belt in Rajasthan province, NW India: *Ore Geology Reviews*, v. 65, p. 929–939.
- Chou, I.-M., and Eugster, H.P., 1977, Solubility of magnetite in supercritical chloride solutions: *American Journal of Science*, v. 277, p. 1296–1314.
- Ciobanu, C.L., and Cook, N.J., 2004, Skarn textures and a case study: The Ocna de Fier-Dognecea orefield, Banat, Romania: *Ore Geology Reviews*, v. 24, p. 315–370.
- Cooke, D.R., Hollings, P., and Walshe, J.L., 2005, Giant porphyry deposits: Characteristics, distribution, and tectonic controls: *Economic Geology*, v. 100, p. 801–818.
- Corriveau, L., Williams, P.J., and Mumin, A.H., 2010, Alteration vectors to IOCG mineralization: From uncharted terranes to deposits: *Geological Association of Canada, Short Course Notes*, v. 20, p. 89–110.
- Corriveau, L., Montreuil, J.-F., and Potter, E., 2016, Alteration facies linkages among iron oxide copper-gold, iron oxide-apatite, and affiliated deposits in the Great Bear magmatic zone, Northwest Territories, Canada: *Economic Geology*, v. 111, p. 2045–2072.
- Cox, D.P., and Singer, D.A., 1992, Distribution of gold in porphyry copper deposits, U.S. Geological Survey Bulletin 1877, p. C1-C14.
- Crane, D., Kavalieris, I., Hedenquist, J.W., Harris, M., and Camus, F., 2012, Geologic overview of the Oyu Tolgoi porphyry Cu-Au-Mo deposits, Mongolia: *Society of Economic Geologists, Special Publication 16*, p. 187–213.
- Dare, S.A.S., Barnes, S.-J., and Beaudoin, G., 2012, Variation in trace element content of magnetite crystallized from a fractionating sulfide liquid, Sudbury, Canada: Implications for provenance discrimination: *Geochimica et Cosmochimica Acta*, v. 88, p. 27–50.
- Dare, S.A.S., Barnes, S.-J., Beaudoin, G., Méric, J., Boutroy, E., and Potvin-Doucet, C., 2014, Trace elements in magnetite as petrogenetic indicators: *Mineralium Deposita*, v. 49, p. 785–796.
- Deditius, A.P., Reich, M., Simon, A.C., Suvorova, A., Knipping, J., Roberts, M.P., Rubanov, S., Dodd, A., and Saunders, M., 2018, Nanogeochemistry of hydrothermal magnetite: *Contributions to Mineralogy and Petrology*, v. 173, p. 46.
- De Iorio, M., Ebbels, T.M.D., and Stephens, D.A., 2007, Statistical techniques in metabolic profiling, in *Balding, D.J., Bishop, M., and Cunnings, C., eds., Handbook of statistical genetics*, 3rd ed.: New York, Wiley, p. 347–373.
- Dilles, J., Martin, M.W., and Stein, H.J., 2003, Re-Os and U-Pb ages for the Butte copper district, Montana: A short- or long-lived hydrothermal system: *Geological Society of America (GSA) Abstracts with Programs*, v. 35, p. 400.
- Dirom, G.E., Dittrick, M.P., McArthur, D.R., Ogryzlo, P.L., Pardoe, A.J., Stothart, P.G., and Schroeter, T.G., 1995, Bell and Granisle porphyry copper-gold mines, Babine region, west-central British Columbia, in *Schroeter, T.G., ed., Porphyry deposits of the northwestern Cordillera of North America: Canadian Institute of Mining, Metallurgy and Petroleum, Special Volume 46*, p. 256–289.
- Duan, S., Zhang, Z., Jiang, Z., Zhao, J., Zhang, Y., Li, F., and Tian, J., 2014, Geology, geochemistry, and geochronology of the Dundee iron-zinc ore deposit in western Tianshan, China: *Ore Geology Reviews*, v. 57, p. 441–461.
- Dupuis, C., and Beaudoin, G., 2007, Signature géochimique des oxydes de fer et application à l'exploration minière – 2e volet: Annual report of project DIVEX SC-22, p. 1–24.
- 2011, Discriminant diagrams for iron oxide trace element fingerprinting of mineral deposit types: *Mineralium Deposita*, v. 46, p. 1–17.
- Egozcue, J.J., Pawlowsky-Glahn, V., Mateu-Figueras, G., and Barcelo-Vidal, C., 2003, Isometric logratio transformations for compositional data analysis: *Mathematical Geology*, v. 35, p. 279–300.
- Einaudi, M.T., 1982, Description of skarns associated with porphyry copper plutons, in *Titley, S.R., ed., Advances in geology of the porphyry copper deposits, southwestern North America: Tucson, Arizona, University of Arizona Press*, p. 139–183.
- Einaudi, M.T., Meinert, L.D., and Newberry, R.J., 1981, Skarn deposits: *Economic Geology 75th Anniversary Volume*, p. 317–391.
- Eliopoulos, D.G., Economou-Eliopoulos, M., and Zelyaskova-Panayiotova, M., 2014, Critical factors controlling Pd and Pt potential in porphyry Cu-Au deposits: Evidence from the Balkan Peninsula: *Geosciences*, v. 4, p. 31–49.
- Eriksson, L., Byrne, T., Johansson, E., Trygg, J., and Vikström, C., 2013, Multi- and megavariable data analysis: Basic principles and applications: Sweden, MKS Umetrics AB, p. 1–521.
- Fitton, J.G., 1987, Alkaline igneous rocks: *Geological Society of London, Special Publication 30*, 552 p.
- Floyd, P.A., and Winchester, J.A., 1978, Identification and discrimination of altered and metamorphosed volcanic rocks using immobile elements: *Chemical Geology*, v. 21, p. 291–306.
- Fraser, T.M., 1994, Geology, alteration and origin of hydrothermal breccias at the Mount Polley alkalic porphyry copper-gold deposit, south-central British Columbia: Unpublished master's thesis, Vancouver, British Columbia, The University of British Columbia, 275 p.
- Frei, R., 1995, Evolution of mineralizing fluid in the porphyry copper system of the Skouries deposit, Northeast Chalkidiki (Greece); evidence from combined Pb-Sr and stable isotope data: *Economic Geology*, v. 90, p. 746–762.
- Frost, B.R., and Lindsley, D.H., 1992, Equilibria among Fe-Ti oxides, pyroxenes, olivine, and quartz: Part II. Application: *American Mineralogist*, v. 77, p. 1004–1020.
- Ghiorso, M.S., and Sack, O., 1991, Fe-Ti oxide geothermometry: Thermodynamic formulation and the estimation of intensive variables in silicic magmas: *Contributions to Mineralogy and Petrology*, v. 108, p. 485–510.
- Gosselin, P., Beaudoin, G., and Jébrak, M., 2006, Signature géochimique des oxydes de fer et application à l'exploration minière: Annual report of projet DIVEX SC-16, p. 1–58.
- Harris, A.C., Dunlap, W.J., Reiners, P.W., Allen, C.M., Cooke, D.R., White, N.C., Campbell, I.H., and Golding, S.D., 2008, Multimillion year thermal history of a porphyry copper deposit: Application of U-Pb, ⁴⁰Ar/³⁹Ar and (U-Th)/He chronometers, Bajo de la Alumbrera copper-gold deposit, Argentina: *Mineralium Deposita*, v. 43, p. 295–314.
- Harris, C., and Sheppard, S.M.F., 1987, Magma and fluid evolution in the lavas and associated granite xenoliths of Ascension Island: *Geological Society of London, Special Publication 30*, p. 269–272.
- Heidarian, H., Lentz, D., Alirezaei, S., Peighambari, S., and Hall, D., 2016, Using the chemical analysis of magnetite to constrain various stages in the formation and genesis of the Kiruna-type chadormalu magnetite-apatite deposit, Bafq district, central Iran: *Mineralogy and Petrology*, v. 110, p. 927–942.
- Helsel, D.R., 2005, *Nondetects and data analysis. Statistics for censored environmental data*: New York, Wiley-Interscience, 268 p.
- Hemley, J.J., and Hunt, J.P., 1992, Hydrothermal ore-forming processes in the light of studies in rock-buffered systems; II. Some general geologic applications: *Economic Geology*, v. 87, p. 23–43.
- Henley, R.W., 1973, Solubility of gold in hydrothermal chloride solutions: *Chemical Geology*, v. 11, p. 73–87.
- Holbek, P., and Noyes, R., 2013, Copper mountain: An alkalic porphyry copper-gold-silver deposit in the southern Quesnel terrane, British Columbia: *Society of Economic Geologists Guidebook*, v. 44, p. 129–143.
- Hooper, P., 1994, Sources of continental flood basalts: The lithospheric component, in *Subbarao, K.V., ed., Volcanism: New Delhi, Wiley Eastern*, p. 29–53.
- Hou, T., Charlier, B., Holtz, F., Veksler, I., Zhang, Z., Thomas, R., and Namur, O., 2018, Immiscible hydrous Fe-Ca-P melt and the origin of iron oxide-apatite ore deposits: *Nature Communications*, v. 9, p. 1–8.
- Hron, K., Templ, M., and Filzmoser, P., 2010, Imputation of missing values for compositional data using classical and robust methods: *Computational Statistics and Data Analysis*, v. 54, p. 3095–3107.

- Hu, H., Li, J.-W., Lentz, D., Ren, Z., Zhao, X.-F., Deng, X.-D., and Hall, D., 2014, Dissolution-reprecipitation process of magnetite from the Chengchao iron deposit: Insights into ore genesis and implication for in-situ chemical analysis of magnetite: *Ore Geology Reviews*, v. 57, p. 393–405.
- Hu, H., Lentz, D., Li, J.-W., McCarron, T., Zhao, X.-F., and Hall, D., 2015, Re-equilibration processes in magnetite from iron skarn deposits: *Economic Geology*, v. 110, p. 1–8.
- Hu, X., Chen, H., Zhao, L., Han, J., and Xia, X., 2017, Magnetite geochemistry of the Longqiao and Tieshan Fe-(Cu) deposits in the Middle-Lower Yangtze River belt: Implications for deposit type and ore genesis: *Ore Geology Reviews*, v. 89, p. 822–835.
- Huang, X.-W., and Beaudoin, G., 2019, Textures and chemical composition of magnetite from iron oxide-copper-gold (IOCG) and Kiruna-type iron oxide-apatite (IOA) deposits and their implications for ore genesis and magnetite classification schemes: *Economic Geology*, v. 114, p. XXXX.
- Huang, X.-W., Zhou, M.-F., Qi, L., Gao, J.-F., and Wang, Y.-W., 2013, Re-Os isotopic ages of pyrite and chemical composition of magnetite from the Cihai magmatic-hydrothermal Fe deposit, NW China: *Mineralium Deposita*, v. 48, p. 925–946.
- Huang, X.-W., Qi, L., and Meng, Y.-M., 2014, Trace element geochemistry of magnetite from the Fe-(Cu) deposits in the Hami region, Eastern Tianshan orogenic belt, NW China: *Acta Geologica Sinica*, v. 88, p. 176–195.
- Huang, X.-W., Gao, J.-F., Qi, L., and Zhou, M.-F., 2015a, In-situ LA-ICP-MS trace elemental analyses of magnetite and Re-Os dating of pyrite: The Tianhu hydrothermally remobilized sedimentary Fe deposit, NW China: *Ore Geology Reviews*, v. 65, p. 900–916.
- Huang, X.-W., Zhou, M.-F., Qiu, Y.-Z., and Qi, L., 2015b, In-situ LA-ICP-MS trace elemental analyses of magnetite: The Bayan Obo Fe-REE-Nb deposit, North China: *Ore Geology Reviews*, v. 65, p. 884–899.
- Huang, X.-W., Gao, J.-F., Qi, L., Meng, Y.-M., Wang, Y.-C., and Dai, Z.-H., 2016, In-situ LA-ICP-MS trace elements analysis of magnetite: The Fenghuangshan Cu-Fe-Au deposit, Tongling, eastern China: *Ore Geology Reviews*, v. 72, p. 746–759.
- Huang, X.-W., Zhou, M.-F., Beaudoin, G., Gao, J.-F., Qi, L., and Lyu, C., 2018, Origin of the volcanic-hosted Yamansu Fe deposit, Eastern Tianshan, NW China: Constraints from pyrite Re-Os isotopes, stable isotopes, and in situ magnetite trace elements: *Mineralium Deposita*, v. 53, p. 1039–1060.
- Huang, X.-W., Boutroy, É., Makvandi, S., Beaudoin, G., Corriveau, L., and De Toni, A.F., 2019, Trace element composition of iron oxides from IOCG and IOA deposits: Relationship to hydrothermal alteration and deposit subtypes: *Mineralium Deposita*, v. 54, p. 525–552.
- Ilton, E.S., and Eugster, H.P., 1989, Base metal exchange between magnetite and a chloride-rich hydrothermal fluid: *Geochimica et Cosmochimica Acta*, v. 53, p. 291–301.
- Ishihara, S., 1977, The magnetite-series and ilmenite-series granitic rocks: *Mining Geology*, v. 27, p. 293–305.
- 1981, The granitoid series and mineralization: *Economic Geology 75th Anniversary Volume*, p. 458–484.
- Jago, C.P., Tosdal, R.M., Cooke, D.R., and Harris, A.C., 2014, Vertical and lateral variation of mineralogy and chemistry in the Early Jurassic Mt. Milligan alkalic porphyry Au-Cu deposit, British Columbia, Canada: *Economic Geology*, v. 109, p. 1005–1033.
- James, B.R., 2003, Chromium, in Stewart, B.A., and Howell, T. A., eds., *Encyclopedia of water science*: New York, Marcel Dekker, p. 77–82.
- Jurek, K., and Hulínský, V., 1980, The use and accuracy of the ZAF correction procedure for the microanalysis of glasses: *Microchimica Acta*, v. 73, p. 183–198.
- Kirkham, R.V., and Sinclair, W.D., 1995, Porphyry copper, gold, molybdenum, tungsten, tin, silver: *Canadian Institute of Mining and Metallurgy, Special Volume 39*, p. 50–71.
- Kirwin, D., Forster, C., Kavalieris, I., Crane, D., Orsich, C., Panther, C., Garamjav, D., Munkhbat, T., and Nüselkhuu, G., 2005, The Oyu Tolgoi copper-gold porphyry deposits, south Gobi, Mongolia: Society of Economic Geologists-International Association on the Genesis of Ore Deposits (SEG-IAGOD) Field Trip, August 14–16, 2005, p. 14–16.
- Knipping, J.L., Bilenker, L.D., Simon, A.C., Reich, M., Barra, F., Deditius, A.P., Wälle, M., Heinrich, C.A., Holtz, F., and Munizaga, R., 2015, Trace elements in magnetite from massive iron oxide-apatite deposits indicate a combined formation by igneous and magmatic-hydrothermal processes: *Geochimica et Cosmochimica Acta*, v. 171, p. 15–38.
- Kooiman, G.J.A., McLeod, M.J., and Sinclair, W.D., 1986, Porphyry tungsten-molybdenum orebodies, polymetallic veins and replacement bodies, and tin-bearing greisen zones in the Fire Tower zone, Mount Pleasant, New Brunswick: *Economic Geology*, v. 81, p. 1356–1373.
- Kouzmanov, K., von Quadt, A., Peytcheva, I., Harris, C., Heinrich, C.A., Rosu, E., and O'Connor, G., 2005, Rosia Poieni porphyry Cu-Au and Rosia Montana epithermal Au-Ag deposits, Apuseni Mts., Romania: Timing of magmatism and related mineralisation: *Bulgarian Academy of Sciences, Geochemistry, Mineralogy and Petrology*, v. 43, p. 113–117.
- Kroll, T., Müller, D., Seifert, T., Herzig, P.M., and Schneider, A., 2002, Petrology and geochemistry of the shoshonite-hosted Skouries porphyry Cu-Au deposit, Chalkidiki, Greece: *Mineralium Deposita*, v. 37, p. 137–144.
- Le Bas, M.J., Le Maitre, R.W., Streckeisen, A., and Zanettin, B., 1986, A chemical classification of volcanic rocks based on the total alkali-silica diagram: *Journal of Petrology*, v. 27, p. 745–750.
- Lee, L., and Helsel, D., 2007, Statistical analysis of water-quality data containing multiple detection limits II: S-language software for nonparametric distribution modeling and hypothesis testing: *Computers and Geosciences*, v. 33, p. 696–704.
- LeFort, D., Hanley, J., and Guillong, M., 2011, Subepithermal Au-Pd mineralization associated with an alkalic porphyry Cu-Au deposit, Mount Milligan, Quesnel terrane, British Columbia, Canada: *Economic Geology*, v. 106, p. 781–808.
- Li, G., 2012, Iron ore deposits in the Eastern Tianshan orogenic belt (China): The magnetite-skarn-magmatism association: Unpublished Ph.D. thesis, Orléans, France, University of Orléans, 356 p.
- Logan, J.M., and Mihalyuk, M.G., 2014, Tectonic controls on early Mesozoic paired alkaline porphyry deposit belts (Cu-Au ± Ag-Pt-Pd-Mo) within the Canadian Cordillera: *Economic Geology*, v. 109, p. 827–858.
- Lund, K., Aleinikoff, J.N., Kunk, M.J., Unruh, D.M., Zeihen, G.D., Hodges, W.C., du Bray, E.A., and O'Neill, J.M., 2002, SHRIMP U-Pb and ⁴⁰Ar/³⁹Ar age constraints for relating plutonism and mineralization in the Boulder batholith region, Montana: *Economic Geology*, v. 97, p. 241–267.
- Makvandi, S., Ghasemzadeh-Barvarz, M., Beaudoin, G., Grunsky, E.C., McClenaghan, M.B., and Duchesne, C., 2016a, Principal component analysis of magnetite composition from volcanogenic massive sulfide deposits: Case studies from the Izok Lake (Nunavut, Canada) and Halfmile Lake (New Brunswick, Canada) deposits: *Ore Geology Reviews*, v. 72, p. 60–85.
- Makvandi, S., Ghasemzadeh-Barvarz, M., Beaudoin, G., Grunsky, E.C., McClenaghan, M.B., Duchesne, C., and Boutroy, E., 2016b, Partial least squares-discriminant analysis of trace element compositions of magnetite from various VMS deposit subtypes: Application to mineral exploration: *Ore Geology Reviews*, v. 78, p. 388–408.
- Makvandi, S., Beaudoin, G., McClenaghan, M.B., and Quirr, D., 2017, Geochemistry of magnetite and hematite from unmineralized bedrock and local till at the Kiggavik uranium deposit: Implications for sediment provenance: *Journal of Geochemical Exploration*, v. 183, p. 1–21.
- McQueen, K.G., and Cross, A.J., 1998, Magnetite as a geochemical sampling medium: Application to skarn deposits, in Eggleton, R.A., ed., *The state of the regolith*: Brisbane, Geological Society of Australia, p. 194–199.
- Meinert, L.D., Dipple, G.M., and Nicolescu, S., 2005, World skarn deposits: *Economic Geology 100th Anniversary Volume*, p. 299–336.
- Meng, Y.-M., and Hu, R.-Z., 2018, Minireview: Advances in germanium isotope analysis by multiple collector-inductively coupled plasma-mass spectrometry: *Analytical Letters*, v. 51, p. 627–647.
- Meng, Y.M., Hu, R.Z., Huang, X.W., and Gao, J.F., 2017, Germanium in magnetite: A preliminary review: *Acta Geologica Sinica (English Edition)*, v. 91, p. 711–726.
- Middelburg, J.J., van der Weijden, C.H., and Woittiez, J.R.W., 1988, Chemical processes affecting the mobility of major, minor and trace elements during weathering of granitic rocks: *Chemical Geology*, v. 68, p. 253–273.
- Milu, V., Milesi, J.-P., and Leroy, J.L., 2004, Rosia Poieni copper deposit, Apuseni Mountains, Romania: Advanced argillic overprint of a porphyry system: *Mineralium Deposita*, v. 39, p. 173–188.
- Mountjoy, D., 2011, Granitoid-hosted magnetite as an indicator mineral for porphyry Cu ore deposits: Unpublished B.Sc. thesis, Victoria, British Columbia, University of Victoria, 41 p.
- Müller, A., Herrington, R., Armstrong, R., Seltnann, R., Kirwin, D.J., Stenina, N.G., and Kronz, A., 2010, Trace elements and cathodoluminescence of quartz in stockwork veins of Mongolian porphyry-style deposits: *Mineralium Deposita*, v. 45, p. 707–727.
- Müller, D., and Groves, D.I., 1993, Direct and indirect associations between potassic igneous rocks, shoshonites and gold-copper deposits: *Ore Geology Reviews*, v. 8, p. 383–406.

- 2000, Potassic igneous rocks and associated gold-copper mineralization, 3rd ed.: Berlin, Springer, 209 p.
- Mysen, B., 2012, High-pressure and high-temperature titanium solution mechanisms in silicate-saturated aqueous fluids and hydrous silicate melts: *American Mineralogist*, v. 97, p. 1241–1251.
- Nadoll, P., 2011, Geochemistry of magnetite from hydrothermal ore deposits and host rocks—case studies from the Proterozoic Belt Supergroup, Cu-Mo-porphry + skarn and Climax Mo deposits in the western United States: Unpublished Ph.D. thesis, Auckland, New Zealand, The University of Auckland, 311 p.
- Nadoll, P., Mauk, J.L., Hayes, T.S., Koenig, A.E., and Box, S.E., 2012, Geochemistry of magnetite from hydrothermal ore deposits and host rocks of the Mesoproterozoic Belt Supergroup, United States: *Economic Geology*, v. 107, p. 1275–1292.
- Nadoll, P., Angerer, T., Mauk, J.L., French, D., and Walshe, J., 2014, The chemistry of hydrothermal magnetite: A review: *Ore Geology Reviews*, v. 61, p. 1–32.
- Nadoll, P., Mauk, J.L., Leveille, R.A., and Koenig, A.E., 2015, Geochemistry of magnetite from porphyry Cu and skarn deposits in the southwestern United States: *Mineralium Deposita*, v. 50, p. 493–515.
- Nielsen, R.L., Forsythe, L.M., Gallahan, W.E., and Fisk, M.R., 1994, Major- and trace-element magnetite-melt equilibria: *Chemical Geology*, v. 117, p. 167–191.
- Pass, H.E., Cooke, D.R., Davidson, G., Maas, R., Dipple, G., Rees, C., Ferreira, L., Taylor, C., and Deyell, C.L., 2014, Isotope geochemistry of the Northeast zone, Mount Polley alkalic Cu-Au-Ag porphyry deposit, British Columbia: A case for carbonate assimilation: *Economic Geology*, v. 109, p. 859–890.
- Pearce, J.A., and Cann, J., 1973, Tectonic setting of basic volcanic rocks determined using trace element analyses: *Earth and Planetary Science Letters*, v. 19, p. 290–300.
- Perello, J., Cox, D., Garamjav, D., Sanjorj, S., Diakov, S., Schissel, D., Munkhbat, T.-O., and Oyun, G., 2001, Oyu Tolgoi, Mongolia: Siluro-Devonian porphyry Cu-Au-(Mo) and high-sulfidation Cu mineralization with a Cretaceous chalcocite blanket: *Economic Geology*, v. 96, p. 1407–1428.
- Perelló, J., Raziq, A., Schloderer, J., and Asad-ur-Rehman, 2008, The Chagai porphyry copper belt, Baluchistan Province, Pakistan: *Economic Geology*, v. 103, p. 1583–1612.
- Pisiak, L.K., Canil, D., Lacourse, T., Plouffe, A., and Ferbey, T., 2017, Magnetite as an indicator mineral in the exploration of porphyry deposits: A case study in till near the Mount Polley Cu-Au deposit, British Columbia, Canada: *Economic Geology*, v. 112, p. 919–940.
- Pollard, P.J., 2006, An intrusion-related origin for Cu-Au mineralization in iron oxide-copper-gold (IOCG) provinces: *Mineralium Deposita*, v. 41, p. 179–187.
- Porter, T.M., 2016, The geology, structure and mineralisation of the Oyu Tolgoi porphyry copper-gold-molybdenum deposits, Mongolia: A review: *Geoscience Frontiers*, v. 7, p. 375–407.
- Proffett, J.M., 2003, Geology of the Bajo de la Alumbrera porphyry copper-gold deposit, Argentina: *Economic Geology*, v. 98, p. 1535–1574.
- Raziq, A., Tosdal, R.M., and Creaser, R.A., 2014, Temporal evolution of the western porphyry Cu-Au systems at Reko Diq, Baluchistan, western Pakistan: *Economic Geology*, v. 109, p. 2003–2021.
- Redmond, P.B., and Einaudi, M.T., 2010, The Bingham Canyon porphyry Cu-Mo-Au deposit. I. Sequence of intrusions, vein formation, and sulfide deposition: *Economic Geology*, v. 105, p. 43–68.
- Reed, M., Rusk, B., and Palandri, J., 2013, The Butte magmatic-hydrothermal system: One fluid yields all alteration and veins: *Economic Geology*, v. 108, p. 1379–1396.
- Richards, J.P., 2014, Discussion of Sun et al. (2013): The link between reduced porphyry copper deposits and oxidized magmas: *Geochimica et Cosmochimica Acta*, v. 126, p. 643–645.
- Richards, J.P., and Mumin, A.H., 2013, Magmatic-hydrothermal processes within an evolving Earth: Iron oxide-copper-gold and porphyry Cu \pm Mo \pm Au deposits: *Geology*, v. 41, p. 767–770.
- Richards, J.P., Bray, C.J., Chamer, D.M.D., and Spooner, E.T.C., 1997, Fluid chemistry and processes at the Porgera gold deposit, Papua New Guinea: *Mineralium Deposita*, v. 32, p. 119–132.
- Richards, J.P., Wilkinson, D., and Ullrich, T., 2006, Geology of the Sari Gunay epithermal gold deposit, northwest Iran: *Economic Geology*, v. 101, p. 1455–1496.
- Richards, J.P., López, G.P., Zhu, J.-J., Creaser, R.A., Locock, A.J., and Mumin, A.H., 2017, Contrasting tectonic settings and sulfur contents of magmas associated with Cretaceous porphyry Cu \pm Mo \pm Au and intrusion-related iron oxide Cu-Au deposits in northern Chile: *Economic Geology*, v. 112, p. 295–318.
- Roberts, M.P., and Clemens, J.D., 1993, Origin of high-potassium, calc-alkaline, I-type granitoids: *Geology*, v. 21, p. 825–828.
- Romero, B., Kojima, S., Wong, C., Barra, F., Véliz, W., and Ruiz, J., 2011, Molybdenite mineralization and Re-Os geochronology of the Escondida and Escondida Norte porphyry deposits, northern Chile: *Resource Geology*, v. 61, p. 91–100.
- Ronacher, E., Richards, J., Reed, M., Bray, C., Spooner, E., and Adams, P., 2004, Characteristics and evolution of the hydrothermal fluid in the North zone high-grade area, Porgera gold deposit, Papua New Guinea: *Economic Geology*, v. 99, p. 843–867.
- Rudnick, R.L., and Gao, S., 2003, Composition of the continental crust, in Holland, H.D., and Turekian, K.K., eds., *Treatise on geochemistry*, v. 3. The crust: Oxford, Elsevier-Pergamon, p. 1–64.
- Rusk, B.G., Reed, M.H., and Dilles, J.H., 2008, Fluid inclusion evidence for magmatic-hydrothermal fluid evolution in the porphyry copper-molybdenum deposit at Butte, Montana: *Economic Geology*, v. 103, p. 307–334.
- Rusk, B.G., Oliver, N.H.S., Zhang, D., Brown, A., Lilly, R., and Jungmann, D., 2009, Compositions of magnetite and sulfides from barren and mineralized IOCG deposits in the eastern succession of the Mt. Isa inlier, Australia: Geological Society of America (GSA) Annual Meeting, Portland, Oregon, October 18–21, 2009, Proceedings, p. 84.
- Salvi, S., and Williams-Jones, A.E., 2006, Alteration, HFSE mineralisation and hydrocarbon formation in peralkaline igneous systems: Insights from the Strange Lake pluton, Canada: *Lithos*, v. 91, p. 19–34.
- Samson, I.M., 1990, Fluid evolution and mineralization in a subvolcanic granite stock; the Mount Pleasant W-Mo-Sn deposits, New Brunswick, Canada: *Economic Geology*, v. 85, p. 145–163.
- Savard, D., Barnes, S.J., Dare, S., and Beaudoin, G., 2012, Improved calibration technique for magnetite analysis by LA-ICP-MS: *Mineralogical Magazine*, v. 76, p. 2329.
- Schwartz, M., and Melcher, F., 2004, The Falémé iron district, Senegal: *Economic Geology*, v. 99, p. 917–939.
- Seedorff, E., Dilles, J.H., Proffett, J.M., Jr., Einaudi, M.T., Zurcher, L., Stavast, W.J.A., Johnson, D.A., and Barton, M.D., 2005, Porphyry deposits: Characteristics and origin of hypogene features: *Economic Geology* 100th Anniversary Volume, p. 251–298.
- Selby, D., and Creaser, R.A., 2001, Re-Os geochronology and systematics in molybdenite from the Endako porphyry molybdenum deposit, British Columbia, Canada: *Economic Geology*, v. 96, p. 197–204.
- Selby, D., Nesbitt, B.E., Muehlenbachs, K., and Prochaska, W., 2000, Hydrothermal alteration and fluid chemistry of the Endako porphyry molybdenum deposit, British Columbia: *Economic Geology*, v. 95, p. 183–202.
- Shchekina, T.I., and Gramenitskii, E.N., 2008, Geochemistry of Sc in the magmatic process: Experimental evidence: *Geochemistry International*, v. 46, p. 351–366.
- Shimazaki, H., 1998, On the occurrence of silician magnetites: *Resource Geology*, v. 48, p. 23–29.
- Siewwright, R.H., Wilkinson, J.J., O'Neill, H.S.C., and Berry, A.J., 2017, Thermodynamic controls on element partitioning between titanomagnetite and andesitic-dacitic silicate melts: Contributions to Mineralogy and Petrology, v. 172, p. 1–33.
- Sillitoe, R.H., 1979, Some thoughts on gold-rich porphyry copper deposits: *Mineralium Deposita*, v. 14, p. 161–174.
- 1997, Characteristics and controls of the largest porphyry copper-gold and epithermal gold deposits in the circum-Pacific region: *Australian Journal of Earth Sciences*, v. 44, p. 373–388.
- 2000, Gold-rich porphyry deposits: Descriptive and genetic models and their role in exploration and discovery: *Reviews in Economic Geology*, v. 13, p. 315–345.
- 2003, Iron oxide copper-gold deposits: An Andean view: *Mineralium Deposita*, v. 38, p. 787–812.
- 2010, Porphyry copper systems: *Economic Geology*, v. 105, p. 3–41.
- Simon, A.C., Pettke, T., Candela, P.A., Piccoli, P.M., and Heinrich, C.A., 2004, Magnetite solubility and iron transport in magmatic-hydrothermal environments: *Geochimica et Cosmochimica Acta*, v. 68, p. 4905–4914.
- Simon, A.C., Knipping, J., Reich, M., Barra, F., Deditius, A.P., Bilenker, L., and Childress, T., 2018, Kiruna-type iron oxide-apatite (IOA) and iron oxide copper-gold (IOCG) deposits form by a combination of igneous and magmatic-hydrothermal processes: Evidence from the Chilean iron belt: *Society of Economic Geologists, Special Publication 21*, p. 89–114.

- Sinclair, W.D., 1995, Porphyry W: British Columbia Ministry of Energy, Mines and Petroleum Resources, Open File 1995–20, p. 101–104.
- 2007, Porphyry deposits: Geological Association of Canada, Mineral Deposits Division, Special Publication 5, p. 223–243.
- Singer, D.A., 1995, World class base and precious metal deposits; a quantitative analysis: *Economic Geology*, v. 90, p. 88–104.
- Singoyi, B., Danyushevsky, L., Davidson, G.J., Large, R., and Zaw, K., 2006, Determination of trace elements in magnetites from hydrothermal deposits using the LA ICP-MS technique: SEG 2006: Wealth Creation in the Minerals Industry, Society of Economic Geologists, Keystone, Colorado, May 14–16, 2006, Proceedings, CD-ROM.
- Sossi, P.A., Prytulak, J., and O'Neill, H.S.C., 2018, Experimental calibration of vanadium partitioning and stable isotope fractionation between hydrous granitic melt and magnetite at 800°C and 0.5 GPa: *Contributions to Mineralogy and Petrology*, v. 173, p. 27.
- Sun, W., Arculus, R.J., Kamenetsky, V.S., and Binns, R.A., 2004, Release of gold-bearing fluids in convergent margin magmas prompted by magnetite crystallization: *Nature*, v. 431, p. 975–978.
- Sun, W.D., Liang, H.Y., Ling, M.X., Zhan, M.Z., Ding, X., Zhang, H., Yang, X.Y., Li, Y.L., Ireland, T.R., and Wei, Q.R., 2013, The link between reduced porphyry copper deposits and oxidized magmas: *Geochimica et Cosmochimica Acta*, v. 103, p. 263–275.
- Tanis, E.A., Simon, A., Tschauner, O., Chow, P., Xiao, Y., Burnley, P., Cline, C.J., Hanchar, J.M., Pettke, T., and Shen, G., 2015, The mobility of Nb in rutile-saturated NaCl- and NaF-bearing aqueous fluids from 1–6.5 GPa and 300–800°C: *American Mineralogist*, v. 100, p. 1600–1609.
- Tanis, E.A., Simon, A., Zhang, Y., Chow, P., Xiao, Y., Hanchar, J.M., Tschauner, O., and Shen, G., 2016, Rutile solubility in NaF–NaCl–KCl-bearing aqueous fluids at 0.5–2.79 GPa and 250–650°C: *Geochimica et Cosmochimica Acta*, v. 177, p. 170–181.
- Titley, S.R., 1990, Evolution and style of fracture permeability in intrusion-centered hydrothermal systems, in Titley, S.R., ed., *The role of fluids in crustal processes*: Washington D.C., National Academic Press, p. 50–63.
- Toplis, M., and Carroll, M., 1995, An experimental study of the influence of oxygen fugacity on Fe–Ti oxide stability, phase relations, and mineral–melt equilibria in ferro-basaltic systems: *Journal of Petrology*, v. 36, p. 1137–1170.
- Toplis, M.J., and Corgne, A., 2002, An experimental study of element partitioning between magnetite, clinopyroxene and iron-bearing silicate liquids with particular emphasis on vanadium: *Contributions to Mineralogy and Petrology*, v. 144, p. 22–37.
- Tornos, F., Velasco, F., Barra, F., and Morata, D., 2010, The Tropezón Cu–Mo–(Au) deposit, northern Chile: The missing link between IOCG and porphyry copper systems?: *Mineralium Deposita*, v. 45, p. 313–321.
- Ulrich, T., and Heinrich, C.A., 2001, Geology and alteration geochemistry of the porphyry Cu–Au deposit at Bajo de la Alumbrera, Argentina: *Economic Geology*, v. 96, p. 1719–1742.
- Watenphul, A., Schmidt, C., and Scholten, L., 2012, First insights into Cr³⁺ solubility in aqueous fluids at elevated P and T by m-XRF: 1st European Mineralogical Conference (EMC): Frankfurt, Germany, 2012, Abstract 544.
- Watenphul, A., Scholten, L., Kavner, A., Alraun, P., Falkenberg, G., Newville, M., Lanzirrotti, A., and Schmidt, C., 2013, Cu and Ni solubility in high-temperature aqueous fluids: American Geophysical Union (AGU), Fall Meeting, San Francisco, California, 2013, Abstract MR33A-2311.
- Webster, J.D., and Holloway, J.R., 1990, Partitioning of F and Cl between magmatic-hydrothermal fluids and highly evolved granitic magmas: *Geological Society of America, Special Paper 246*, p. 21–34.
- Wen, G., Li, J.-W., Hofstra, A.H., Koenig, A.E., Lowers, H.A., and Adams, D., 2017, Hydrothermal reequilibration of igneous magnetite in altered granitic plutons and its implications for magnetite classification schemes: Insights from the Handan–Xingtai iron district, North China craton: *Geochimica et Cosmochimica Acta*, v. 213, p. 255–270.
- Westendorp, R.W., Watkinson, D.H., and Jonasson, I.R., 1991, Silicon-bearing zoned magnetite crystals and the evolution of hydrothermal fluids at the Ansil Cu–Zn mine, Rouyn-Noranda, Quebec: *Economic Geology*, v. 86, p. 1110–1114.
- Whitten, E.H.T., 1995, Open and closed compositional data in petrology: *Mathematical Geology*, v. 27, p. 789–806.
- Williams, P.J., Barton, M.D., Johnson, D.A., Fontbote, L., De Haller, A., Mark, G., Oliver, N.H.S., and Marschik, R., 2005, Iron oxide copper-gold deposits: Geology, space-time distribution and possible modes of origin: *Economic Geology 100th Anniversary Volume*, p. 371–405.
- Williams-Jones, A.E., and Heinrich, C.A., 2005, 100th Anniversary special paper: Vapor transport of metals and the formation of magmatic-hydrothermal ore deposits: *Economic Geology*, v. 100, p. 1287–1312.
- Wilson, A.J., Cooke, D.R., Stein, H.J., Fanning, C.M., Holliday, J.R., and Tedder, I.J., 2007, U–Pb and Re–Os geochronologic evidence for two alkaline porphyry ore-forming events in the Cadia district, New South Wales, Australia: *Economic Geology*, v. 102, p. 3–26.
- Wilson, J.W.J., Kesler, S.E., Cloke, P.L., and Kelly, W.C., 1980, Fluid inclusion geochemistry of the Granisle and Bell porphyry copper deposits, British Columbia: *Economic Geology*, v. 75, p. 45–61.
- Wilson, M., 1996, *Igneous petrogenesis*: London, Chapman and Hall, 466 p.
- Wold, S., Sjöström, M., and Eriksson, L., 2001, PLS-regression: A basic tool of chemometrics: *Chemometrics and Intelligent Laboratory Systems*, v. 58, p. 109–130.
- Xie, Q., Zhang, Z., Hou, T., Jin, Z., and Santosh, M., 2017, Geochemistry and oxygen isotope composition of magnetite from the Zhangmatun deposit, North China craton: Implications for the magmatic-hydrothermal evolution of Cornwall-type iron mineralization: *Ore Geology Reviews*, v. 88, p. 57–70.
- Yang, W.-B., Niu, H.-C., Shan, Q., Sun, W.-D., Zhang, H., Li, N.-B., Jiang, Y.-H., and Yu, X.-Y., 2014, Geochemistry of magmatic and hydrothermal zircon from the highly evolved Baerzhe alkaline granite: Implications for Zr–REE–Nb mineralization: *Mineralium Deposita*, v. 49, p. 451–470.
- Yang, X.-M., Lentz, D.R., and McCutcheon, S.R., 2003, Petrochemical evolution of subvolcanic granitoid intrusions within the Late Devonian Mount Pleasant caldera, southwestern New Brunswick, Canada: Comparison of Au versus Sn–W–Mo–polymetallic mineralization systems: *Atlantic Geology*, v. 39, p. 97–121.
- Yi, L., Gu, X., Lu, A., Liu, J., Lei, H., Wang, Z., Cui, Y., Zuo, H., and Shen, C., 2015, Major and trace elements of magnetite from the Qimantag metallogenic belt: Insights into evolution of ore-forming fluids: *Acta Geologica Sinica (English Edition)*, v. 89, p. 1226–1243.
- Zhao, L., Chen, H., Zhang, L., Li, D., Zhang, W., Wang, C., Yang, J., and Yan, X., 2018, Magnetite geochemistry of the Heijianshan Fe–Cu (–Au) deposit in Eastern Tianshan: Metallogenic implications for submarine volcanic-hosted Fe–Cu deposits in NW China: *Ore Geology Reviews*, v. 100, p. 422–440.
- Zhao, W.W., and Zhou, M.-F., 2015, In-situ LA-ICP-MS trace elemental analyses of magnetite: The Mesozoic Tengtie skarn Fe deposit in the Nanling Range, South China: *Ore Geology Reviews*, v. 65, p. 872–883.



Xiao-Wen Huang is an assistant professor in the Institute of Geochemistry, Chinese Academy of Sciences (IGCAS). He received his B.Sc. degree in resource exploration engineering from the Kunming University of Science and Technology in 2008 and his Ph.D. degree in geochemistry from the University of Chinese Academy of Sciences in 2013. He has conducted postdoctoral research at the Laval University (Québec, Canada) from August 2016 to August 2019. His research interests include Re–Os isotope and platinum group element analytical methods and applications, indicator minerals in mineral exploration, and genesis of iron oxide-related deposits (e.g., IOCG, IOA, skarn).